Printed sensors for indoor air quality

A thesis presented in partial fulfilment of the

requirements for the degree of

Doctor of Philosophy

in

Engineering

Massey University, Albany,

New Zealand

Muhammad Asif Ali Rehmani

November 2021

I would like to dedicate this thesis to my late father, mother, wife, wonderful kids and siblings...

Declaration of Authorship

This thesis has been furnished according to the Massey University "PhD Thesis by publication" guildelines. The thesis is based on the technical manuscripts either published or currently under review or in preparation for submission to the reputable academic journals.

Muhammad Asif Ali Rehmani

Acknowledgements

First and foremost I want to thank Almighty, Allah for guiding me throughout my PhD tenure without His blessings it was not possible to reach here. I would like to express my sincere gratitude to my main supervisor Dr. Khalid Mahmood Arif. I would not have achieved this without his support. I would like to acknowledge the continuous support of my co-supervisor(s) Dr. Catherine Whitby, and Dr. Mathew Stevens. Their guidance has helped me at all times of my research and writing of this thesis. I could not have imagined having better advisors and mentors for my PhD study. I would like to extend my thanks to Massey University for supporting my studies with a Doctoral Scholarship and to the Department of Mechanical and Electrical Engineering for providing additional support.

My sincere thanks to the technical and administrative staff at Massey University who gave access to the laboratory and research facilities. Without their support, it would not be possible to conduct this research.

I thank my fellow lab mates for the stimulating discussions while we were working together before deadlines, and for all the fun we have had in the last three years. Also, I thank my friends at Massey University. In particular, I am grateful to Muhammad Harris, Swapna Jaywant, and Ayesha Shaukat for invaluable support during my PhD studies.

Last but not the least, I would like to thank my family who stood firmly throughout my PhD tenure. Especially my mother, wife, wonderful kids and siblings for their support, encouragement and unconditional love throughout this journey and my life in general.

Abstract

On average, a human inhale about 14,000 litres of air every day. The quality of inhaled air is highly important as the presence of pathogens and contaminants in air can adversely affect human health. Generally, the probability of pathogens/contaminant is high in indoor environment where humans spend an estimated 90% of their total lifetime. Continuous urbanization, increasing population, technological advancement and automation has further increased the time spent indoors. The length of exposure and indoor activities such as cooking, smoking, ventilation and frequency of cleaning can further aggravate the health risk due to localized higher concentrations of the contaminants. According to the Environmental Protection Agency (EPA), poor indoor air quality (IAQ) is considered one of the top environmental dangers to the public as increasing number of people are suffering from asthma, allergies, heart disease, and even lung cancer. In New Zealand, poor air quality is estimated to cause 730 premature deaths and cost over one billion dollars in restricted activity days per year.

The above premise cannot be validated until and unless there are means and measures of continually monitoring the indoor air pollutants with emphasis that the same can be fabricated using low cost and energy efficient methods. Furthermore, any remedial actions cannot be undertaken if the quantitative values of the environmental pollutants are unknown. Existing solutions for the air quality monitoring are expensive and can only be applied in certain numbers, leaving areas of the houses, offices, and schools unmonitored. Therefore, a ubiquitous system of air quality monitoring is needed, the one that can be applied on large areas like walls, roofs and so on. Such a prevalent system will allow sensing of air quality parameters rapidly, continuously, and with low power consumption.

To realize the bigger objective of achieving sensing and aware surfaces for indoor air quality, this research proposes to print sensors on large surfaces rather than making them in batches and packaging in discrete units. Recent advancements in inkjet printing provide solutions which can enable the implementation of such sensors. However, the choice of inkjet printing method has major impact on the efficacy of printed sensors. Therefore, we have explored printing techniques based on conventional screen printing and non-conventional electrohydrodynamic (EHD) inkjet printing. These printing methods offer low-cost, rapid prototyping and high-thorough-put conductive printing of features as compared to other inkjet printing methods with the latter bringing further advantages of improved resolution, scalability, customization and little or no environmental waste printing solution.

For screen printing, laser ablation process has been used to implement several customized transduction schemes. The utility of this technique is demonstrated by humidity sensing. It has been found that the designs of the transduction electrodes can easily be customized, and large area printing can be realized on the substrate. The fabricated humidity sensor provides higher sensitivity through bio-compatible sensing layer with good response and recovery time.

Next, EHD printing was explored for high-resolution conductive printing on flexible substrates. Current EHD printing focuses on improving the print resolution by decreasing the printhead nozzle diameter thus limiting the type of ink to be used for printing purpose. In the proposed EHD printhead design we overcame this major shortcoming by improving the resolution of printed feature with a bigger nozzle of 0.5 mm diameter. This resulted in the printed feature resolution of less than 10 μm in general with the highest achieved resolution 1.85 μm. The effective nozzle diameter to printed feature ratio of more than 250 was achieved. The use of bigger nozzle for fine resolution printing opens the avenue for utilizing higher concentration of metallic nano-particles inks through EHD printing. The hallmark of the presented EHD printhead design is the utilization of off-the-shelf components which does not require expensive manufacturing process while highlighting the importance of wetting area profile of the nozzle to facilitate fine resolution printing which until now has not been explored in detail. Furthermore, the work highlights the issue of crack development during EHD printing in the conductive tracks while using available piezoelectric inkjet ink. Later the ink was modified to minimise the cracks in EHD printed features.

Finally, a comprehensive study on the 3D printed microfluidic channels was conducted. The study highlights the variation of pressure developed in different microfluidic channel designs and the susceptibility of leakages from microfluidic devices. The work presents the possibility of utilizing the 3D printed microfluidics with printed sensors for deploying as lab-on-a-chip in various applications, such as passing a stream of air through sensors integrated in a microfluidic device for analysing the volatile organic compounds, humidity, toxic gases, and other analytes of interest.

Overall, the presented work demonstrates the feasibility of using conventional and non-conventional printing methods through simple implementations for the fabrication of IAQ sensors with high degree of customization, low processing cost and scalability.

Contents

List of Figures

List of Tables

Abbreviations

3DP	3-Dimensional Printing
AC	Alternating Current
AgF-DGME	Silver Flake - Diethylene glycol monoethyl ether
AgNF	Silver Nanoflakes
AgNP	Silver Nanoparticles
AM	Additive Manufacturing
CAD	Computer Aided Design
CO2	Carbon Dioxide
COE	Coefficient of Expansion
COT	Commercial off-the-shelf
DEG	Diethylene Glycol
DGME	Diethylene glycol monoethyl ether
EG	Ethylene Glycol
EHD	Electrohydrodynamic
EPA	Environmental Protection Agency
FDM	Fused Deposition Modelling
FSS	Full-scale Span
IAQ	Indoor Air Quality
IDEs	Interdigital Electrodes
IPA	Isopropyl Alcohol
IPL	Intense Pulsed Light
LOC	Length of Detecion
MEMs	Microelectromechanical Systems
OEM	Original Equipment Manufacturer
OHP	Overhead Projector

PCB	Printed Circuit Board
PDMS	Polydimethylsiloxane
PEDOT:PSS	Polyethylene Dioxythiopene Polystyrene
PET	Polyethylene Naphthalate
PIJ	Piezoelectric Inkjet
PLA	Poly(Lactic Acid) Acrylate
PMMA	Poly (methyl methacrylate)
PP	Parallel Plate
PVP	Polyvinyl Propylene
RH	Relative Humidity
SEM	Scanning Electron Microscopy
SLA	Stereolithography
SLS	Selective Laser Sintering
TEB	Total Error Band
TIJ	Thermal Inkjet
UV	Ultraviolet
WHO	World Health Organization

Chapter 1

Introduction

1.1 Overview

Urban populating usually spend most of their time indoors. Occupant health can be adversely affected by prolonged exposure due to poor indoor air quality. It is difficult to assess the potential threat posed by indoor air quality without a consistent and continuous monitoring regime due to the longevity of its continuous exposure, potentially making it a silent killer [1, 2]. Indoor air is estimated to be more polluted than outdoors by several orders of magnitude [3, 4]. More often, human response to indoor air pollution is absent owing to the lack of immediate sensing and threat quantification, and this leads to acute or serious health hazards.

Sensing technology is ever-changing; new systems and devices continue to enter our daily lives with the intent to improve our well-being. However, in order to reap the benefits from sensing technology, there is a greater need to collect data over time continuously, especially in the case of indoor air quality monitoring. Additionally, efforts should be made to seamlessly integrate these devices with our existing buildings and infrastructure so that corrective actions and predictions can be made from the collected data.

Unfortunately, little effort has so far been made to integrate the air quality monitoring devices in the existing buildings and infrastructure. Consequently, any remedial actions cannot be undertaken as the accurate quantitative values of the environmental pollutants are unknown. In the words of Lord Kelvin (1824-1907): “If you cannot measure it, you

cannot improve it". An improvement can be as simple as opening a window, but you would only do this if you are cognisant of the air quality of your surroundings.

1.2 Motivation

Air quality control or any remedial actions to improve indoor air rely on the ability of sensors to measure the air quality parameters. Therefore, sensitive, specific, low-cost, non-intrusive and readily integrable sensors are highly desired. Unfortunately, such sensors do not exist and most of the sensors used in IAQ monitoring applications are discrete units that can cover only parts of indoor environments. The major reason for this is probably the way the sensors are normally manufactured/fabricated.

Several different technologies exist for the fabrication of sensors, the most common being the microelectromechanical systems (MEMs) technology. MEMs is a proven technology but there are many drawbacks like the requirement of a clean room and special substrates e.g. silicon wafers. Due to the limitations of the MEMs technology numerous alternate techniques (such as piezoelectric [5, 6] and thermal inkjet printing [7], electrohydrodynamic printing [8], etc.) have been developed in the past couple of decades. The main focus of the alternate technologies is to enable sensor production in ambient environments leading to cost-effective sensors. However, more research and development is needed to improve the print resolution, range of materials and substrates, transduction mechanisms and sensing schemes. Despite the current limitations of the printing technologies, they have a huge potential in the area of sensor fabrication that is evident from their success in paper printing industry.

Considering the need for IAQ sensors and potential of printing technologies, this thesis is dedicated to the investigation, improvement, adoption and application of both conventional (screen printing) and non-conventional (electrohydrodynamic (EHD)) technologies. The selected printing technologies are considered as the most viable contactless printing technologies in term of cost, printing resolution, scalability and process customization. The results obtained from these techniques are expected to not only allow further development in the low-cost printed sensors for air quality but can also be extended to other applications.

1.3 Contributions

The main contributions of this thesis can be summarized as below:

- The current contactless printing technologies heavily rely on the size of the nozzle to improve the printing resolution. However, by reducing the nozzle size it puts limitation on the use of ink or material that can deposited. In our proposed high-resolution EHD printing, the convention of reducing the nozzle diameter to achieve a smaller droplet size has been addressed. This enables the printing of material having a wide range of viscosities, surface tension and composition. Furthermore, bigger nozzle diameter for high-resolution printing facilitate the use of polymer-based inks, proteins and multi-material deposition for applications not only in the domain of air quality sensing but also in the areas of biomedical, optics, soft robotics and related sensor applications.

- The development of suitable ink for a specific printing method is often complex and costly. Therefore, readily available commercial-off-the-shelf (COTs) inks seem to be a cost-effective solution for printing applications. In our work COTs piezoelectric ink utilized for EHD printing developed cracks. As a result, we demonstrated that the ink could be tuned easily for crack-free printing through the cost-effective processing of ink. The results identify the probable reasons for the crack formation and its remedial solution which can be of great assets for researchers working in the similar domains.

- To improve the sensitivity of sensors, the sensing layer is often chosen to give high sensitivity. However, there is little or no focus on improving the sensitivity by considering transduction electrode geometries. In our work, we have demonstrated that the same sensing layer can have different sensing responses towards the analyte of interest. This opens the avenue for researchers where further improvement on the sensing capabilities of the sensors can be realized by incorporating suitable transduction geometries.

- Last but not least, an exhaustive study on the characterisation of fused deposition based microchannels for microfluidic applications has provided the pressure ranges at which the microfluidic devices work without leaking. The results obtained from the study provide the quantitative differential pressure values for integrating

microfluidics with the printed sensors for realising packaged standalone lab-on-a-chip systems for medley of applications.

1.4 An Overview of Printing Technologies

Since the main topic of the thesis is focused on printing technologies, particularly inkjet printing, a brief overview of the existing printing technologies along with their pros and cons is provided in this sections.

Generally, printing technologies can be divided into contact and contactless printing [9, 10] as shown in Figure 1.1. In contact printing the imprint on the substrate is generated when a web is fed through the pressing rollers which generates the conductive tracks on the substrate. Offset, flexography and gravure are the prominent contact printing methods. Whereas, in case of contactless printing the ink is forced out of the nozzle either through a push force generated inside the ink chamber or pull force at the tip of the nozzle. Aerosol, thermal, piezoelectric, electrohydrodynamic and acoustic inkjet printing are the prominent contactless inkjet printing methods. Contact printing has been widely used in print media over the years due to their high thorough-put with accuracies up to 50 μm, with gravure printing reaching higher resolution and high aspect ratios [11]. However, when the substrate passes through the series of imprinting rollers the registration control in case of tight tolerances is challenging. In most cases the substrate velocity is high and flexible substrate is susceptible to stretch under high pressure. The stretchability of the substrate, speed of the web and pressure on the substrate makes the registration even difficult and requires design of complex registration algorithms [12–15]. Contact printing has an inherent advantage of producing cheaper item on per unit basis for large productive batches [16–19] when compared with contactless printing. However, feature customization or changes in contact printing during the process is not possible as it requires changes in pattern on the imprinting rollers which is often expensive and complex. Moreover, the overall printing process produces ink wastage at various stages of printing. On the other hand, for small production batches contactless printing is cheaper and offers additional benefits of no ink wastage and on-the-fly feature customizations [20, 21].

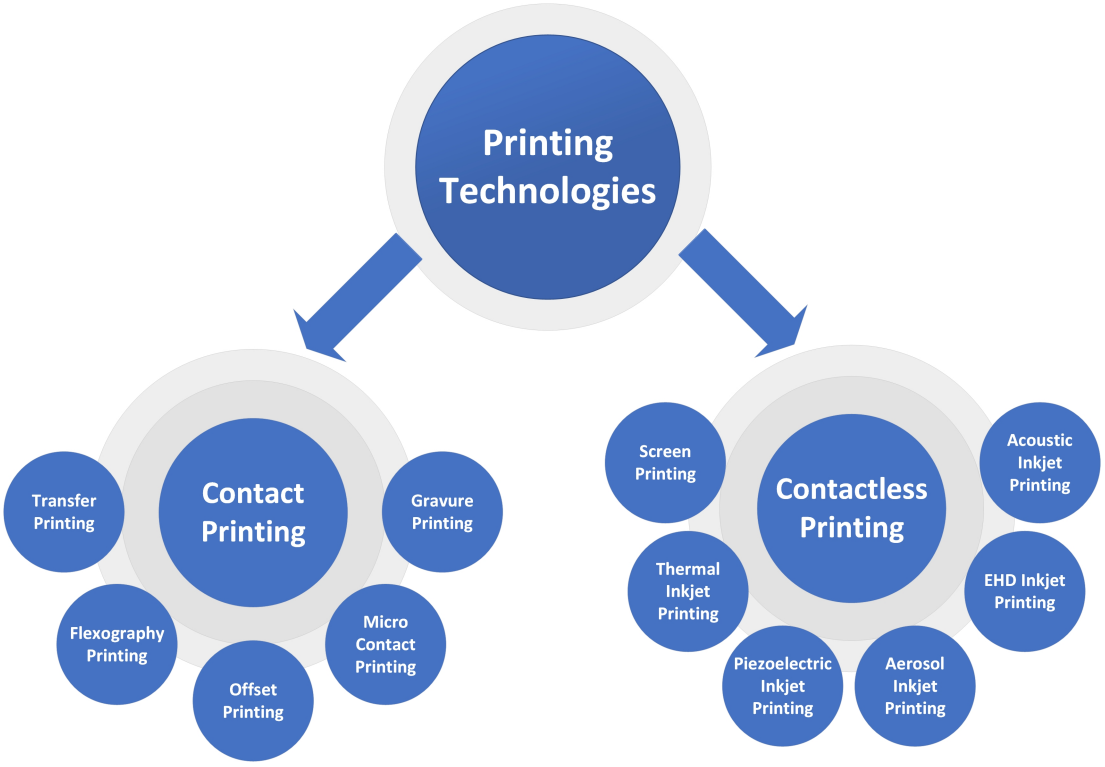

FIGURE 1.1: Common printing technologies

Due to their inherent benefit of low cost, low environmental footprint and customizability, contactless printing is more suited for small batch production, prototyping and lab scale manufacturing. Following are the key contactless printing methods

1. Piezoelectric Inkjet Printing
2. Thermal Inkjet Printing
3. Aerosol Inkjet Printing
4. Acoustophoretic Inkjet Printing
5. Electrohydrodynamic Inkjet Printing

1.4.1 Piezoelectric Inkjet Printing

The droplet ejection phenomenon of piezoelectric inkjet printing process is based on the ink displaced in the ink chamber by the deformation of thin piezo-ceramic membrane often referred as piezoelectric membrane. When the voltage is applied to this piezoelectric material it undergoes physical deformation by changing its shape and size as depicted

in Figure 1.2. The deformation of piezoelectric membrane causes the pressure gradient inside the ink chamber and ejects the droplet from the nozzle. Once the applied voltage is removed the membrane goes back to its original shape. Successive series of pulsed voltage results in the controllable drop-on-demand ink deposition from the piezoelectric actuated printhead on the substrate.

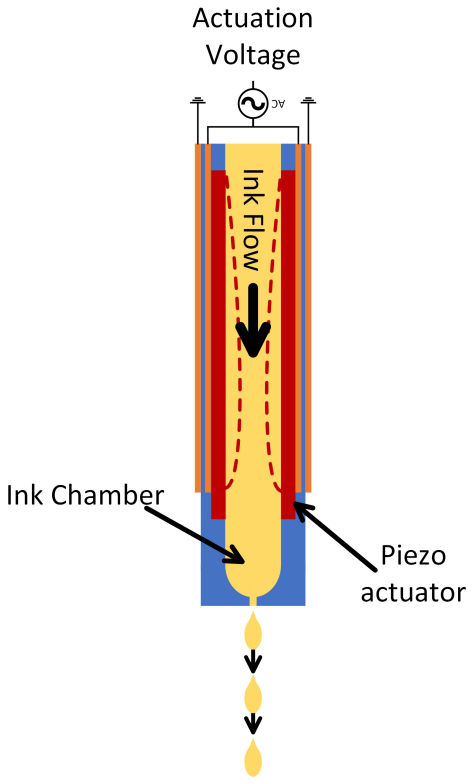

FIGURE 1.2: Squeeze mode piezoelectric printhead: Principle of operation

1.4.2 Thermal Inkjet Printing

A thermal inkjet consists of an ink chamber integrated with a heater near the nozzle as shown in Figure 1.3. A current pulse of less than a few microseconds through the heater generates heat inside the ink chamber. The ink becomes superheated to the critical temperature for bubble nucleation. Often, for water-based ink, this temperature is around 300°C. When the nucleation occurs, a vapour bubble instantaneously expands creating a net positive pressure to force the ink out of the nozzle. Once all the heat stored in the ink is used, the bubble collapses on the surface of the heater. As the bubble collapses the channel forces helps the ink to break off at the nozzle and generate

a droplet towards the substrate. The ink then refills back into the chamber and the process repeats again.

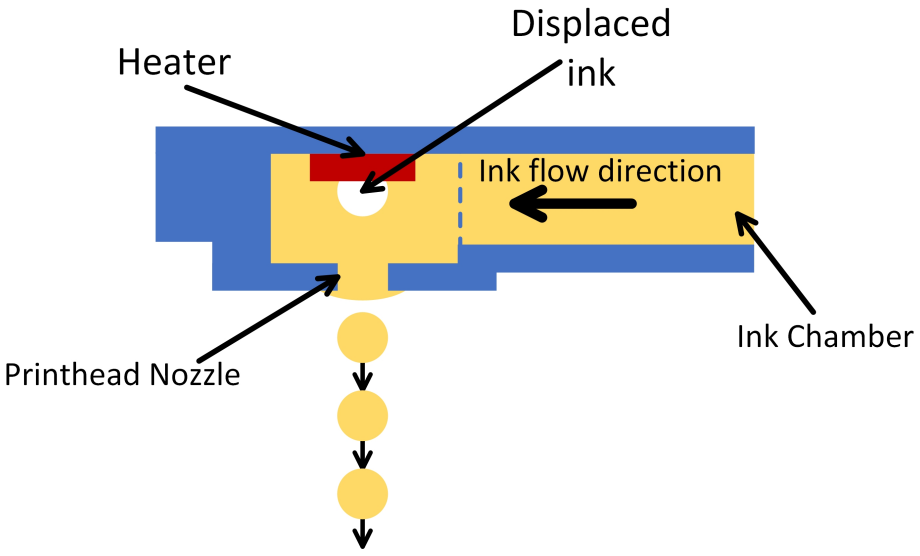

FIGURE 1.3: Thermal inkjet: Principle of operation

1.4.3 Aerosol Inkjet Printing

Aerosol inkjet printing is an aerodynamic focusing of ink particles on the planar and non-planar surfaces. The ink which needs to be deposited undergoes atomization either through pneumatic or ultrasonic atomizer into tiny droplets. The atomized aerosol is then focused by a coaxial sheath gas to deposit the particles on the substrate as shown in Figure 1.4. Focusing of aerosol reduces the jet diameter of the exiting ink particles from the printhead nozzle to achieve a fine resolution of up to 10 μm of printed features.

1.4.4 Acoustophoretic Inkjet Printing

Acoustophoretic printing is a drop-on-demand method capable of patterning liquid metals, optical lenses, and even cell laden droplets. This platform technology is uniquely suited for printing biopharmaceuticals, advanced material and many other liquids including honey. In this method a print nozzle is placed inside an acoustic resonator. The sound energy imparted by the acoustic resonator detaches the liquid from the nozzle. Separation of liquid is similar to the dripping behaviour of droplet from nozzle when an external force is applied however, the resolution is improved as the acoustic energy

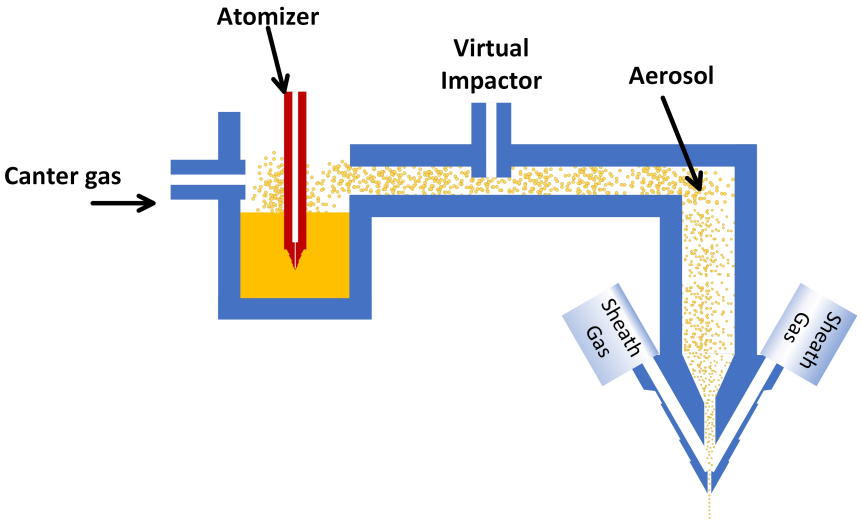

FIGURE 1.4: Aerosol inkjet: Principle of operation

initiates early detachment of droplet from the nozzle. The resolution of printing depends upon the acoustic force and the physical properties of the liquid.

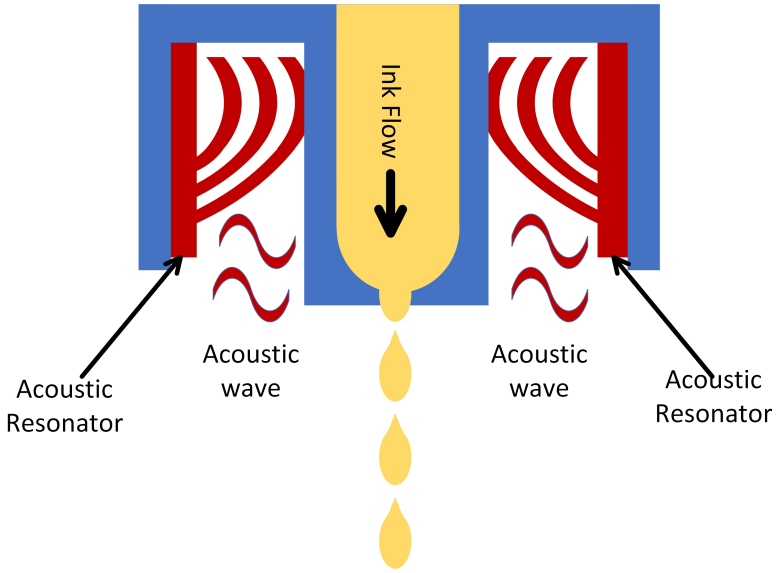

FIGURE 1.5: Acoustophoretic inkjet: Principle of operation

1.4.5 Electrohydrodynamic Inkjet Printing

Electrohydrodynamic (EHD) is a contactless printing method of ejecting the droplet by using a pull force generated by the counter electrodes placed at different potentials. The electric field generated by the counter electrode pulls the liquid from the nozzle. The force acts on the spherical shape of the meniscus of liquid outside the nozzle and transforms the shape of the liquid into a cone as shown in Figure 1.6. Thus, making a

conejet, which depends on the applied voltage, the distance between counter electrodes and the physical characteristics (such as viscosity, density, surface tension, etc.) of the liquid being ejected.

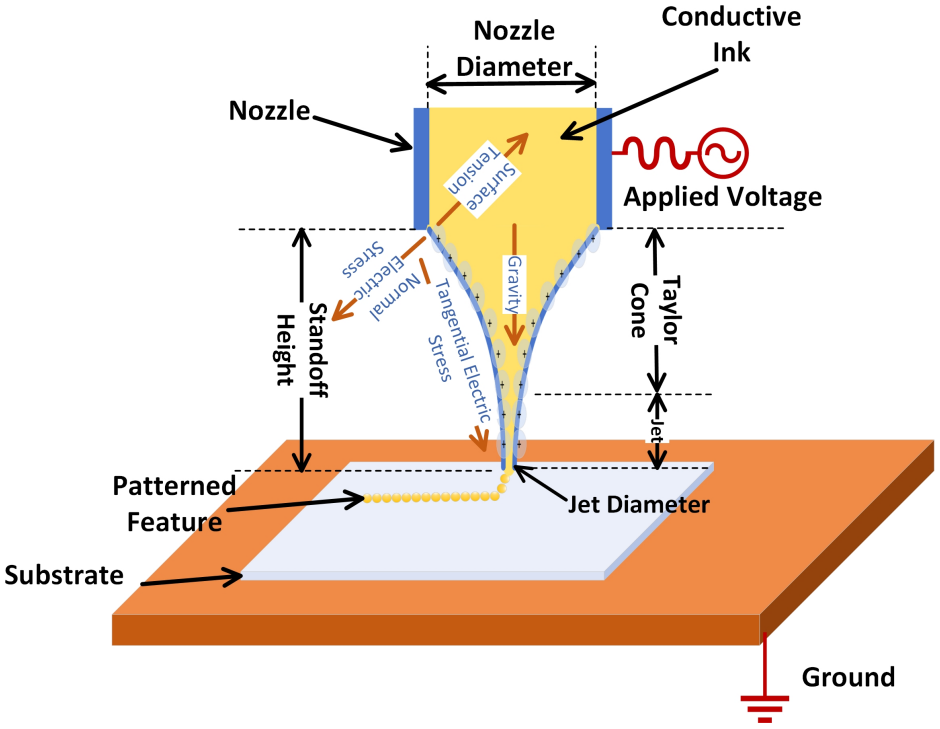

FIGURE 1.6: EHD inkjet: Principle of operation

1.4.6 Strengths and Shortcomings of Contactless Printing

Although the drop-on-demand droplet can be achieved through these technologies, there are still many challenges in the contactless printing for printed electronics. For instance, thermal inkjet works on the principle of forming a small bubble in the ink chamber by the heating element. Due to the application of heat for generating the on-demand droplet the method has two major drawbacks: 1) the use of ink which is susceptible to thermal degradation as the temperature is raised by the heating element, and 2) the ejected droplet is bigger than the size of the nozzle that leads to the printing resolution larger than the nozzle diameter.

Piezoelectric inkjet overcomes some of the issues related to the thermal inkjet printing such as printing without the application of heat inside the ink chamber and printing at higher frequency. However, the generation of droplets smaller than the size of the nozzle is still not possible. Moreover, the ink for the thermal and piezoelectric printers needs

to be tuned such that the printing can be done within the operating parameters. The main parameters are viscosity, surface tension, concentration of nanoparticles, size of nanoparticles and compatibility of the ink with the overall ejection mechanism.

Acoustophoretic printing can solve issues pertaining to the physical properties of ink as it can handle inks having higher viscosities and surface tension when compared to piezoelectric and thermal inkjet printing. However, it uses sound wave energy to detach ink droplets from the printing nozzle, the resolution of printing is still an issue. At best the droplet size equal to or greater than 65 μm could be produced through a nozzle size of 14 μm which is still four times higher than the nozzle diameter [22].

On the other hand, EHD printing provides a solution to most of the aforementioned challenges of other technologies and has gathered a lot of attention in recent times. EHD printing stems from the earliest EHD experiment performed by William Gilbert in the seventeenth century which showed the conical shape of the drop when the charged rod is taken closer to the sessile drop [23]. Further progress in EHD printing research has been fuelled by Taylor for his work on electrically-driven-jet [24]. Research published by Taylor has driven numerous applications of electrohydrodynamic in areas such as EHD inkjet printing [25, 26], electro-spraying [27–30], electrokinetic pumping [31, 32], polymer coatings [33, 34], facilitation of heat and mass transfer [35, 36], and in various biomedical applications [37–39]. The phenomenon of electrospray has been widely applied under vacuum to augment the atomization with dominant pulsating electrostatic forces as the gravitational forces are negligible. In electrospray application the control on the deposition of the drop is of little importance as the aim is to spread the droplet on the large surface.

The main advantage of EHD printing is that it can operate on liquids that have higher viscosities than those handled by either piezoelectric or thermal inkjet printing. Also, due to the shape of a cone, the ejected volume is much less than the conventional printing techniques. This results in better resolution during the printing process. However, for EHD printing the localized custom printing offers many challenges such as uniformity and even distribution of conductive nanoparticles in the ink colloid. These challenges are due to the change in meniscus shape as the liquid is ejected from the nozzle. To circumvent this issue a stable meniscus is maintained by the application of base voltage and external pressure with the help of syringe pump/pneumatic pumping as reported by

more recent EHD printing processes [8, 40, 41]. However, due to the varying nature of the ink physical properties rigorous experimentation is required for finding the optimal parameters for conducting an on-demand printing process through EHD for a particular ink.

Most of the work in the domain of EHD printing has been done with the focus of improving the resolution by reducing the size of nozzle. Nevertheless, the true potential of EHD printing could only be realised by using larger nozzles that would allow ejection of higher concentrations of metallic conductive particles along with good printing resolution which is challenge in other contactless printing methods.

1.5 Thesis Layout

This thesis by publications is organised as follows:

Chapter 2 provides a detailed overview of the proposed EHD printhead design, experimental results and analysis of the printed features. This work was published in the International Journal of Advanced Manufacturing and Technology.

Chapter 3 highlights the design and development of the environmental humidity sensors by using the laser ablation process. This work has been prepared for submission to Nature Scientific Reports.

Chapter 4 presents a thorough study on the issues associated with EHD printing. This work has been prepared for submission to MDPI Polymers.

Chapter 5 details a comprehensive study on the characterisation of fused deposition based microchannels to be used in microfluidic applications to complement the work on sensor fabrication. The results attained from the experiments were compiled and published in MDPI Micromachines journal.

Chapter 6 summarizes this thesis and discusses the future work.

Chapter 2

High resolution electrohydrodynamic printing of conductive ink with an aligned aperture coaxial printhead

2.1 Abstract

Electrohydrodynamic (EHD) printing is a promising inkjet technique to generate smaller droplet sizes due to the formation of a Taylor cone. However, the process is intricate and involves the fabrication of a printhead having a smaller nozzle diameter. Notable examples are present in the literature regarding printing through EHD but the underlying phenomenon which is responsible for generating the smaller droplet is obscure. In this work, we present a methodology which highlights the importance of nozzle shape which can govern smaller droplets even with a large head diameter. The work achieves a resolution of less than 2 μm by fabricating the inkjet head using simple techniques and off-the-shelf inexpensive needles of nozzle diameter ranging from 500 μm to 250 μm. The study of various nozzle profiles resulted in a printed resolution which is 50 times smaller than the nozzle diameter. Moreover, the study also highlights the importance of the wetting area profile of the nozzle and explains the role of printhead design which facilitates fine resolution printing of conductive tracks which until now seemed to be obscure.

2.2 Introduction

High resolution conductive printing without the need of a cleanroom and conventional photolithography process which requires fabrication of mask and subsequent etching is highly desirable. Microscale printing with on-the-fly customization for small batch fabrication of printed electronics and flexible sensors development has received tremendous attention [42–45].

Primarily, the key printing technologies can be divided into contact and contactless printing [9, 10]. In contact printing the impression of roll generates the features on the substrate. Depending on the process whether the impression engraves or penetrates the ink on the substrate the process can be differentiated by physical phenomenon responsible for generating tracks or features in the substrate. Screen, offset, flexography, gravure and pad printing are examples of contact printing, whereas aerosol, thermal, piezoelectric, electrohydrodynamic and acoustic inkjet printing are the prominent contactless inkjet printing methods. Contact printing technology is widely used in the paper industry and print media. The advantage of these printing methods is their high throughput with accuracies up to 50 μm, with gravure printing reaching higher resolution and high aspect ratios [11]. Almost all the contact printing methods utilize the roll-to-roll technology to transfer the base pattern on the substrate. But registration control, in the case of tight tolerances, can be a challenge. High velocity and pressure on the substrate in contact printing causes the flexible substrate to stretch, resulting in the design of complex registration algorithms [12–15] for aligning the next feature printing on the substrate. The cost of product fabricated through contact printing is cheaper per unit than the contactless printing method due to high throughput for large production batches [16–19]. However, for small production batches, the cost per unit is much higher than contactless printing [20, 21] and incorporating design changes requires changes in the impression features of roller which is often expensive and complex. Moreover, the overall printing process produces ink wastage at various stages of printing. Inkjet printing has certain advantages in a printed electronic application. Not only is it a contactless printing method but it also has a fabrication process which allows the pattern printing to be in a discrete or continuous manner depending upon the selection of the inkjet process. Among inkjet printing, electrohydrodynamic (EHD) printing offers high throughput [46], fine resolution of print feature [47], drop-on-demand printing,

continuous printing and spraying [48–51] and ability to print with inks having high viscosity [52–54] and thermal stability issues [55–58]. In EHD printing the driving force for ejecting the droplet is governed by electrostatic potential. Ink nanoparticles in the ink chamber are charged by an electrode subjected to the positive or negative potential where the counter electrode is placed under the ejecting orifice and provides the pull force necessary to produce droplets from the printhead. Due to the reverse polarity or grounding effect of the counter electrode, the ink/liquid in consideration experiences a shear force and forms the cone jet shape which is referred as the Taylor cone [59]. Recent developments in EHD printing are attributed to the contribution of the leaky dielectric model proposed by Saville [60]. The initial EHD printing concept and working device as presented by Choi et. al [61] dates back to 1998. And the first notable work in the area of fine resolution EHD printing was done by Roger et. al. by pulling a constant diameter of glass capillary through a heater and producing the necking between the two firmly held ends of the capillary by applying tension force. The force and heating zone are controlled in such a manner that a gradual decrease in the diameter of the nozzle is produced and finally the glass breaks to produce two sets of small diameters of nozzles. The final diameter which the glass nozzle achieved was about 2 μm. The printed line resolution was 3 μm and the printed dots were in the range of 490 nm [62]. Although EHD printing provides the aforementioned benefits, achieving them requires intricate printhead designs. Furthermore, most of the efforts in the past were targeted towards achieving high resolution printing by decreasing the size of the nozzle. For this reason, nozzle sizes less than or equal to 10 μm were used in various published articles for achieving printing resolution less than the size of nozzle [63–68]. In this paper, we present the study of various needle profiles which augments better resolution by understanding the hydrodynamic effect of the nozzle tip and by incorporating these profiles in the printhead which to date to the best of our knowledge have not been explored in general. The overall design improvement resulted in achieving a resolution of printing in continuous EHD printing mode of up 10 μm with a nozzle diameter to printed feature ratio of 1:50 on an average basis for three different printheads. However, our aligned aperture design based on the spinal needle type-D printhead resulted in the smallest resolution of 1.85 μm at the optimal applied voltage and flowrate parameters. The achieved ratio of the proposed printhead nozzle diameter to the printed lines was around 270 times, which to-date is the highest to the best of our knowledge.

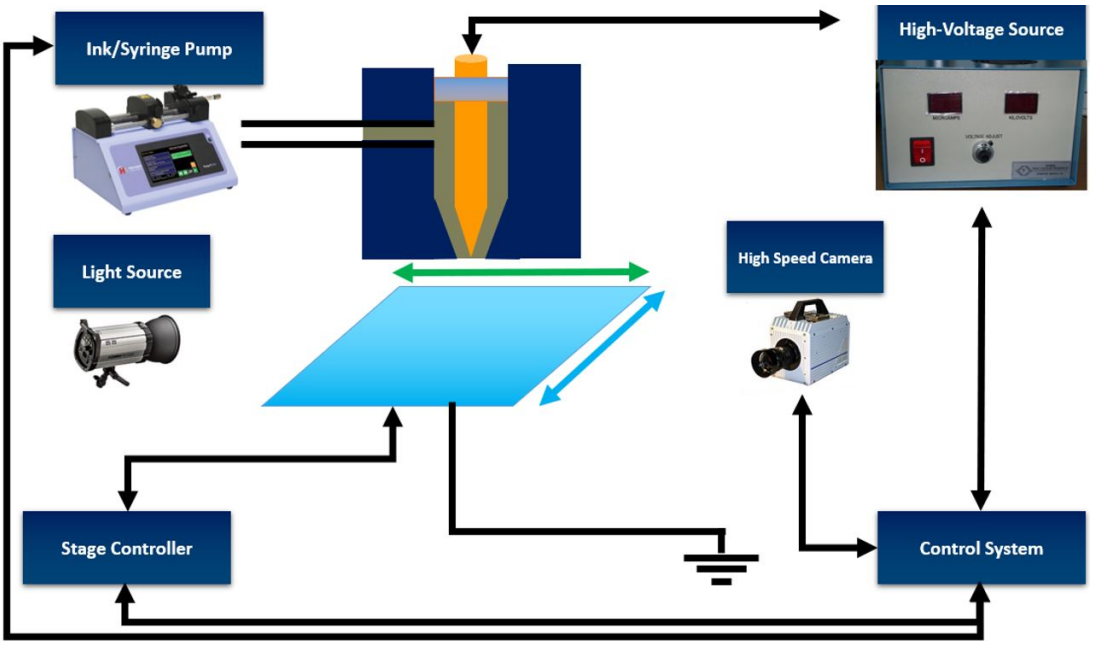

FIGURE 2.1: Schematic of the EHD printing setup.

2.3 Materials and Method

2.3.1 Experimental system

The schematic in Figure 2.1 outlines the overall EHD setup. The EHD setup includes a high-voltage DC power supply from Gamma High Voltage Research Inc. USA , a ground electrode mounted on the high precision X-Y stage from Applied Scientific Instrumentation USA along with its motion controller, a syringe pump from Harvard Apparatus USA, a high intensity fibre optics illumination from Edmund Optics USA and a high-speed camera from Kron Technologies Inc. Canada for visualization. Brief specifications and models of the overall setup are mentioned in Table 2.1.

2.3.2 Preparation of materials and substrate

In this work, a 4 mil (101.6 μm) PET substrate was used for printing the conductive lines. The substrate was mounted on the copper plate on which small holes of diameter 0.5 mm were drilled. The plate was then fixed by means of screws onto an aluminium machined plate which is connected to the vacuum pump. Once the vacuum pump is in operation it creates the vacuum which then holds the substrate firmly when placed over the copper plate as shown in Figure 2.2. To avoid the sagging of the substrate under

TABLE 2.1: EHD printing system component specification

Equipment	Model	Brief Specification
DC Power Supply	D-ES50PN -20W	0 to 50 kV DC, 400μA
XY Stage	MS-4400	XY Travel:100x 100 mm Resolution: 22nm Repeatability: <700 nm
Z Stage	MS-4400	Z Travel: 100 mm Resolution: 50nm Repeatability: <$\pm$100 nm
Motion Controller	LX-4000	XYZ stage Motion controller
Syringe Pump	11 Pico Plus MA1 70-2213	Min. Flowrate: 1.3 pl/min with 0.5μl syringe
High Speed Camera	Chronos 1.4	Min. Res:336x96@38565fps Max. Res:1280x1024@1057fps
High Intensity Illuminator	MI-150	Power: 150 W EKE Quartz Colour Temp.(K):3200 Power: 150 W EKE Quartz Colour Temp.(K):3200

vacuum a 3D printed pillar plate was inserted between the aluminium suction plate and copper cladded printed circuit board (PCB) plate. Holes on the copper cladded plate were drilled with the help of a ProtoMat S62 PCB milling machine by LPKF Laser & Electronics, USA, at a spacing of 10 mm with the offset distance of 5 mm to the next row on a length of 100 mm by 100 mm. Thus, the overall substrate which can be held firmly on the X-Y stage was around 100 mm x 100 mm. The thickness of the copper cladded PCB plate was 1.2 mm with a copper thickness of 35 μm.

Before fixing the copper plate to the vacuum chamber the copper plate was finely sanded to remove any burrs or unevenness which can occur due to the drilling of the minute holes for the vacuum. The copper plate was then connected to the ground electrode for the electrohydrodynamic ejection of liquid from the nozzle.

Parameters of the conductive ink are mentioned in Table 2.2. The ink was delivered to the nozzle with the help of piping of 0.19 mm diameter connected with the syringe pump. Commercial off-the-shelf hypodermic nozzle tips were removed from the Luer lock hub of these needles and connected to the piping. This is to avoid a volume of printing ink becoming trapped inside the Luer lock hub. All these modifications resulted in the

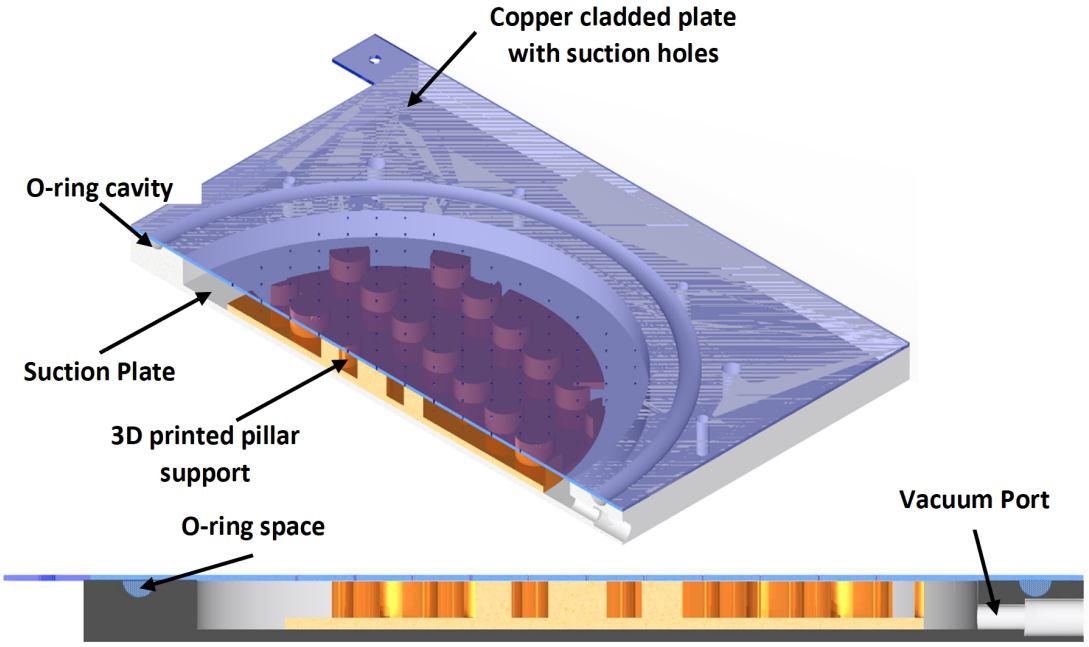

FIGURE 2.2: Substrate mount for the EHD process consisting of suction plate with micro holes on copper cladded plate

TABLE 2.2: Parameters of printed ink

S.No.	Parameter	Value
1.	Specific gravity	1.63
2.	Surface Tension	20.00 dyne/cm
3.	Viscosity	10.6 cP @ 20 °C
4.	pH	5.6
5.	Average particle size	47 nm
6.	% Silver nano particles	≈40%
7.	Solvent	Diethylene glycol

precise control of flowrate and instantaneous changes in the shape of the meniscus were observed as the flowrate from the syringe pump was changed.

Four different experimental setups were prepared for conducting the series of experiments for comparison and to investigate the profiles which govern the best possibilities for the ease of printing of the conductive ink. Print nozzle holders were fabricated by 3D printing and aligned with the stage with an accuracy of ± 5 μm. The accuracy was tested by traversing the needles across the stage and visualizing it on the highspeed camera setup. A custom application in C# was written to control the movement of the stage where the needle was kept static during the whole printing process once the vertical distance with the Z-stage was fixed before the printing process. Table 2.3 details the different printed ejection profiles investigated in this study.

TABLE 2.3: Design of printhead for EHD system

S.No.	Nozzle Ejection Schematic	Nozzle/Outlet Diameter	Remarks
Type A.		ID: 250 μm	Conventional hypodermic needle of 25 Gauge with ID of 250 μm and OD of 500 μm
Type B.		ID: 250 μm	Spinal needle of 25 Gauge with ID of 250 μm and OD of 500 μm
Type C.		Nozzle: 500 μm	500 μm nozzle with hypodermic needle of gauge 31. Tip diameter of needle of around 5μm
Type D.		Nozzle: 500 μm	500 μm nozzle with spinal needle introducer. Tip diameter of needle of around 10 μm

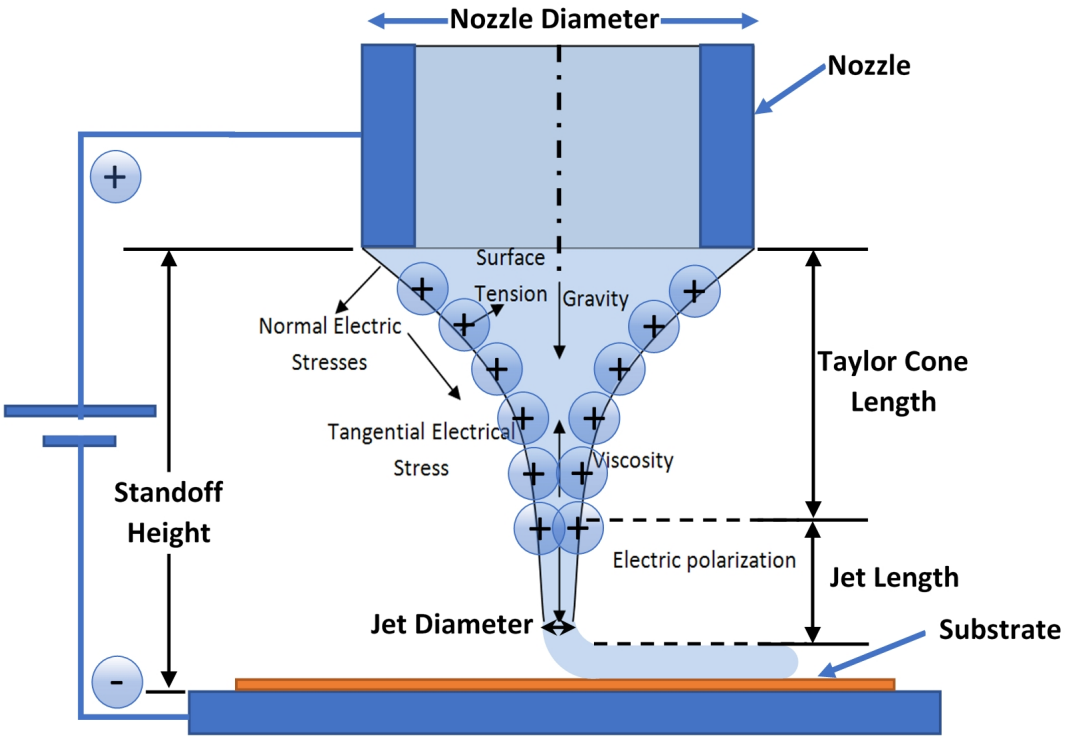

FIGURE 2.3: Forces acting on conducting ink during EHD printing

2.3.3 Printhead Design

This study aims to understand the profiles which can be easily fabricated without the need of special tools or processes. This is to enable EHD printing for various applications, offering fine resolution, repeatability, and ease of maintenance. To understand the parameters of the printhead design it is important to understand the forces acting on the liquid under the influence of an electric field as shown in the schematic diagram (Figure 2.3)

Under the influence of the electric field the liquid experiences dilation in the form of a cone. When the same liquid is outside the nozzle the capillary forces are insignificant. In this case, electrical stresses only need to overcome the surface tension and thinning of the jet diameter occurs with the decreasing distance of the jet from the counter electrode. Smaller standoff height and nozzle size enhance the ejection behaviour of the droplet as the length over which surface tension acts decreases. However, decreasing the size of the nozzle creates issues of high wall forces, blockage of nozzles, the limitations of the ink to be used and, eventually, limited reusability of the printhead. According to Choi et al. [69], jet diameter d_j is proportional to the anchoring diameter of the nozzle d_n, under the influence of electric field E on the ink having surface tension γ on the continuum media of absolute permittivity ε_0 and is expressed as

$$d_j \approx 1/E\sqrt{\gamma d_n/\varepsilon_0} \tag{2.1}$$

Equation 2.1 indicates that as the diameter of the nozzle decreases the jet size of the cone jet also decreases resulting in smaller droplet size. Methods other than reducing the diameter of the nozzle are not explored extensively, in particular, using two sets of nozzles so that a primary nozzle is used to transport the ink/fluid and secondary nozzle for the ejection of the droplet. Here, we present the concept of aligned aperture coaxial nozzles by using a Y-shaped / T-shaped construction of printhead. This construction allows the ink chamber to be large enough to transport the ink of diverse physical, chemical and rheological properties. The construction of the EHD printhead is such that the droplet ejection tip is not in-plane with the inlet of the ink, using a smaller needle diameter than the primary nozzle allows the ink to flow in between the aligned coaxial nozzles. We designate the primary nozzle as the aperture or opening for liquid as well as the secondary nozzle. This extension of the secondary nozzle enables the ink/liquid to create adhesion with the tip profile of the secondary nozzle. The secondary nozzle profile and apex point can facilitate the ejection behaviour of the droplet. Since the primary and secondary nozzles are at the same electrical potential, therefore the secondary nozzle can take advantage of the meniscus formed by the primary nozzle and further reduces the jet diameter due to its small anchoring diameter. This type of aligned construction of printhead is simple to fabricate and allows greater control on the secondary nozzle tip/profile compared to previously reported EHD systems [70]. In our work, we have

demonstrated that aligning the cone formed by the primary nozzle provides a very good resolution of continuous EHD printing with the printed feature approaching that of many reported drop-on-demand EHD systems. All the modifications provide a simpler continuous EHD printing which can use a large ink capillary thus solving the bottleneck of the smaller diameter of the nozzle, making the EHD system more feasible in biomedical applications where the liquid is highly viscous, is composed of myriads of sub-particles, and contains sol-gel phases. A printhead with two different profiles has been used in this work. First, a comparison of the hypodermic and spinal needle profiles has been done and, later, the same profile tips were used in a coaxially aligned aperture printhead in which the second nozzle is extended at the end of the Taylor cone which is about 450 μm further from the 500 μm internal diameter of the primary nozzle. Profiles of the two different secondary nozzles are illustrated in Figure 2.4.

Figure 2.4 shows that the distance from bevel opening to the tip of the nozzle of the hypodermic needle is about 53% more than the spinal needle. In our work, we demonstrate that the anchoring diameter of the liquid depends on the distance from the opening of the nozzle (bevel length) to the tip and can be changed by aligning a secondary nozzle at the centre of the primary nozzle with different profiles of jet resolution facilitating tips.

2.3.3.1 Type A & B: Hypodermic & Spinal needle profile printhead

This is the simplest printhead configuration in which a 25-gauge needle is connected to the ink through a fluidic line which is then connected to the syringe pump. In this printhead, hypodermic needles were used to understand the behaviour of the ejecting droplet and the needle profile/shape. A 25-gauge hypodermic needle was connected to the fluidic adaptor by cutting the needle tips with the help of a Dremel tool and inserting the same in the fluidic adaptor. Since the outer diameter of the needle was 0.5 mm, which is much greater than the fluidic line internal diameter of 0.19 mm, it creates enough pressure on the internal walls of the connected fluidic line to avoid any leakages. Figure 2.5. shows the holder of the hypodermic needle with the fluidic system and overall tip shapes of the hypodermic and spinal needles. The attachment of the

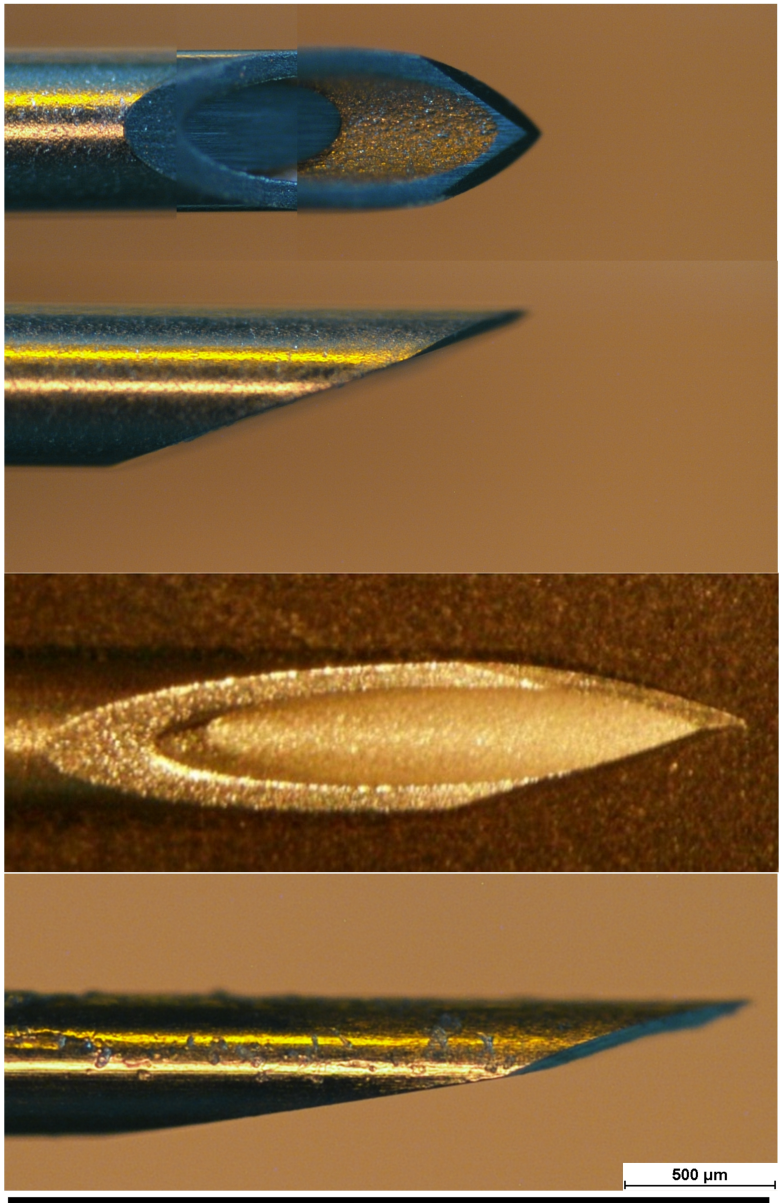

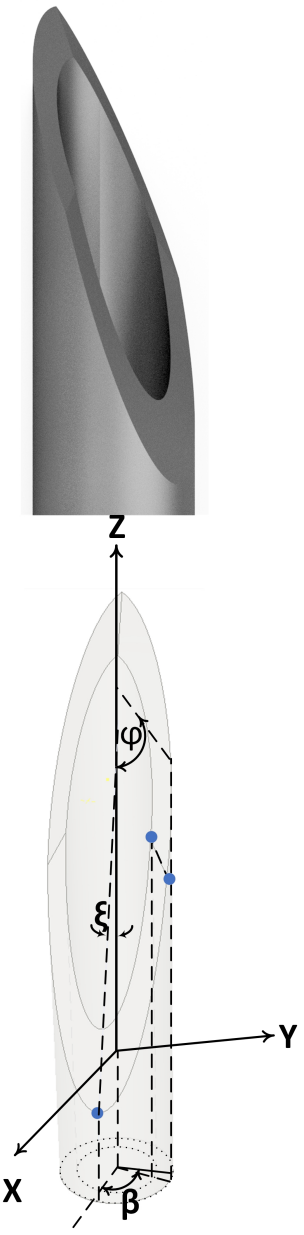

Needle Type	ξ	φ	β	Bevel Length (mm)
Hypodermic	12°	18°	60°	1.5
Spinal	23°	23°	10°	0.8

FIGURE 2.4: Needle profiles used in the experimentation

needle and the fluidic channel was printed out of a fused deposition modelling (FDM) 3D printer, demonstrating that overall visualization from the camera system is possible. The outer diameter of the 25-gauge needle is 0.5 mm and inner diameter of the needle is 0.25 mm. The hypodermic needle used in this work was from Becton Dickenson which has 5 profile cuts at the tip of the needle instead of three sharp cuts which conventional hypodermic needles have. Additional cuts improve the insertion of the needle into the skin. When the liquid is exposed to atmospheric pressure, the liquid from the exit of the nozzle swells considerably more than with the blunt spinal needle. This is due to the longer distance between the sharpest end of the nozzle of these needles. In our subsequent discussion, it will be evident that the tip profile, the liquid exit distance from the tip of the nozzle, and the ability to dilate the liquid to the tip have considerable effects on the printing results of different printheads. As these nozzles are commercially available - thus providing consistent geometry for every batch - the overall EHD printing system is easy and cheaper to establish when compared to many reported glass nozzle EHD systems. Moreover, little or no comparison has been reported in the literature regarding the exit shape of the nozzle with respect to printing performance. Therefore, the results presented in this work are noteworthy from the point of view of establishing future EHD systems.

2.3.3.2 Type D & E: Aligned aperture hypodermic, sharp needle and spinal needle introducer profile printhead

In this type of EHD printhead, a nozzle holder was fabricated in such a way that the needle tips exit the nozzle in a telescopic extension of one needle sliding inside another needle. The aim was to study how the printing resolution is affected when a needle is introduced at the apex point of the meniscus of the Taylor Cone [71–73]. In this regard, a 0.5 mm 3D printer nozzle was used as the ink chamber and subsequent ejection nozzle. A 25-gauge needle with an external diameter of 0.5 mm is inserted in the 0.5 mm 3D printer nozzle. The matching of the internal diameter of the 3D printer nozzle and the external diameter of the 25-gauge needle facilitates the central alignment of the inserted needle. Inside the 25-gauge nozzle, a hypodermic nozzle is inserted making a telescopic extension of the 25-gauge nozzle. It is pertinent to mention that the 25-gauge

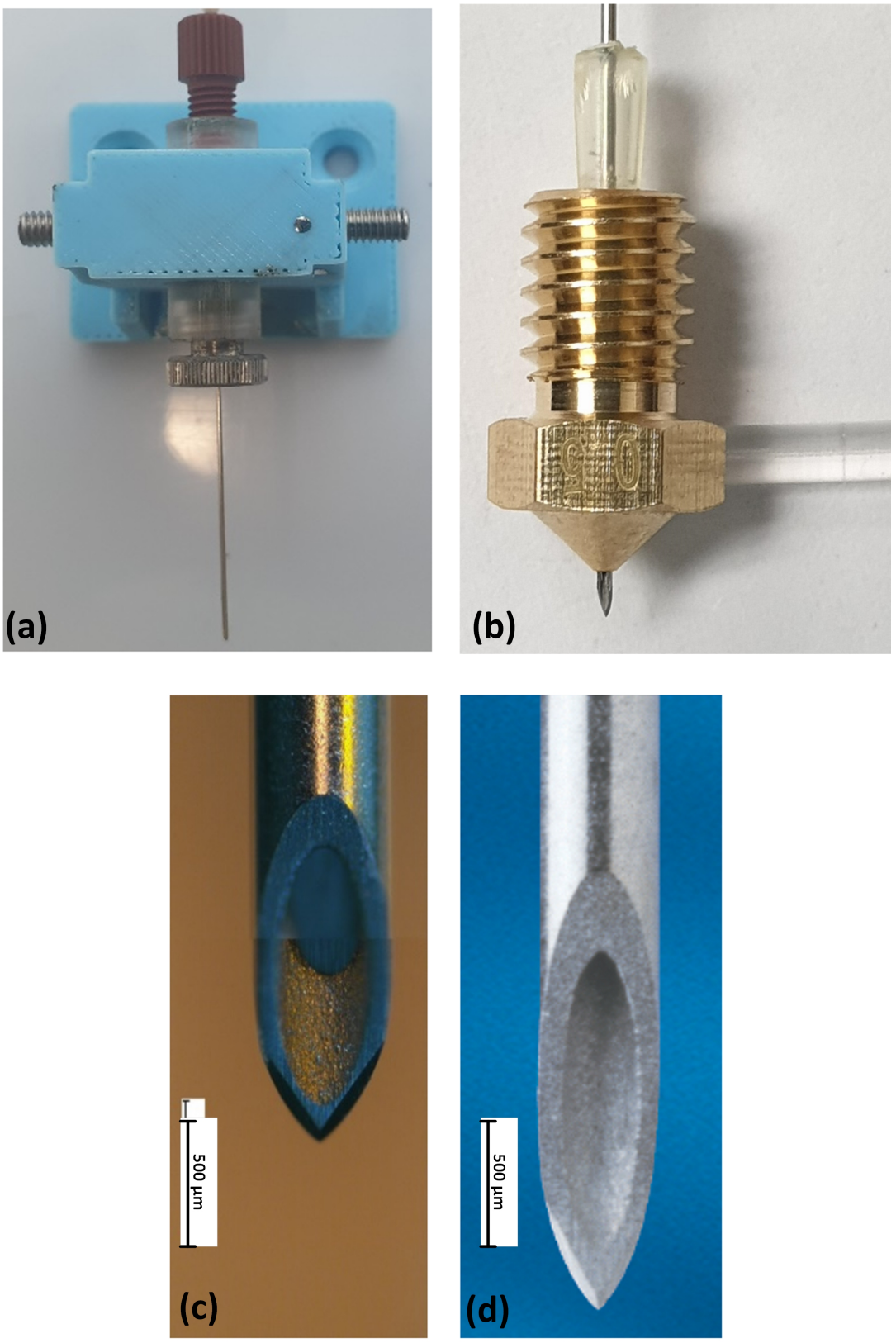

FIGURE 2.5: (a) Fluidic connection with the needle for Type A and Type-B printheads (b) Fluidic connection with the needle for Type C and Type-D printheads (c) Hypodermic needle profile of Type-A and Type-C printhead (c) Spinal needle profile of Type-B and Type-D printhead.

nozzle is not connected with the fluidic line. Instead, the connections were made with the 3D printer nozzle. Before inserting the nozzle, a fluidic line was connected to the 3D printer nozzle by filling the cavity with Polydimethylsiloxane (PDMS). The PDMS mixture consisted of a SYLGARD™ 184 silicone elastomer base and a curing agent from Dow Corning, USA. The mixture ratio of curing agent to the silicone elastomer was ten-parts base to one-part curing agent by mass. The PDMS helps the 25-gauge needle to hold firmly at the centre of the 3D printer nozzle, and the elastic properties of the PDMS exerted enough pressure on the needle walls to avoid any fluid leakage from the top of the nozzle. The internals of the ink chamber, the overall EHD system, and the 3D printed holder are shown in Figure 2.6.

2.4 Results & Discussion

Several experiments with different printhead designs were conducted to evaluate the best configuration. The stable conejet of each configuration depends upon the standoff distance (distance between the nozzle and counter electrode), flowrate, printing speed and applied voltage. Since the printing feature of each configuration was different, the flowrate was adjusted accordingly to perform the printing [63–68, 74, 75]. In order to perform a direct comparison in all our experiments, the distance between the nozzle and counter electrode was adjusted to 350 μm, printing speed was set to 2 mm/s, voltage was varied between 1.1 to 1.5 kV, and flowrate was also varied from 5 nl per minute to 12 μl per minute. The same 4 mil (101.6 μm) PET substrate from 3M was used. Moreover, a continuous DC voltage was used for the printing process instead of AC pulsed voltage. This is to demonstrate that continuous EHD printing can also be used for fabricating a conductive pattern at a fine resolution. In sensor applications the continuous line of a transduction electrode is required to provide the sensor output to the readout circuit [20, 76, 77]. The results tabled below provide a comparison of each type of fabricated printhead.

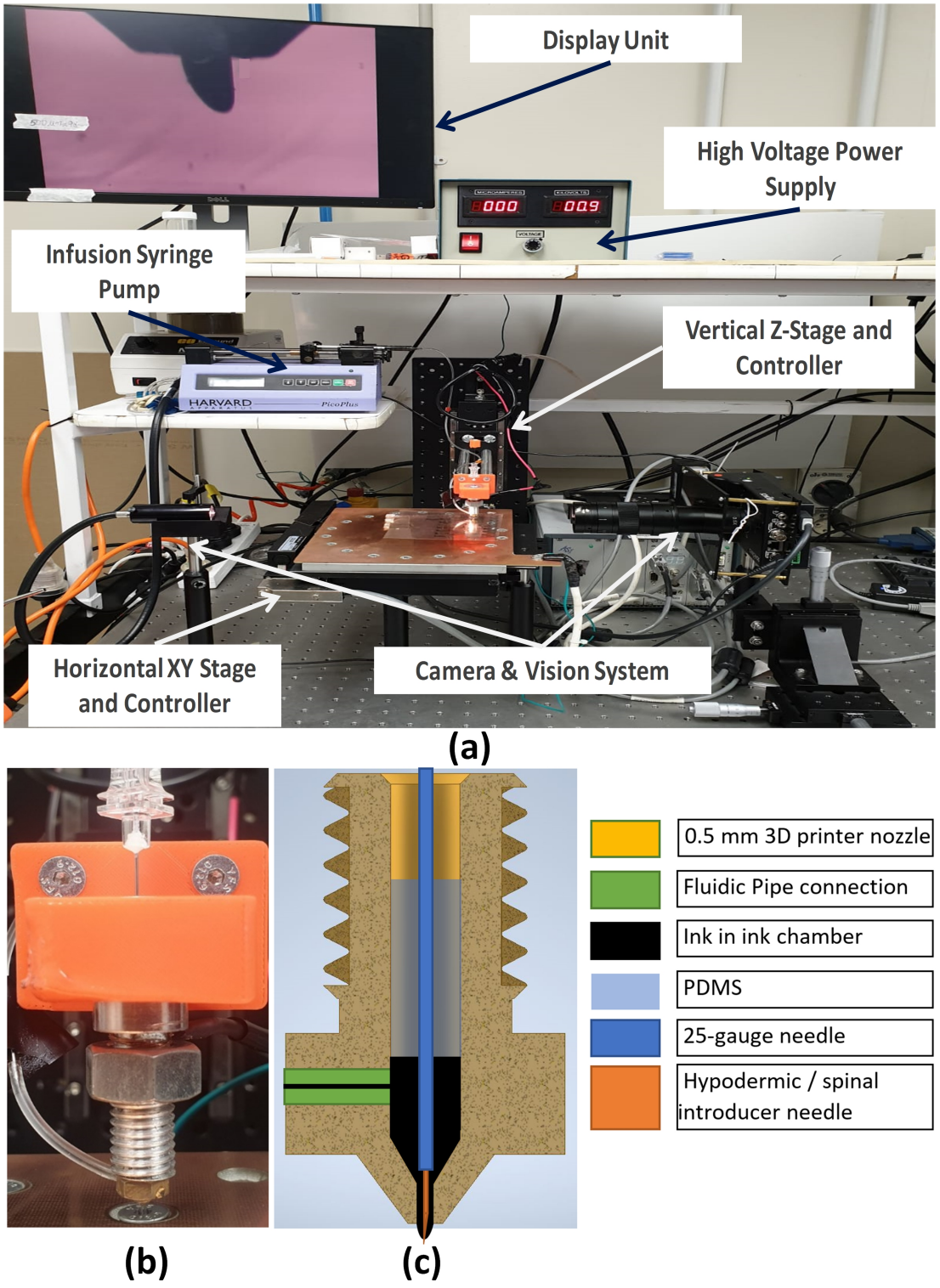

FIGURE 2.6: (a) EHD system and printhead assembly (b) FDM copper nozzle integration with fluidic line (c) Schematic of Type C & Type D aligned aperture sharp needle with introducer and hypodermic EHD printhead

TABLE 2.4: Printed line resolution of Type A and B printhead parameters

Printhead Type	Flowrate (μl/hr)	Voltage (kV)	Line width (μm)
Type A	40	1.5	≈65
Type A	50	1.5	≈75
Type A	65	1.5	≈82
Type B	30	1.5	≈32
Type B	40	1.5	≈47
Type B	55	1.5	≈56

2.4.1 Type A and Type B Hypodermic and Spinal Needle Printhead

In the Type A printhead which consists of the hypodermic needle the ejection voltage at the standard standoff height of 350 μm was 1.5 kV. Figure 2.7 shows the width of the printed lines at optimal flow rates from 30 μl per hour to 65 μl per hour. Under optimal conditions the conejet formed from the printhead is stable and consistent printing is performed. However, the line width increases with increasing the flowrate due to the availability of more volume at the tip of the nozzle. Thinning of the jet diameter is observed when the flowrate is low and in the stable conejet region. On the contrary, higher flowrate results in thick jet diameter and wider line widths. The distance from the ejection of the needle was greater than for the spinal needle; smooth ejection was noted in the case of continuous electrohydrodynamic printing. When the Type A was replaced with the Type B spinal printhead consisting of a 25-gauge needle, the printing resolution improved (Figs. 2.7, 2.8 and 2.9). Table 2.4 shows the variation in droplet size during the two different printing modes.

It is evident from the results that the spinal needle has better resolution of printing of the order of around 2. This is due to the improved dilation of liquid at the tip of the nozzle. The momentum of liquid in the case of the hypodermic needle is greater when it reaches the sharpest point of the needle. Even though the tip of the hypodermic is sharp and has the same tip width as that of the spinal needle, the overall printing width is higher. From this finding it can be established that the tip angle or distance from the nozzle exit to the tip of the nozzle (bevel length) has considerable influence on the printing resolution.

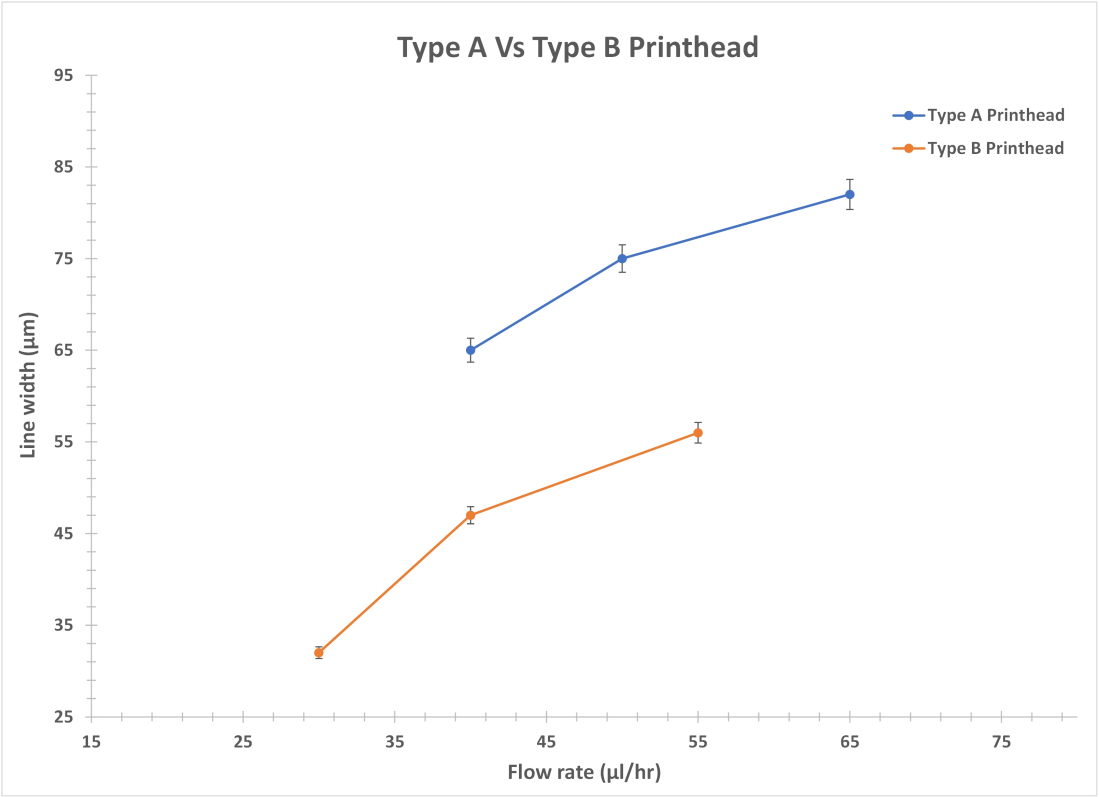

FIGURE 2.7: Flow rate vs line width for Type A and Type B printheads

2.4.2 Type C & D Aligned aperture printheads

Type C and Type D printheads are based on the 3D printer nozzle. A hypodermic needle of gauge 31 was used in the Type C printhead nozzle and a spinal needle introducer of 200 μm diameter having the profile of a spinal needle was used with the Type D printhead. The introducer can be considered as the wire inside the 25-gauge needle, but the end shape of the introducer matches the spinal needle profile. The difference between the two profiles is the tapered angle of the needle to the apex of the needle tip. The hypodermic needle angle is sharper than the angle of the spinal needle due to the ink having to travel further from the nozzle exit to reach the tip. Table 2.5 and Figure 2.10 show the printed line width at a standoff distance of 350 μm and printing speed of 2 mm/s. The optical and scanning electron microscope (SEM) images shown in Figs. 2.11 and 2.12 depicts a transition from larger line width (for Type C printhead) to the smallest achieved linewidth (for Type D printhead).

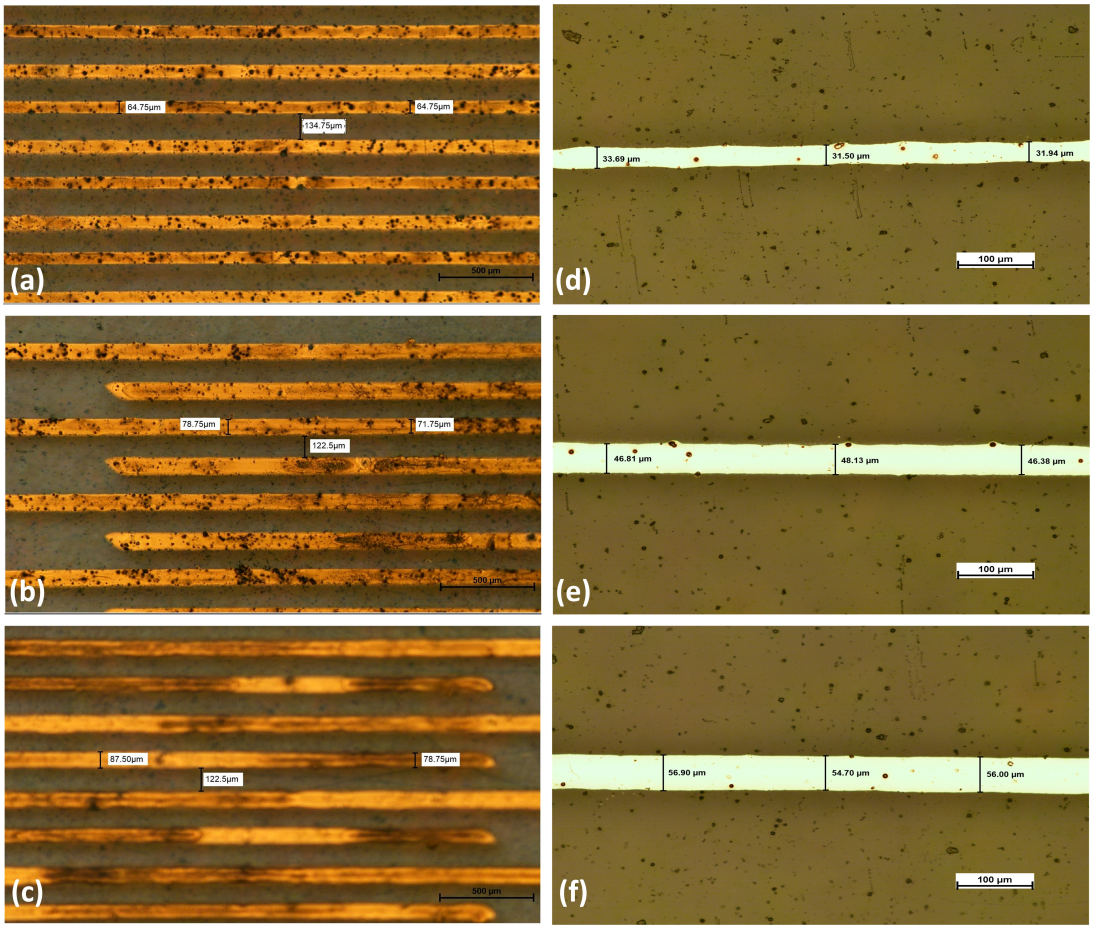

FIGURE 2.8: Optical images of printed lines with (a-c) Type A and (d-f) Type B printheads

TABLE 2.5: Printed line resolution of Type C and D printhead parameters

Printhead Type	Flowrate (μl/hr)	Voltage (kV)	Line width (μm)
Type C	0.4	1.5	≈6
Type C	8	1.5	≈29
Type C	20	1.5	≈46
Type D	0.35	1.5	≈2
Type D	0.85	1.5	≈3
Type D	7.5	1.5	≈13

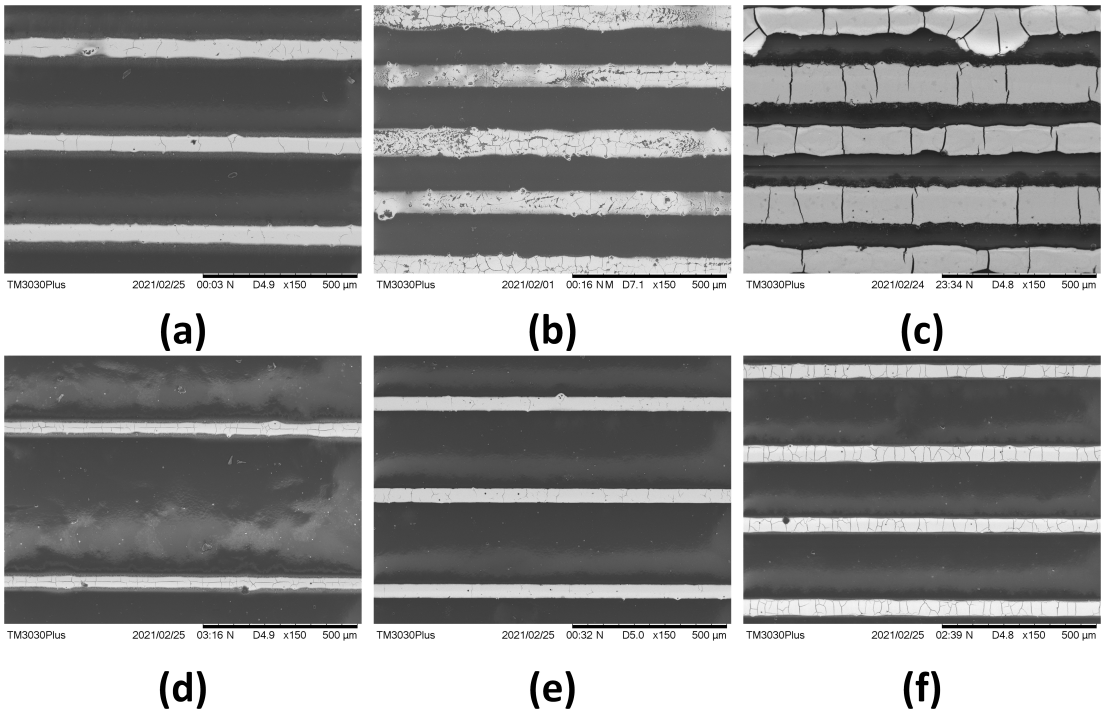

FIGURE 2.9: Scanning electron microscopes (SEM) images of printed lines with (a-c) Type A and (d-f) Type B printhead

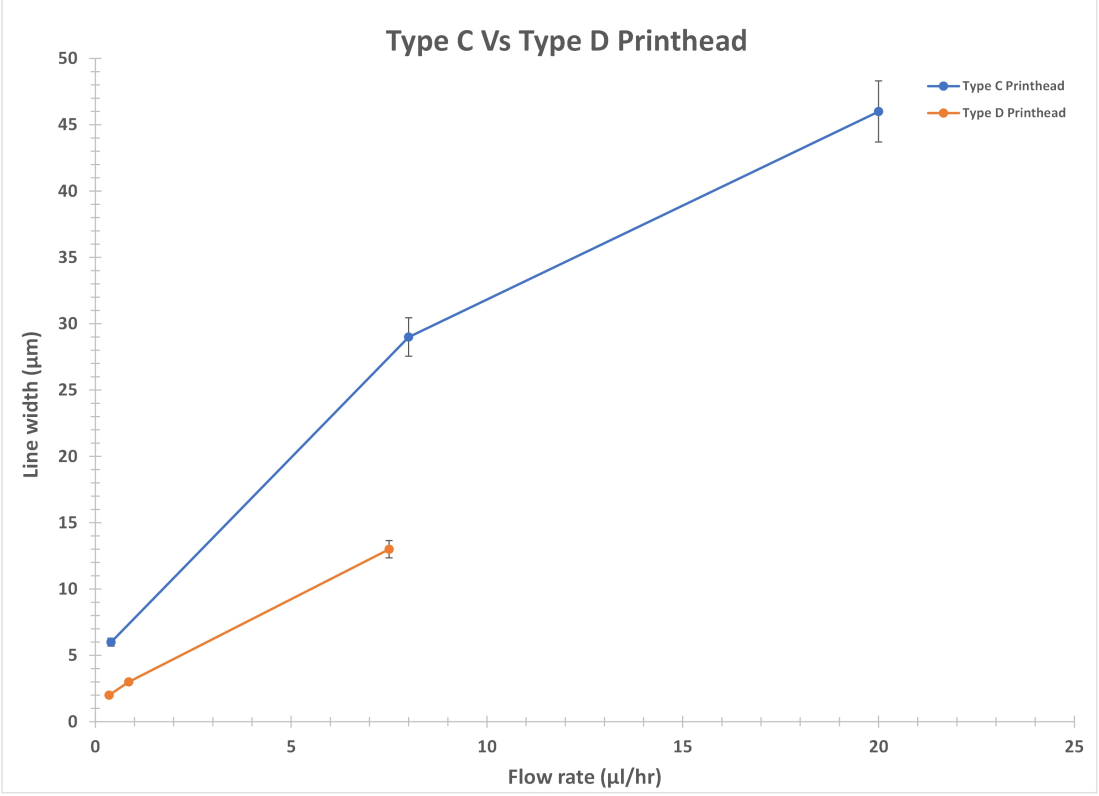

FIGURE 2.10: Flow rate vs line width for Type C and Type D printheads

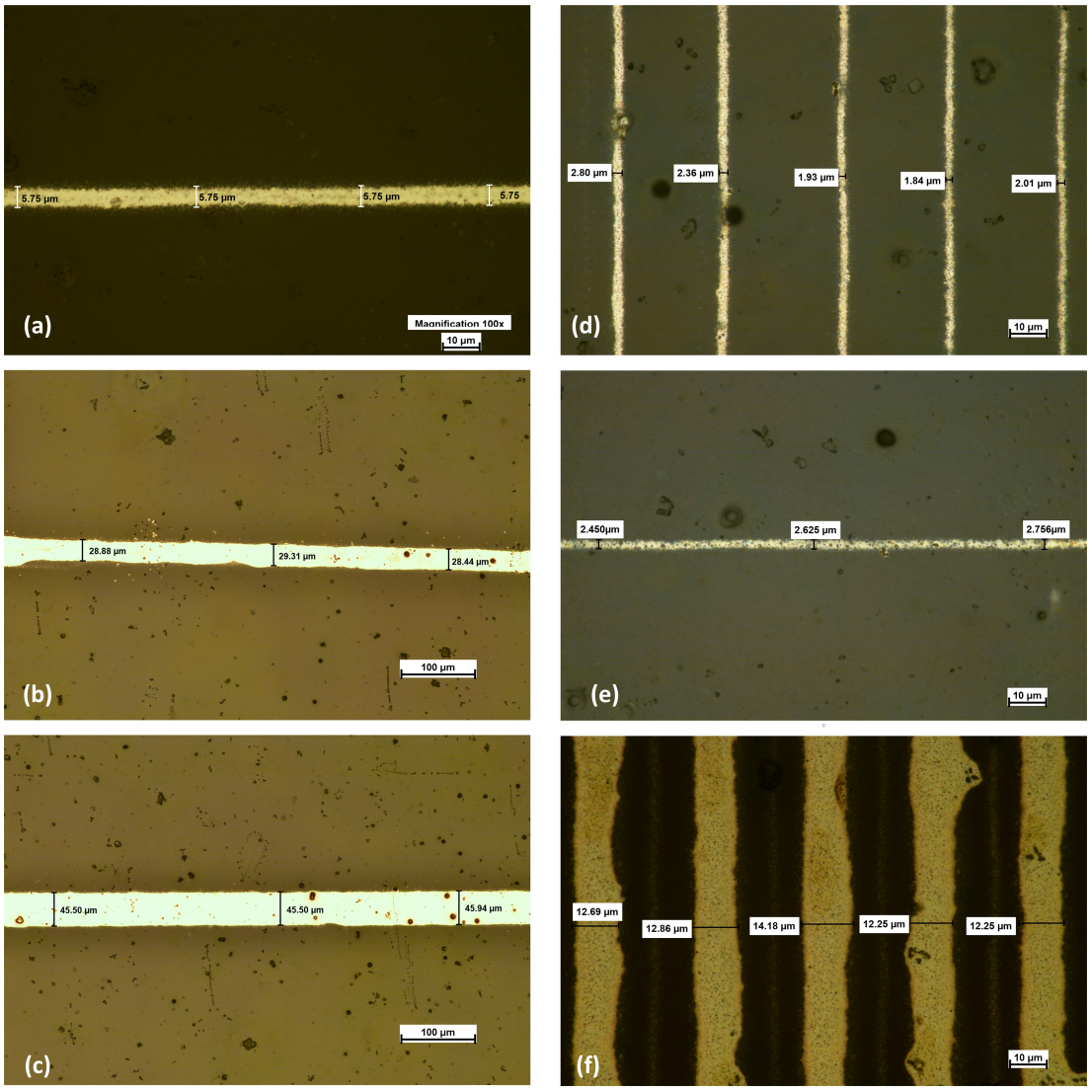

FIGURE 2.11: Optical images of printed lines with (a-c) Type C and (d-f) Type D printheads

The short ink dilation distance from the apex of the nozzle, and the forces required to eject the droplet from the tip of the nozzle, are relatively small when compared to other profiles as described in the literature and as tabulated in Table 2.1. The overall achieved droplet size and the width of the printed line is smaller. This is achieved as the meniscus is already formed at the tip of the nozzle and the apex of aligned aperture needle acts as a trigger to generate a smaller droplet due to the concentration of the electric field

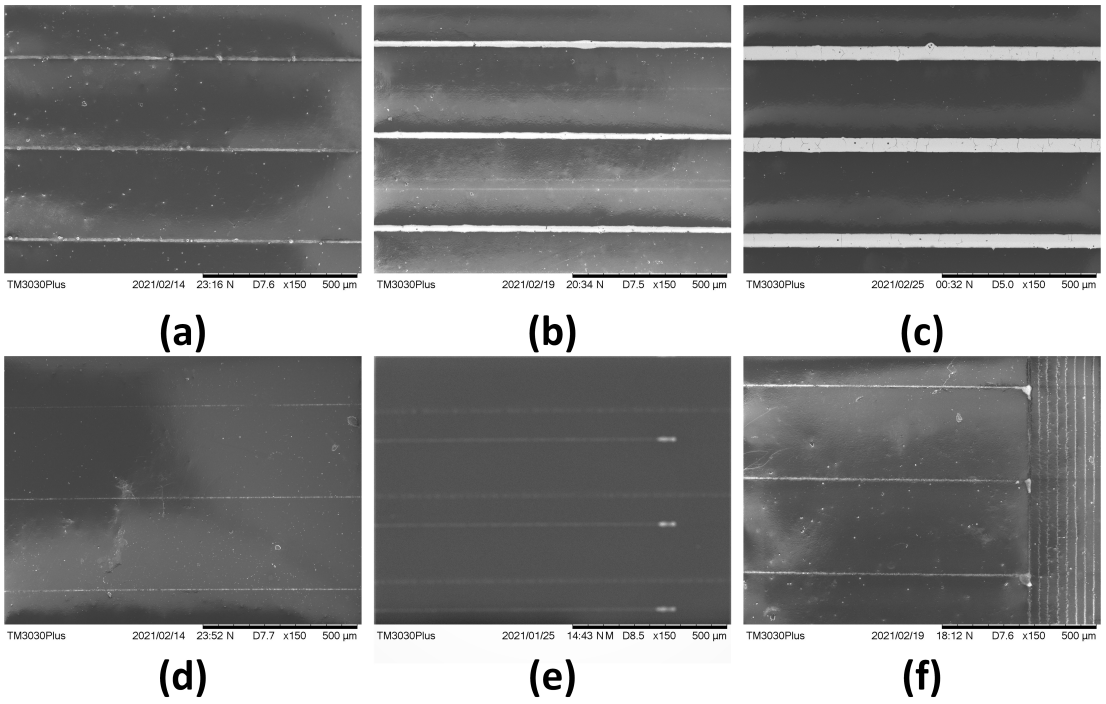

FIGURE 2.12: Scanning electron microscope (SEM) images of printed lines with (a-c) Type C and (d-f) Type D printheads

TABLE 2.6: EHD printed line resolution parameters in the literature

S.No.	Nozzle Diameter (μm)	Nozzle Material	Resolution (μm)	Voltage (kV)	Ratio (Nozzle to Line width)	Ref.
1	7	Glass Nozzle	6.06	0.4	1.16	[78]
2	6	Glass Nozzle	7.25	0.38	1.21	[68]
3	7	Glass Nozzle	5.3	0.4	1.32	[79]
4	20	Glass Nozzle	14.8	0.55	1.35	[80]
5	6	Glass Nozzle	4.4	0.6	1.36	[81]
6	260	Stainless Steel Nozzle	175	3.6	1.49	[82]
7	5	Glass Nozzle	2.8	0.3 0.9	1.79	[66]
8	10	Glass Nozzle	5	0.8 1.5	2.00	[67]
9	30	Glass Nozzle	15	0.45-0.65	2.00	[83]
10	100	Metal Nozzle	48.15	3	2.08	[72]
11	200	Stainless Steel Nozzle	95	1	2.11	[84]
12	110	Metal Nozzle	50	2	2.20	[85]
13	110	Stainless Steel Nozzle	45	1.2	2.44	[86]
14	5	Glass Nozzle	2	0.42	2.50	[65]
15	60	Stainless Steel Nozzle	19	3	3.16	[87]
16	100	Stainless steel Nozzle	20	2.25	5.00	[88]
17	180	Stainless Steel Nozzle	30	0 to 15	6.00	[52]
18	840	Stainless Steel Nozzle	135	8.7	6.22	[89]
19	80	Stainless Steel Nozzle	2.3	0.60	34.78	[70]
20	220	Metal Nozzle	5	1.65	44.00	[73]
21	100	Stainless Steel Nozzle	0.7	0.2-0.6	142.86	[71]
22	500	Copper 3D Printer Nozzle	1.84	0.9	271.74	This work

at the tip. Table 2.6 shows the printed resolution of different EHD systems reported in the literature and the printed resolution of line width in this work.

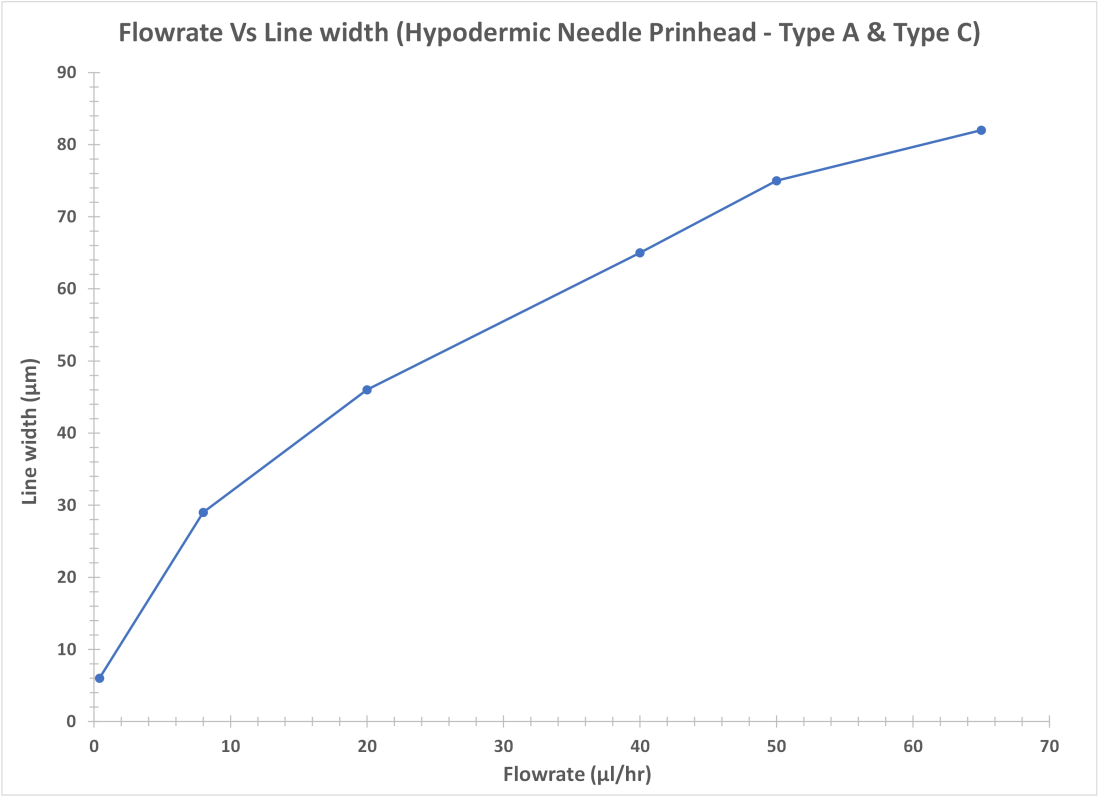

FIGURE 2.13: Flow rate vs line width for hypodermic needle type printheads (Type A and Type C)

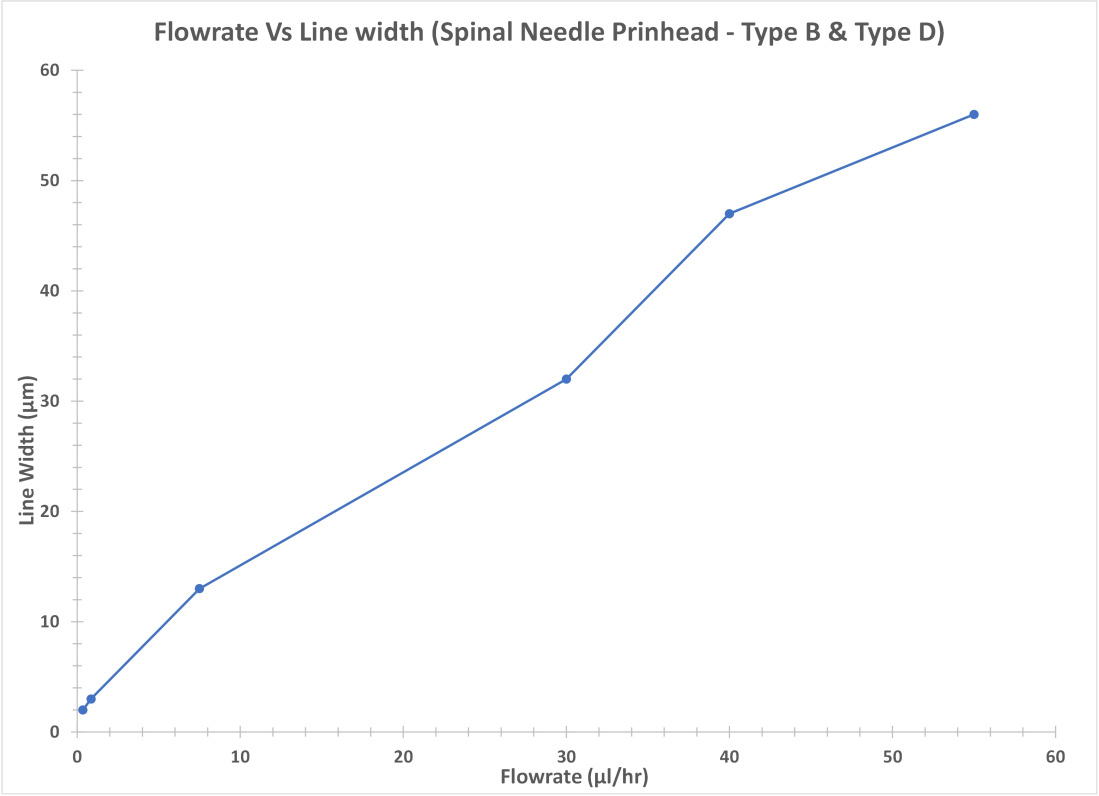

FIGURE 2.14: Flow rate vs line width for spinal needle type printheads (Type B and Type D)

Similarly, when the hypodermic and spinal needle printhead was compared it was found that the spinal needle printhead has small printed features as compared to the hypodermic printhead. This is due to the respective smaller conejet diameter when the fluid exit the printhead nozzle. The reason for the enhanced resolution is due to the momentum of the liquid which is lower for the spinal needle as compared to a hypodermic needle. The momentum is directly proportional to the height of the bevel cut. Due to the higher momentum, the liquid volume ejecting from the nozzle is greater for hypodermic type printhead as compared to the spinal printhead and hence the jet size of conejet becomes smaller for spinal needle printhead which improves the printing resolution. Figures 2.13 and 2.14 illustrate the abovementioned phenomenon by comparing the printed line width with respect to the flowrate of hypodermic and spinal needles printhead respectively.

2.5 Conclusions

In this work, we proposed a method to improve the printing resolution from EHD printing. The work highlights the importance of needle profile rather than the size of the needle to generate the droplet by comparing the printing of silver conductive ink through four different EHD printhead designs. The method also provides the solution of using the bigger size of nozzle to avoid common issues with the already reported EHD system based on glass pulled nozzles. Feature size of as small as 1.85 μm was printed with the proposed geometry of the EHD printhead under the optimal flowrate, a constant standoff distance of 350 μm and optimal applied voltage. The overall experimental optimization of system achieved the nozzle diameter to printed resolution of 270 times which is the highest reported value to the best of our knowledge. The bigger nozzle diameter opens the possibility of printing highly viscous polymer-based inks and the high concentration of nanoparticle inks to be utilized by the proposed printhead design in this work. This can be of great significance in the areas of biomedical, optics, soft robotics and sensor applications which require additive printing of micro and nano size features.

Chapter 3

Laser ablation assisted micropattern screen printed transduction electrodes for sensing application

3.1 Abstract

In this work we present a facile method for the fabrication of several capacitive transduction electrodes for sensing applications. To prepare the electrodes, line widths up to 300 μm were produced on polymethyl methacrylate (PMMA) substrate using a common workshop laser engraving machine. The geometries prepared with the laser ablation process were characterised by optical microscopy for consistency and accuracy. Later, the geometries were coated with functional-polymer porous-cellulose decorated sensing layer for humidity sensing. The resulting sensors were tested at various relative humidity (RH) levels. In general, good sensing response was produced by the sensors with sensitivities ranging from 0.13 to 2.37 pF/%RH. In ambient conditions the response time of 10s was noticed for all the fabricated sensors. Moreover, experimental results show that the sensitivity of the fabricated sensors depends highly on the geometry and by changing the electrode geometry sensitivity increases up to 5 times can be achieved with the same sensing layer. The simplicity of the fabrication process and higher sensitivity resulting from the electrode designs is expected to enable the application of the proposed

electrodes not only in air quality sensors but also in many other areas such as touch or tactile sensors.

3.2 Introduction

Numerous fabrication techniques have been reported in literature to form the transduction schemes for sensors attaining new functionalities, superior device responses and capabilities. However, most of the techniques require intricate processes and costly facilities to fabricate such sensors. For instance, the conventional microelectromechanical (MEMs) photolithography process, which is a top-down approach for fabricating sensing electrodes, requires cleanroom and chemical etching process [90, 91]. The overall process leads to chemical wastage, poses environmental issues [92–94] and customization in the electrode design is often expensive as the product cost relies heavily on the scale and batch size of fabrication. Therefore, contactless printing and contact printing, not requiring the provision of a clean room, have attained interest recently for R&D activities. Contact printing is widely used in the paper industry and print media.

The upside of these printing strategies is their high throughput with accuracies up to 50 μm of printed features. Generally, all the contact printing methods use roll-to-roll technology to imprint the pattern on the substrate [95–97]. However, interconnect registration control, on account of tight tolerances and elastic nature of the substrate at high speed and pressure is intricate in nature. For large volume production the cost of printed features through roll-to-roll technology is cheaper than contact printing method. However, for small production batches or customized imprints, the cost per item is a lot higher than contactless printing. Among contact-less printing inkjet printing has been widely used for printed electronic applications due to their low capital cost and pervasive availability. Moreover, compared to roll-to-roll printing technology the customized patterned printing can be done readily with the ability to print features or ink additively on the previously printed features.

Thermal and piezoelectric inkjet techniques require formulation of ink which needs to be compatible with the printing process. Inks often degrades in the thermal inkjet printing process if it is composed of material susceptible to thermal degradation, moreover high viscosity ink cannot be used with piezoelectric inkjet printers [98, 99]. Screen printing

for a simple lab-based R&D setup seems to be a possible solution for fabricating transduction electrodes at a much cheaper cost compared to above-mentioned fabricating processes. Screen printing requires a stencil. Although the process is simple, the low-cost customization of the transduction electrodes is a big issue and the process involves spreading a large amount of ink on the mesh. To circumvent the aforementioned issues, a simple laser ablation process for screen printing of conductive ink seems to a be simpler route for fabricating transduction electrodes. The laser ablation process from the commercial laser cutting machine not only provide facile implementation of transduction electrodes but also generates less ink waste when compared to the conventional screen printing of ink. In this work printed capacitive structures to sense the electrochemical behaviour of the analyte are formed by laser ablation technique. The advantage of capacitive sensors is that they consume low energy, are less susceptible to radiation, have good sensitivity and provide fast response [100–105].The most well-known design for measuring capacitive response is a parallel plate (PP) electrodes where the electrical terminals are isolated by a dielectric material[106, 107]. For sensing applications and particularly in thin-film capacitive sensors, interdigitated electrodes(IDEs) are perhaps the most broadly utilized mostly due to their simple design, analytical and numerical modelling [108–111].

The basic components of an electrochemical sensor are the sensing layer, transduction electrodes and the substrate. The sensing layer attracts the analyte by undergoing chemiadsorption which generates the electric signal sensed by the readout circuit. The rate of adsorption dictates the response of the sensor where the desorption cycle is attributed to the recovery of the sensing layer. The sensing layer can be a single layer, bilayer or composite layer. A typical sensor layout is presented in Figure 3.1. Transduction electrodes can have different shape or geometries such as indigitated or meander that provide the enhanced signal for capacitive and resistive sensing schemes [112].

Capacitive sensing has been commonly used for humidity sensors with reference capacitors so to mitigate the drift due to thermal interference. However, these devices are complex due to the inclusion of additional components [113, 114]. Other methods such as heating of substrate are also used to shorten or augment the recovery of such sensors [115]. Nevertheless, with proper selection of sensing layers, electrode geometry and suitable substrate a sensitive and highly responsive environmental sensor can be fabricated which operates at room temperature with low or minimal sensor drift and without

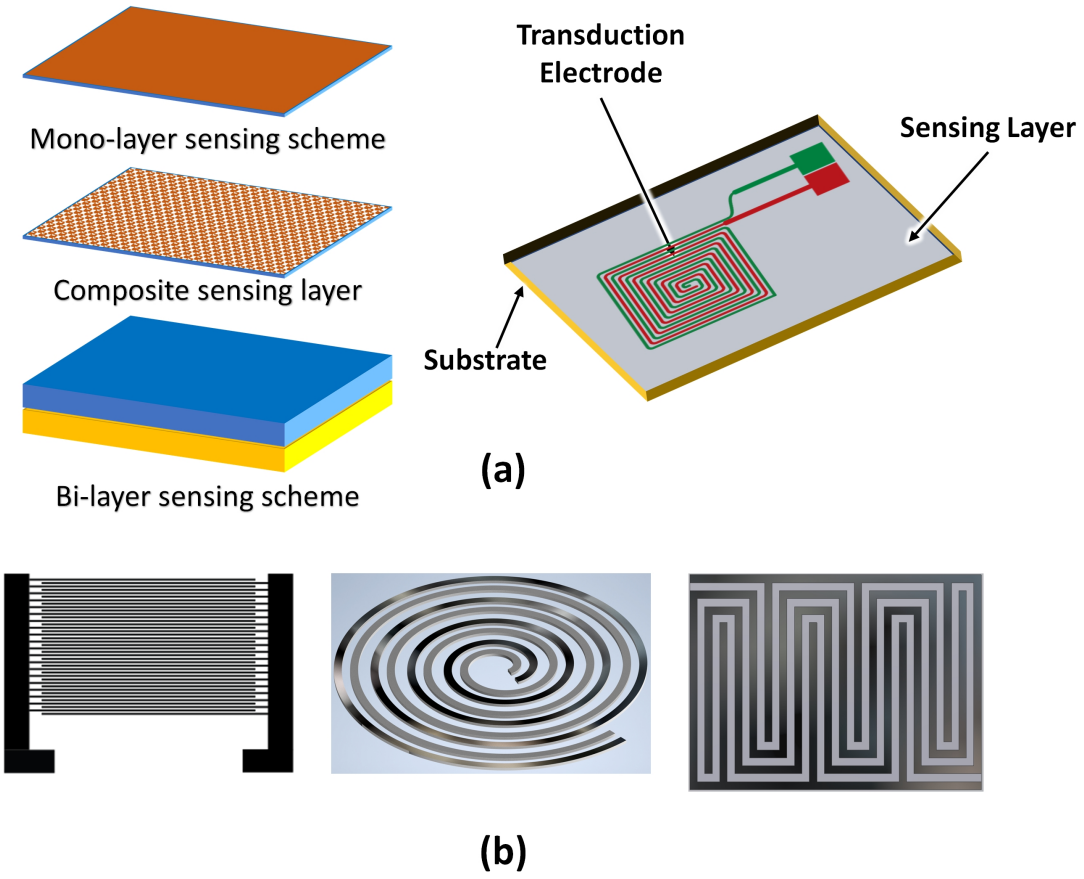

FIGURE 3.1: (a) Typical sensing mechanism. (b) Geometric shapes of transduction electrodes.

needing additional components [116, 117].

Fabricating the transduction schemes on the substrate requires intricate procedure and is often subjected to available resources. In the context of the prevailing COVID-19 pandemic situation most of the fabrication facilities are either non-accessible or closed [118]. In this scenario sensor fabrication techniques based on MEMs [119–121], inkjet printing [122–124] and contact printing [125–127] methods can be expensive or unapproachable. However, a simple laser ablation technique by utilizing the desktop CO_2 laser cutter can be used to fabricate the transduction schemes for realizing the environmental sensor through screen printing the conductive ink inside the ablated tracks.

3.3 Result and Discussion

A systematic methodology followed by pursuing the steps highlighted in Figure 3.2, resulted in the fabrication of laser ablated micropatterned features having an average

width resolution of around 290 μm. Table 3.1 shows the variation in the experimental data of the patterned features.

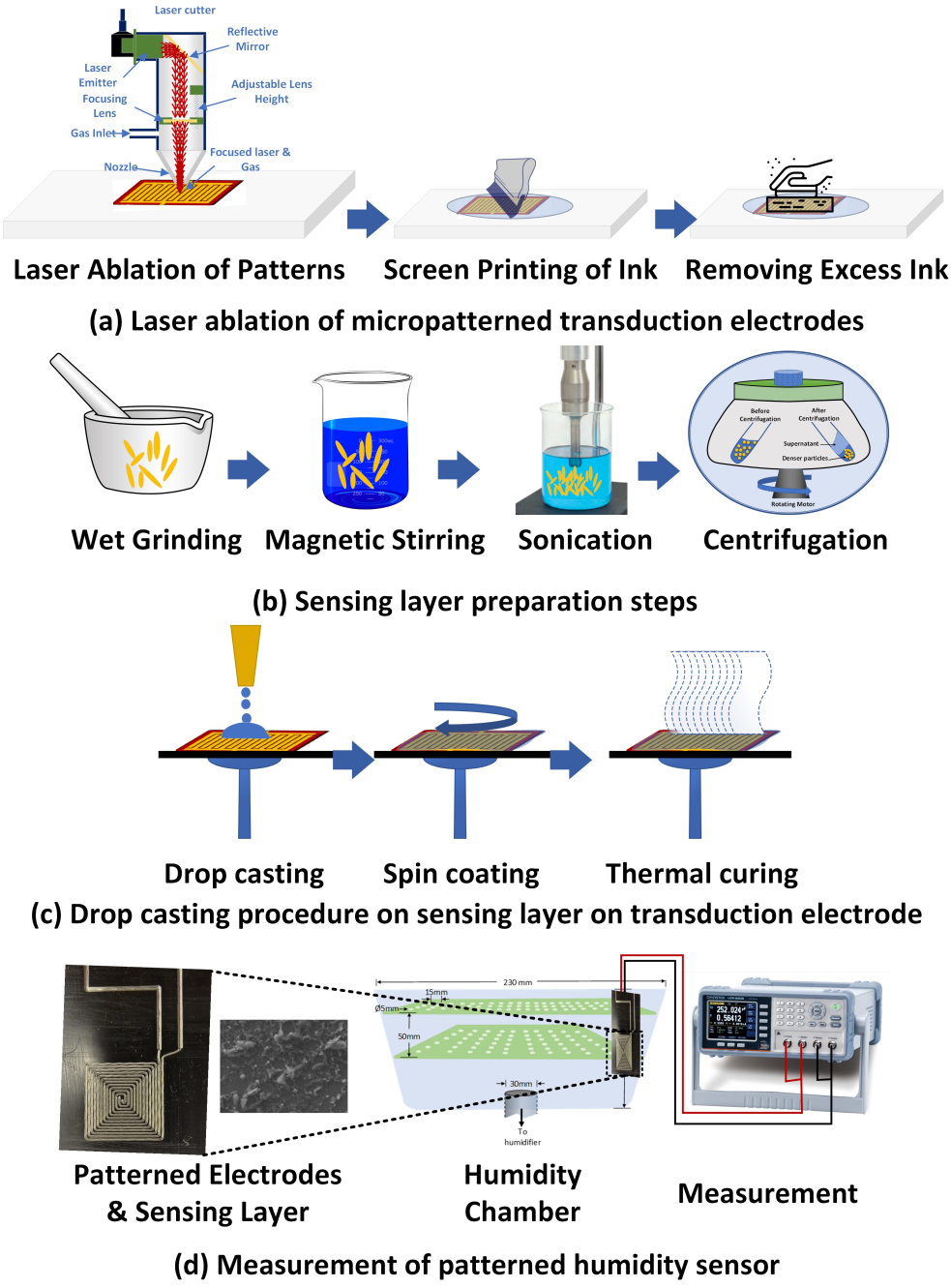

FIGURE 3.2: Step for laser ablated micro-patterned sensor.

The microchannel is formed by the laser ablation process due to the absorption of energy induced by the laser beam. When the laser beam interacts with the work piece it ablates the top surface of the work piece. The rate of ablation depends upon the power, speed of the laser, wavelength of the radiation and material physical and optical properties. The resolution of the microchannel can be optimized by carefully selecting the parameters

TABLE 3.1: Experimental resolution of screen templating through laser cutting process

Straight Profiles Electrode Distance	
Measure	**Value (µm)**
Average	289
Minimum	287
Maximum	292
Standard deviation	2.1
Curved Profiles Electrode Distance	
Average	377
Minimum	370
Maximum	383
Standard deviation	5.3
Straight Profile Interelectrode Spacing	
Average	315
Minimum	313
Maximum	318
Standard deviation	2.1
Curved Profile Interelectrode Spacing	
Average	216
Minimum	208
Maximum	223
Standard deviation	6.1

mentioned above. However, we have used the default ablation process parameters for ease of micropatterning and simplicity of fabricating micropattern which can be utilized for sensing of humidity. In our experiments we used 100% laser power and 100% speed for laser engraving on Poly (methyl methacrylate) 3 mm sheet. Figure 3.3 shows that for curved regions the resolution of patterned microchannel was degraded. The reason for degradation of the resolution is due to slower speed of laser as compared to the straight feature. The X-Y stage of the laser scanning head uses successive straight line interpolation and offsets to interpolate the next laser spot for a curved geometry on the work piece. Due to this interpolation of points for a curved region the speed is slow and more area is ablated due to the prolonged laser exposure at a particular position in time. Optical Images of the curved and straight features depicting the differences in the line widths are shown in Figure 3.3.

Operations that were conducted to reduce the size of the suspended particles and to increase the activation sites can be seen from the scanning electron microscopy images in Figure 3.4. The image shows the overall distribution of the cellulose after wet grinding, centrifugation and ultrasonic sonication.

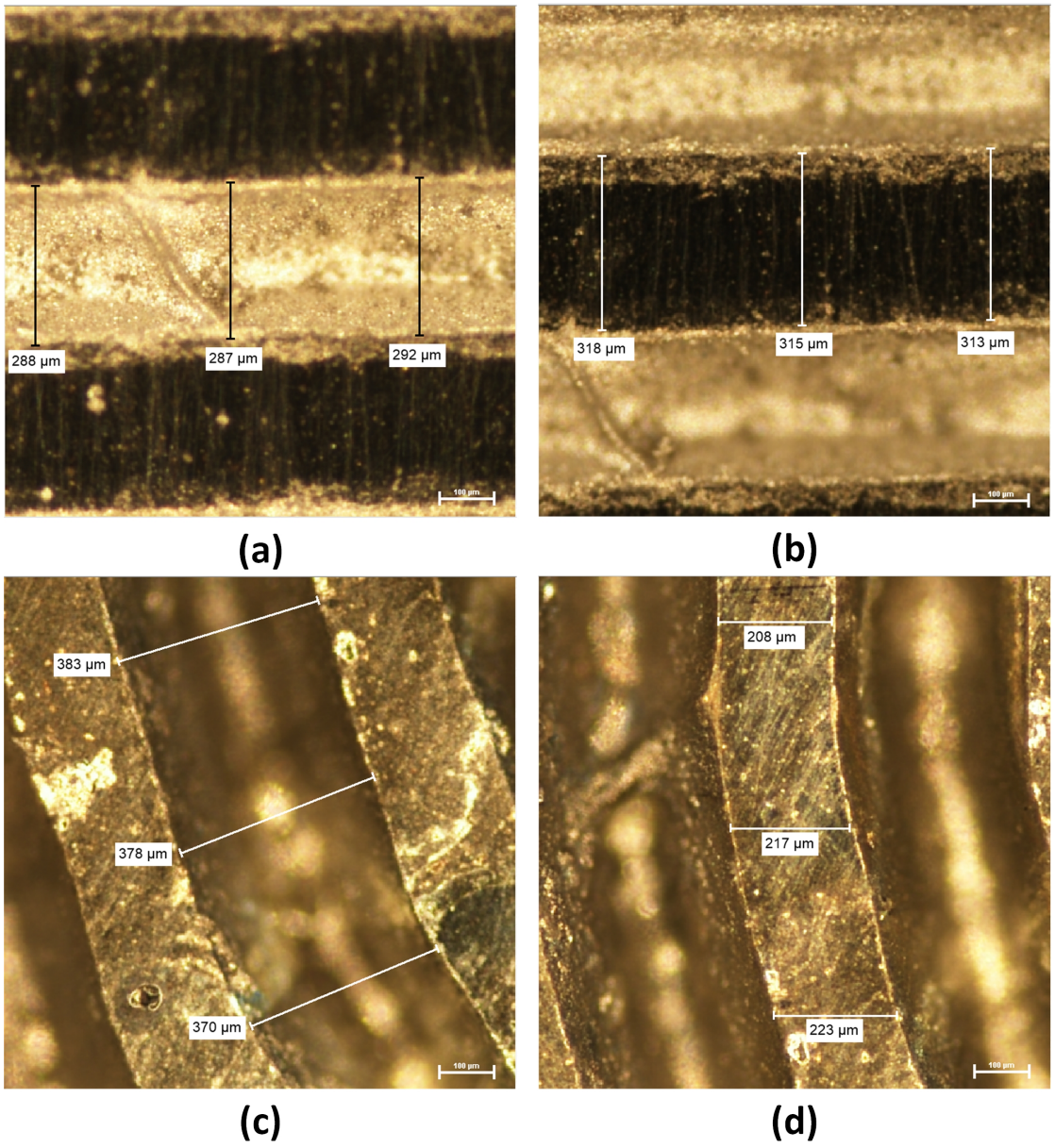

FIGURE 3.3: Optical images of laser ablated transduction features (a) Straight profile (b) Straight profile electrode inter-spacing (c) Curve profile (d) Curved profile electrode inter-spacing.

The composition of ink is based on biodegradable sensing layer, which is mainly composed of cellulose, Poly ethylene dioxythiophene: poly-styrene sulfonate (PEDOT:PSS) [128, 129] and Polyvinylpyrrolidone (PVP) coated silver nanoparticles [130, 131]. Silver nanoparticles (SNP) are known for their antimicrobial activities as in medical applications silver catheters and silver coated catheters are used for slow-injection of solvent while providing antiseptic properties. Moreover, as the nano-particles are coated with PVP, there are less chances of toxicity and the possibility of oxidation [132–134]. On

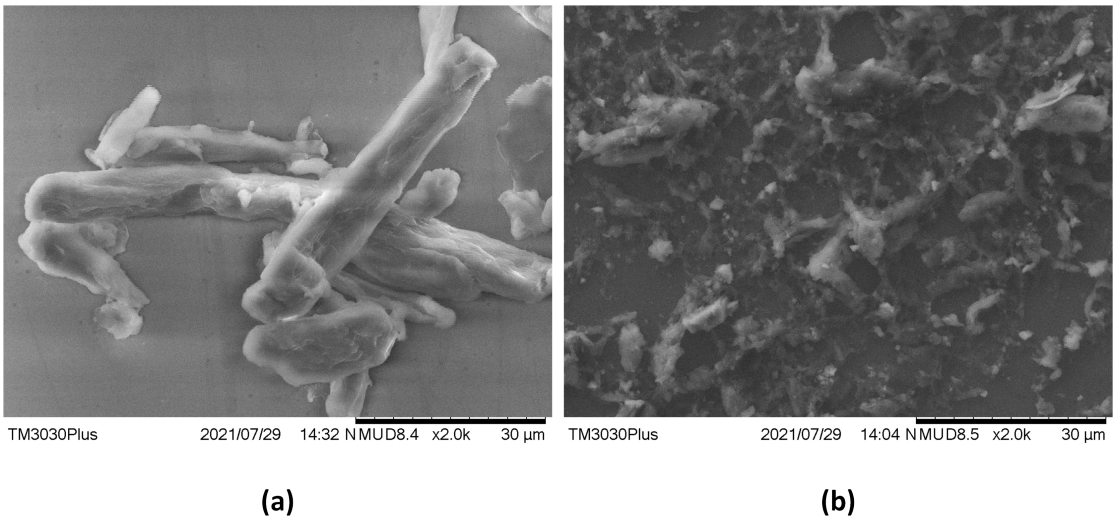

FIGURE 3.4: SEM images of cellulose decorated sensing layer. (a) Decorated cellulose before ultrasonication. (b) Decorated cellulose after ultrasonication.

the other hand, cellulose is a good natural insulator commonly used as a dielectric material. It has been incorporated into many applications as substrate for conductive and non-conductive applications [135, 136].

The sensing properties depend on the change in electrical properties of the sensing layer, which forms a uniform sensing region over the transduction electrodes. Once the sensing layer is exposed to humidity the porous structure of the cellulose decorated PEDOT:PSS and PVP coated SNP layer changes it's capacitance during the adsorption and desorption cycles. The change in capacitance is then recorded for various humidity levels. All the sensors were tested with a starting relative humidity level of 50% as it was the prevailing ambient condition for conducting the humidity measurements. The measurements were taken with the help of GW INSTEK LCR-6000 Precision LCR Meter by sweeping the selectable frequencies between 100 Hz to 2 kHz as tabulated in Table 3.2. The formulation of the sensing layer with the addition of PVP coated SNP has provided steric stability. The steric stability is evident in the SEM image as the cellulose fibres are well spread over the region. Not only the readings are stable but also the fluctuation of the capacitance value of the prepared sensors remains with in standard deviation of 0.52 pF. In our experiments, when only the conductive PEDOT:PSS and cellulose mixture was spin-coated on the transduction electrodes, the capacitive reading from the fabricated sensors were not stable due to highly conductive PEDOT:PSS coated layer. The mixing procedure and addition of PVP coated SNP not only reduced the conductivity of the sensing layer but also provided anti-agglomeration property to the

prepared ink for sensing. We noted that, on average, for all the transduction geometries the fluctuation in the capacitance was abrupt without the inclusion of PVP coated SNP steric stabilizer.

TABLE 3.2: Experimental resolution of screen templating through laser cutting process

The capacitance of transduction geometries at 50% RH							
S.No.	**Freq.**	**IDTs**	**Meander**	**Spiral**	**Swiss**	**Serpentine**	**Custom**
1	100	15.87	19.43	17.30	19.65	21.23	23.10
2	200	15.52	19.09	16.88	19.21	20.84	22.75
3	300	15.28	18.95	16.71	18.90	20.58	22.48
4	400	15.24	18.63	16.70	18.77	20.43	22.34
5	500	15.14	18.66	16.56	18.60	20.32	22.32
6	750	15.14	18.42	16.39	18.22	20.31	22.39
7	1,000	14.88	18.33	16.35	18.28	19.94	21.99
8	1,250	14.73	18.18	16.36	18.14	19.80	21.73
9	1,500	14.76	18.25	16.23	18.13	19.75	21.83
10	2,000	14.68	18.16	16.16	18.00	19.60	21.75
Mean		15.12	18.61	16.56	18.59	20.28	22.27
Std. Deviation		0.36	0.41	0.33	0.51	0.49	0.43
Schematic		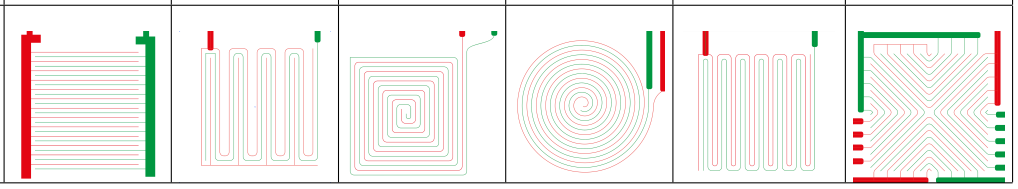					

The results of the humidity response with the transduction geometries are highlighted in Fig 3.5. The highest response was recorded with a meander electrode configuration having a sensitivity of 2.37 pF/%RH whereas the lowest response was from archenemies spiral configuration of 0.13 pF/%RH. At relative humidity level above 80% there was a sharp increase in capacitive response for meander electrode configuration as compared to the other geometric configuration. Serpentine, interdigital, and custom pattern has not only shown good sensitivity but a gradual increase in capacitive response with respect to relative humidity. Therefore, these configurations may be selected for practical ranges of humidity response. The reason for the variation in the transduction response is due to the difference in the density of the sensing electrodes and inflection points in the geometries. These changes result in the difference of electric field generated by the respective geometries thus exhibiting changes in the capacitance of each geometry.

The sensitivity of the sensor is defined as the ratio of difference of the capacitance at a specific relative humidity level designated by C_{RH} and base capacitance (C_{RHo}) of

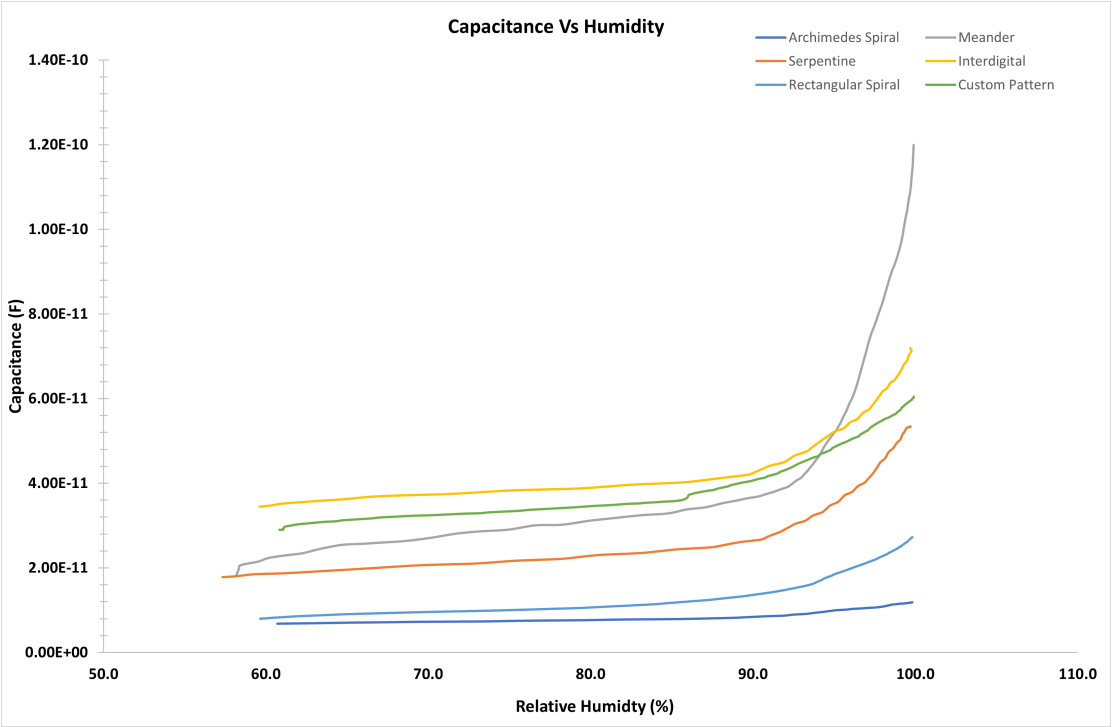

FIGURE 3.5: Humidity response of patterned sensors (a) Archemedies Spiral (b) Meander (c) Serpentine (d) Interdigital (e) Rectangular Spiral (f) Custom design .

the sensor divided by the base capacitance of the sensor. Equation 3.1 mathematically denotes the sensitivity of the sensor.

$$S = (C_{\mathrm{RH}} - C_{\mathrm{RHo}})/C_{\mathrm{RHo}} \tag{3.1}$$

Table 3.3 shows the sensitivities of the different transduction schemes. It is evident from the sensitivity values that sensing gradient highly depends on the transduction geometry. For certain sensing application a same sensing layer can offer better result with a specific geometry.

TABLE 3.3: Sensitivity of the transduction geometries

Sensitivity of fabricated sensors	
Transduction Geometry	**Sensitivity pF/%RH**
Meander	2.37
Archimedes Spiral	0.13
Serpentine	0.84
Interdigital	1.06
Rectangular Spiral	0.31
Custom	0.88

Table 3.4 and Figure 3.7 show the response and recovery cycles of all the patterned sensors. For each cycle of response time and recovery time of the sensor are calculated. The response time is highlighted in green, and the recovery time is in red. Except the meander geometry all the other fabricated sensors have response time of less than 1 second, illustrating a quick humidity sensing application. However, the overall recovery times were below 6 seconds for all the geometries. A closer inspection of the bin sensitivities of all the transduction electrodes, as shown in Figure 3.6, indicates that the meander transduction electrode geometry has exceptionally high sensitivity in the humidity bin of 90-100% when compared with the other transduction electrodes. Due to this effect the overall sensitivity of the meander geometry is higher as compared to the other geometries. Considering this factor and the gradual increase of transduction response of interdigital, serpentine, rectangular and custom geometries, it is evident that they are well suited for humidity sensing in our case.

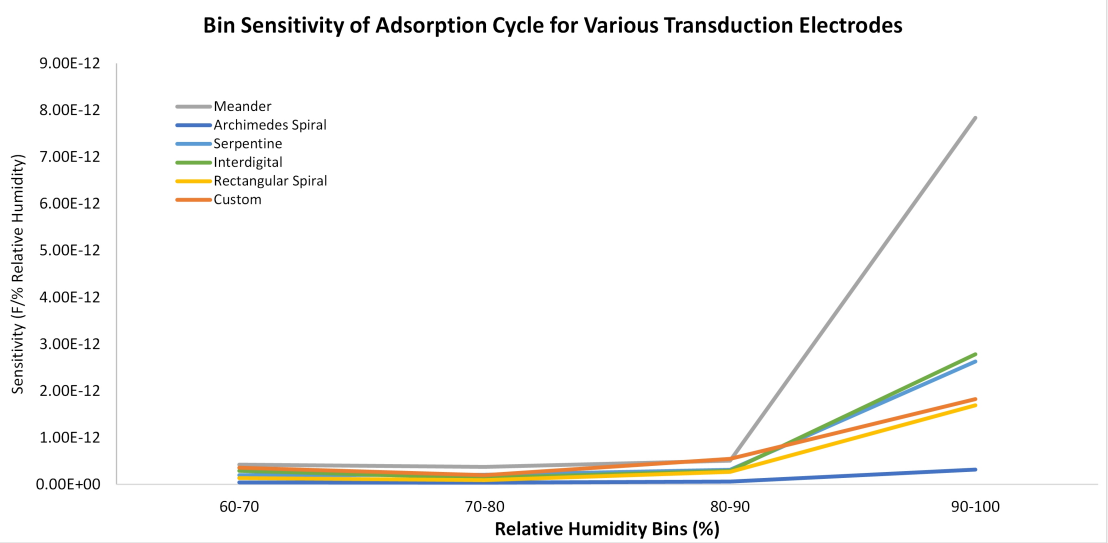

FIGURE 3.6: Bin sensitivities of all the transduction electrodes.

TABLE 3.4: Response and recovery of the transduction geometries

Response and recovery of fabricated sensors		
Transduction Geometry	**Response (s)**	**Recovery (s)**
Meander	9.38	5.90
Archimedes Spiral	0.57	5.10
Serpentine	0.38	3.13
Interdigital	0.91	4.74
Rectangular Spiral	0.57	1.28
Custom	0.54	3.11

Figure 3.8 provides the adsorption and desorption cycle of patterned sensors. We found

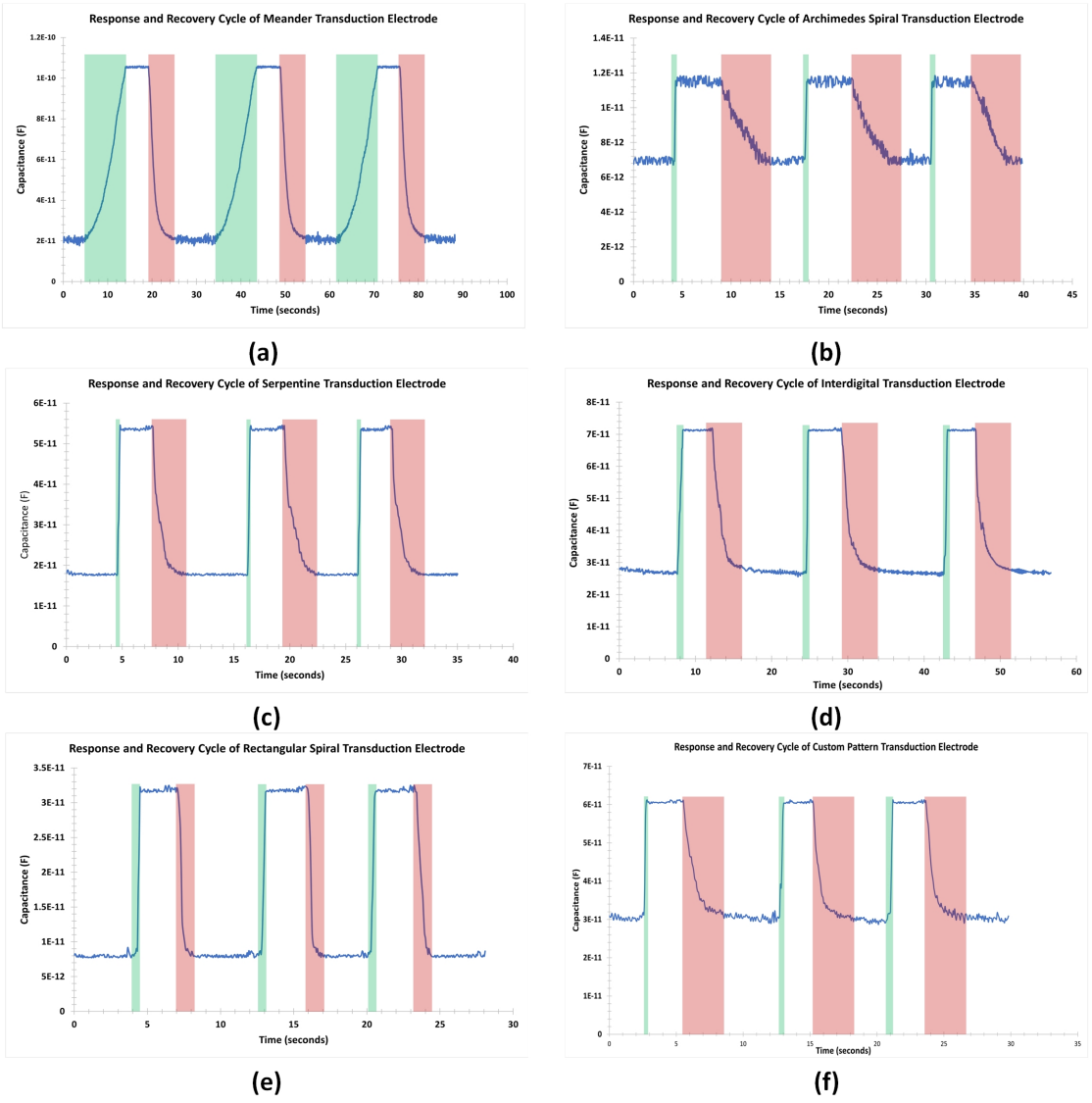

FIGURE 3.7: Response and Recovery cycle of patterned sensors (a) Meander (b) Archimedes Spiral (c) Serpentine (d) Interdigital (e) Rectangular Spiral (f) Custom design .

that there exists a hysteresis between the adsorption and desorption cycle of the patterned electrodes in all the geometry. However, for certain geometry there the hysteresis is small compared to other geometries. The reason for the hysteresis is due to two factors. The first is due to the porous nature of cellulose layers on the sensing layer which traps the water molecules during the desorption cycle. It is evident that the capacitive response for the desorption is more than the adsorption cycle of depicting the high chances of trapping water molecules.

The other reason is the gradual decrease of humidity level in the desorption cycle as compared to the adsorption cycle which has a steep change in the humidity level. Since,

the response of the DHT22 sensor has a higher rise due to the sudden increase of humidity in the chamber therefore, there is more hysteresis in the response stage of the sensor as compared to the recovery stage, where the hysteresis is low since the chamber humidity during this stage has a slower rate. It is anticipated that a precise measurement chamber can reduce the hysteresis between the response and recovery stage of the screen-printed sensors. It can be noted that in most of the cases the chamber starting humidity was a little higher at the end of the reading and the screen-printed response was also a little higher in the end depicting that there exists high correlation of humidity sensing of the sensors even with the slight deviation of humidity levels.

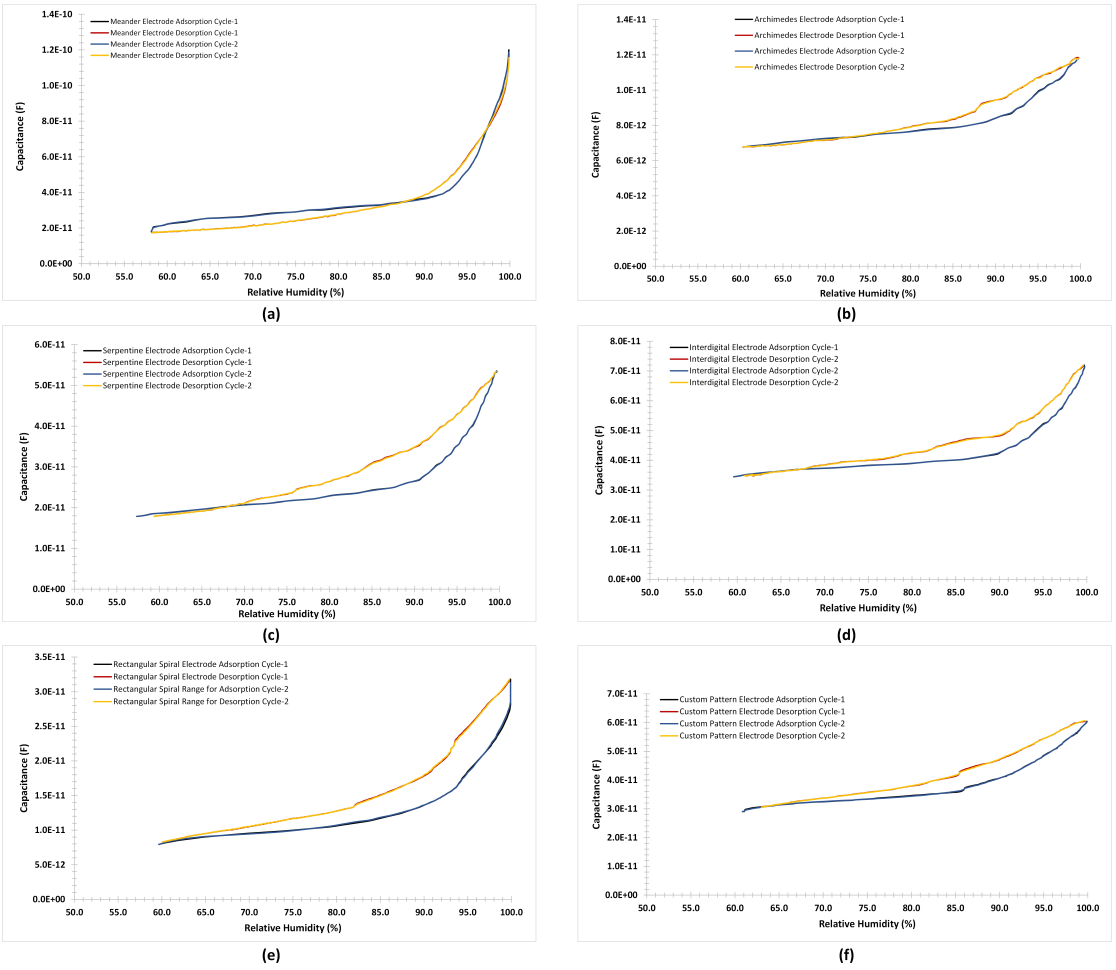

FIGURE 3.8: Adsorption and desorption cycle of patterned sensors (a) Meander (b) Archimedes Spiral (c) Serpentine (d) Interdigital (e) Rectangular Spiral (f) Custom design .

In the preceding discussion the results of the sensitivity, hysteresis, response and recovery of various transduction scheme was presented for humidity sensing. It is pertinent to note here that the sensitivity of the meander electrode was higher among all the

fabricated sensors however, the response and recovery cycle was the lowest among all the geometries. Moreover, there was an appreciable increase in the capacitance value above 80% relative humidity which indicates highly non-linear relationship between the humidity and respective capacitive response. In this regard, the most promising electrode configuration seems to be either serpentine and custom pattern as these were the only geometries which provided a good sensitivities and less non-linearity among all the fabricated geometry.

3.4 Methods

3.4.1 Fabrication of Transduction Electrodes

Laser scribing is a method to induce high laser power to produce features or cuts on the surface of the substrate. In a mechanical workshop, the laser machine is used for cutting various materials of different thickness to perform 2D cutting and engraving. The main purpose is to transform the digital design to follow a laser path which can be used for either cutting or engraving purposes. The depth of the cut depends upon the settings of power of the laser, speed of the laser and whether the spot size of the laser is focused on the substrate. On the other hand, the width of the cut depends upon the focusing lens, laser spot speed, power of the laser and distance of the laser with the object. If the laser is adjusted so as to focus properly on the substate then the quality of the laser cut is precise and is slightly above the focused spot size of the laser. The power of the laser is converted into heat energy when focused on the substrate and removes the material by locally ablate or burn the material to induce the digital imprints on the substrate. In the laser cutting process, the cut width is often termed as the kerf width of the laser cutting process. In order to reap the benefits of the above-mentioned process, we followed a facile process of engraving the designed pattern on the Poly (methyl methacrylate) (PMMA) sheets of thickness 3 mm. The printing process involves the computer-aided (CAD) designs of the electrode geometry and digitally transforming those through CO_2 laser cutting beam on the PMMA sheets. Figure 3.9 highlights the overall process of fabrication.

The laser ablation was done by considering the glass transition temperature of the polymer substrate, laser speed, laser power and z-height of the laser beam without the

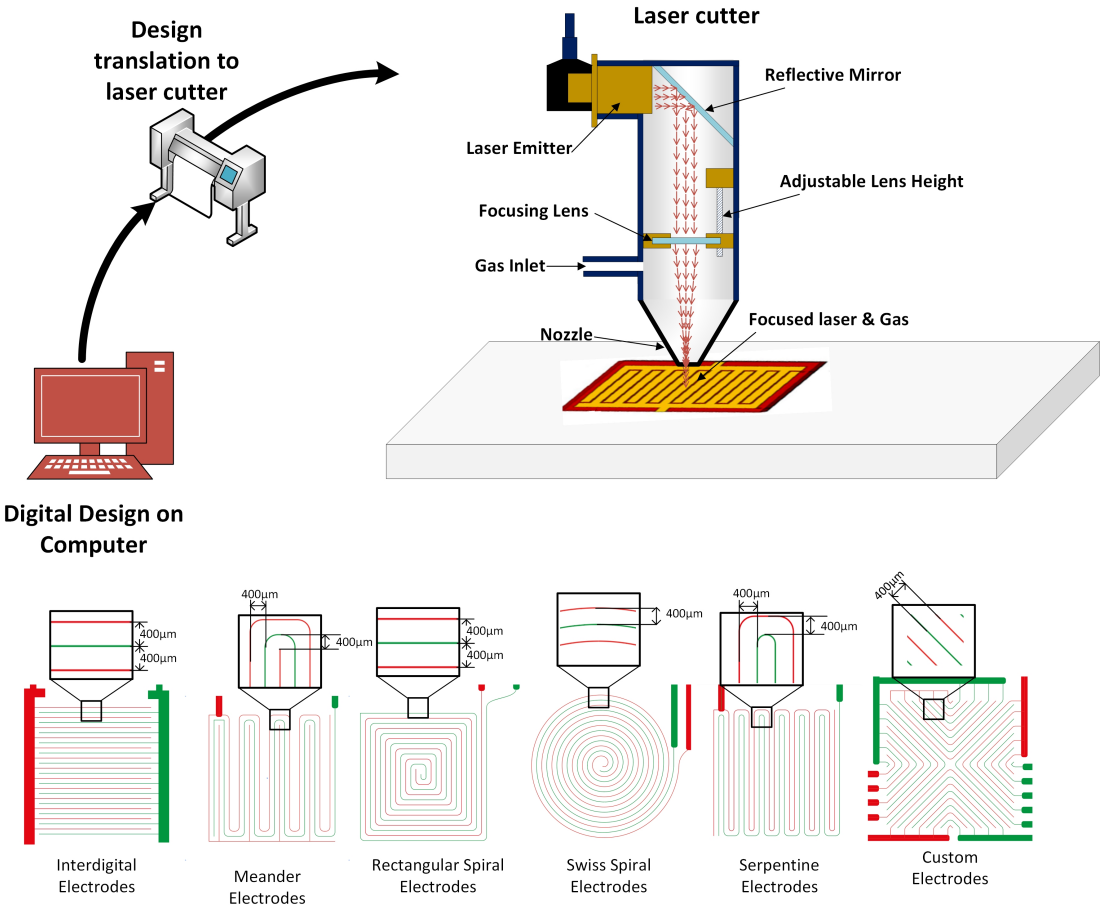

FIGURE 3.9: Transduction electrode fabrication process and transduction geometries.

optimization of the kerf width. This technique provides a rapid production of custom geometrical transduction scheme on the substrate. Due to the nature of the process, it requires no special micro fabrication process and can be done in a workshop environment to produce the transduction electrodes. Moreover, as the polymer becomes flexible close to its glass transition temperature, there is a possibility to adhere the substrate to curved surfaces. Moreover, the geometrical designs can be readily exported to the laser cutter, where the laser can be turned on and off instantly and the engraving/cutting features can be set for various layers. However, the limitation of the above technique is the resolution of the laser beam and the accuracy of stages of the CO_2 beam laser cutter. In our experiments we used six different geometrical features all with line spacing of 400 μm from the centre of the finger. Once the geometrical features were engraved on the PMMA sheets the edges of the sheets were cut out and a template for screen printing of conductive ink is ready for the next stage of conductive ink coating process. In our experiments we used the Novacentric Metalon® HPS-021LV (Novacentric, USA) screen

printing ink. HPS-021LV is an electrically conductive silver flake ink designed to produce conductive traces on the substrate substrates such as paper, PET, glass, polyimide, and silicon. Properties of HPS-021LV ink is enlisted in Table 3.5

TABLE 3.5: Properties of HPS-021LV screen printing ink

Measure	**Value**
Average particle size	2-4 μm
Viscosity	26,000 cP at 0.1 sec^{-1}
Specific gravity	3.1
Silver loading	75%
Solvent	Water

Once an ample amount of HPS-021LV is coated on the PMMA substrate the ink settles insides the engraved geometrical features. Later these geometrical features is subjected to heating in a convective oven to evaporate the solvent at 100°C which is below the glass transition temperature of the PMMA sheet of 105°C. The thermal curing of the ink was done for 1 hour each for all the geometrical features. After the curing process the sheet is cooled down to the ambient temperature and the excess ink is removed by uniformly scribing the surface of the PMMA sheets using a scribing knife. As the engrave features were below the level of the PMMA sheets, therefore, after the scribing process only the ink necessary for forming the transduction electrode was left behind resulting in the functional sensing schemes. After the scribing process the conductivity of the tracks were checked through continuity measurement via a multimeter. Since, for each type of geometrical design the track lengths were different from the connection pad therefore, the conductivity of the tracks varied for each geometrical feature.

3.4.2 Sensing Layer Preparation

The process of ink preparation involves a synthesis of ultrafine particles from an amorphous precursor. For this purpose, a comprehensive methodology has been devised. The methodology involves the following steps as shown in Figure 3.10.

The process starts with the wet grinding of 1 gm of Sigmacell Cellulose (Product Code: S3504) of Type 20 with 20 μm average diameter size with 5 ml of deionized water. The wet process improves the overall particle size by reducing the lumps and agglomerations during the storage of the cellulose. Shearing forces reduce the particles' size, thus increasing the particles per unit weight. Reduction in particles increases the activation

sites. During the 2-hour grinding process the reduction in particle size in the mortar is felt with a decrease in friction of the grinding. Wet grinding was assisted by gradually adding water to maintain the solvent quantity during the process.

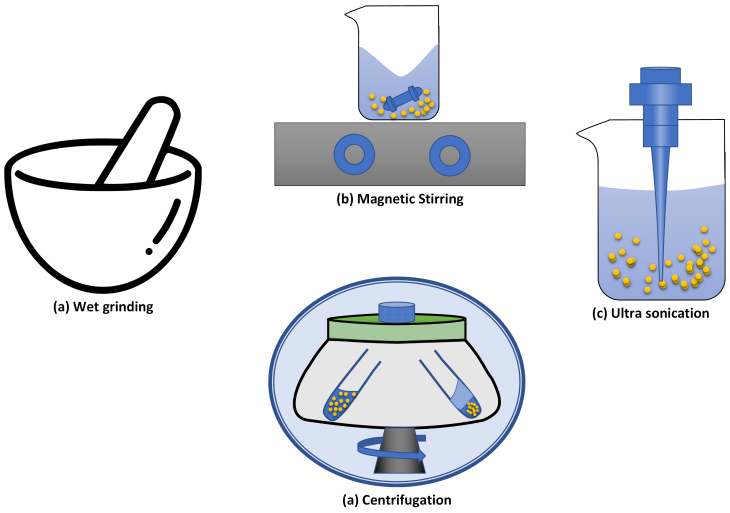

FIGURE 3.10: Process of ink preparation.

Later the mixture was transferred into the beaker and is weighted to record the concentration of solvent in the mixture, Once the weight measurement is taken, 50 ml of deionized water was added so facilitate the stirring process through a magnetic stirrer. Magnetic stirring of mixture provided a uniform homogenization of amorphous solid particles in the solvent. Thus, improving the uniformity of the suspended particles in the solution. After the stirring process the mixture is heated to 100 °C attain the solvent quantity of 5 ml after the evaporation process. A 1 ml of high conductivity grade of Poly(3,4-ethylenedioxythiophene)-poly(styrenesulfonate) (PEDOT:PSS) purchased from Sigma Aldrich (Product Code : 900181) having concentration of 0.5-1wt%of PEDOT:PSS in water along with 0.1 ml of Polyvinylpyrrolidone (PVP) coated silver nanoparticle of concentration 5mg/ml in water (PVP-coated AgNP) purchased from NanoComposix was added to adjust the conductivity and to provide steric stability of the mixture was added thus avoiding agglomeration of the suspended particles. The mixture was then probe sonicated twice for an interval of 5 minutes each to attain the homogenized mixture of cellulose decorated conductive polymer. After sonication the liquid is then subjected to centrifugation at 800 rpm for 30 minutes to remove the heavier particles from the mixture by removing the supernatant from the solution. The mentioned process provided a uniform concentration of cellulose particles when compared to the filtration process. Since, in the filtration process only particles

above a certain size are removed from the liquid. The shape of the particle remains the same, whereas the above method shapes the particles into flakes or nanorods. This two-dimensional feature is more responsive when used for gas sensing applications [137]. Once the mixture is prepared the solution was poured on the transduction electrode and each transduction acrylic plate was then spin-coated at 1000 rpm for 120 seconds for each type of transduction geometry.

3.4.3 Measurement Setup

Transduction electrodes are commonly used in sensing applications. The electrodes provide the ability to measure different kinds of gases such as Nitrous oxide, gaseous Ammonia, humidity, and many more [138]. To test the performance of various patterns of electrodes, we chose to work with the most frequently measured physical quantity i.e., humidity. This provided us with a base for assessing performance parameters of various patterns of electrodes, built using in-house facilities. Since, the humidity level in an indoor setting is quite low and stable, we carried out the experiment in an environment where humidity could be controlled to monitor the behaviour of the electrodes. Therefore, an environment was built in a plastic container that was linked to an external humidifier where the level of humidity was varied and continuously monitored. Basic structure of the experimental setup is depicted by Figure 3.11.

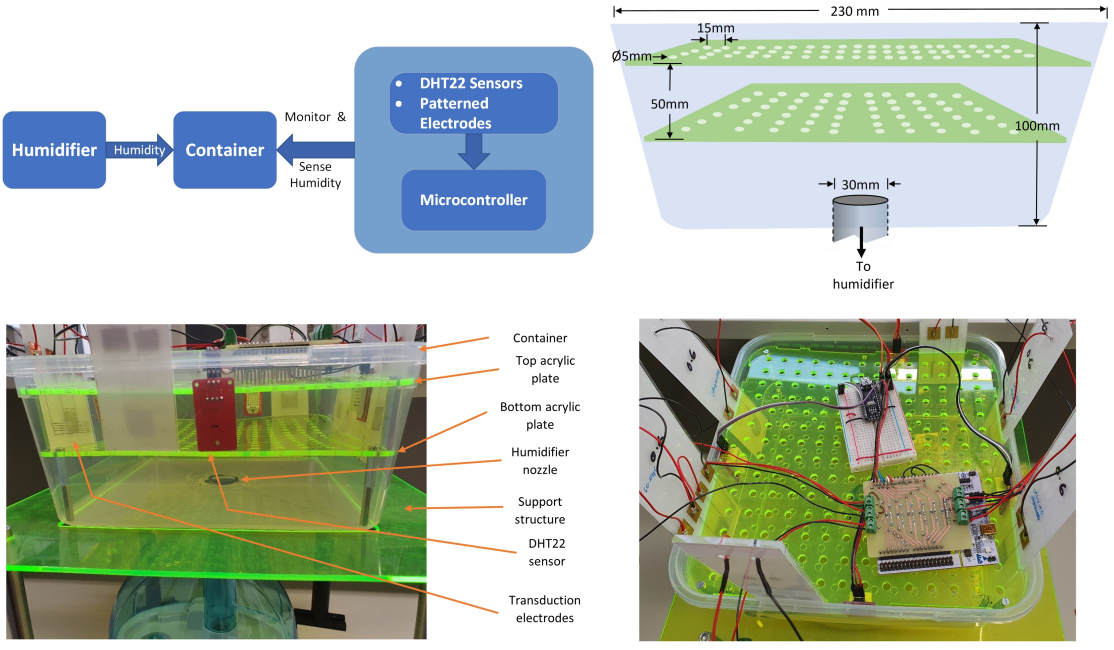

FIGURE 3.11: The basic layout of the experimental setup.

The container was built such that the DHT sensors and different patterns of electrodes could be placed inside it. To achieve homogeneity of humidity inside the container, two acrylic plates were placed horizontally inside the container with holes made using a laser cutter. The holes of 5mm in diameter were spread evenly across both plates with 15mm spacing between them, and a 7mm offset in holes between the top and bottom plate. The bottom plate assisted in dispersing humidity evenly while the top plate assisted in releasing excess humidity out of the chamber. Four DHT22 humidity sensors were placed on all four sides of the container such that the sensors and the electrode sensors were placed vertically around the inner walls of the container located between the top and the bottom plates. This enabled us to simultaneously test the performance of all the different patterns of transduction electrode sensors with varying levels of humidity. The two plates with holes fit inside the container with a much larger hole cut out at the centre of the container for a plastic pipe that drops down to the humidifier.

Humidity can easily be generated using an appliance called the humidifier, which is inexpensive and provides the user with the ability to control the humidity. It is an ultrasonic cool mist generator that is droplet free from Kogan and has a 1.5-liter water tank. The humidifier was placed at the bottom of the container with a circular hole cut out at the bottom for a tight fit of a 30mm wide pipe connecting to the outlet of the humidifier. A support structure was built to place the container on top of the humidifier. The humidifier exudes mist from the top into the bottom of the container through a pipe. Each pattern of transduction sensor has two square pads filled with silver ink that extends to the sensing electrodes themselves. With the help of adhesive copper tape, small pieces were fixed to the two pads, so that thin multistrand wires could be soldered on to the tape for connectivity. Arduino/STM32: As soon as the humidifier starts introducing humidity into the container, DHT22 sensors begin reading humidity levels and simultaneously the transduction electrodes start sensing the humidity levels. Humidity levels from DHT22 sensors, were read using Arduino Nano that was kept separate from the capacitive readings taken with Nucleo-F446RE board. Components of the experimental setup are labelled in Figure 3.11.

The top view of experimental setup indicating position of transduction electrodes of six different patterns (meander, interdigital, serpentine, circular spiral, rectangular spiral and a custom design) and four DHT22 humidity sensors, all mounted on inner walls of the container.

3.5 Conclusion

In this work, we presented a comparison among six different electrode layouts fabricated by using a laser ablation process. It has been observed that depending on the specific application and its requirements, an appropriate transduction scheme for environmental humidity sensors can be ascertained. For a large area sensing applications, the presented designs are scalable and suitable for sensing applications. The custom triangular pattern presented in this work can be a promising scheme when scalability for large area is not an issue. The fabricated sensors were tested at various relative humidity levels that achieved a good sensing response with sensitivities ranging from 0.13 to 2.37 pF/%RH in general for various transduction schemes. The meander geometric transduction scheme reported the highest sensitivity among the fabricated sensors however, there were some demerits for such geometry such as lower response and recovery time along with associated non-linearity of capacitive response with respect to humidity. The work presented here provides a facile approach, biocompatible sensing layer and compendium of processes for fabricating sensors in a small low-cost laboratory which can be of great advantage during the prevailing COVID-19 pandemic. Furthermore, the results obtained from the presented fabrication scheme can be extended for a high-resolution patterning electrode geometry with a suitable sensing layer.

Chapter 4

Silver nanoparticle and diethylene glycol monobutyl ether modified conductive ink for high conductivity electrohydrodynamic printing

4.1 Abstract

Piezoelectric inkjet printing is a well-known technique for conductive printing on various substrates. However, the printed conductive tracks require post printing thermal curing. The development of cracks in the printed tracks during the curing process is a common issue associated with the non-optimal ink composition or the substrate expansion during the curing process. This problem can be further aggravated if the ink normally prepared for a particular printer is used with another printer such as an electrohydrodynamic (EHD) printer. Regardless of the reason, if cracks are developed in the printed conductive tracks, the electrical continuity of the printed features is deteriorated, and this can render the overall process ineffective for flexible printed electronics. As a general principle, with appropriate modification of the ink, it is possible to prevent the development of cracks during the curing process. In this paper, we present results of EHD printing experiments over polyethylene terephthalate (PET) substrate with a commercially off-the-shelf (COTs) available ink procured from Novacentrix. The ink is

normally used in piezoelectric inkjet printers. The ink was printed as obtained on an EHD system, but cracks were produced after thermal curing even at temperature below the glass transition temperature of the PET substrate. The ink was later modified with different concentrations of loading of metallic silver conductive nanoparticles and, low concentration of diethylene glycol monobutyl ether. This modification led to elimination/reduction of the cracks as experienced with the COTs ink. A thorough set of characterisations was performed to ascertain the effectiveness of the ink modification and crack-free printed patterns. It is concluded that the printed features with the lab prepared/modified ink produce conductive tracks and the proposed modification plan can be a cost-effective method for modifying the existing COTs ink for printed electronics through EHD printing.

4.2 Introduction

Inkjet printing is one of the promising printing techniques for fabricating conductive tracks on various substrate materials. Traditionally, most of the inkjet printing systems have been employed in the print media [99]. Over the years the piezoelectric and thermal inkjet technology has matured and there is now a plethora of commercial piezoelectric and thermal inkjet printers. However, inkjet printing based on the piezoelectric inkjet principle has attained significant attention in life science applications since the dynamics of printing is done without varying the temperatures and ink is less susceptible to thermal degradation. Life science applications, such as proteomics, DNA sequencing, tissue, and cell manipulation [139–145] along with the applications in printed electronics [146–149], are now seemingly growing. Despite the growing usage of inkjet printing in emerging areas, most of the formulated ink needs to operate within a certain ink dynamics envelope. Therefore, intricate processes are required not only for formulating the ink for a specific purpose but also the surface properties of the substrate need to be catered while synthesizing the ink. Due to the complex nature and customized requirements which are often challenging, inks for inkjet printing needs to be tuned for jettability and producing consistent patterns during the printing process.

Moreover, use of a piezoelectric inkjet system for conductive printing of tracks for printed electronics requires further refinements since the ink contains conductive nanoparticles which are susceptible to agglomeration which requires a greater piezoelectric ejection

TABLE 4.1: General viscosity ranges of contactless and contact printing methods.

Parameter	**Viscosity Range (mPas)**
Thermal Inkjet	1-2
Piezo Inkjet	5-30
Gravure	50-200
Flexography	50-500
Screen	1,000-10,000
Offset	40,000-100,000

force during the printing process. Cleaning of ink cartridges after printing, viscosity, surface tension and substrate properties play a vital role in preparing ink particularly for piezoelectric inkjet printing. Additionally, attaining higher resolution with piezoelectric inkjet printing is also a big issue. In order to improve the print resolution the ejection diameter of the nozzle needs to be reduced. When the diameter of the nozzle reduces it increases the wall forces in the nozzle appreciably, and the piezoelectric ejection forces need to increase accordingly. Due to this constraint, the use of smaller nozzle diameters with higher concentrations of conductive nanoparticles is a big challenge.

Electrohydrodynamic (EHD) printing involves pull forces instead of push forces generated by the counter electrode electric field. Since, the liquid is pulled from the nozzle therefore, it forms the shape of a cone from the ejecting nozzle. The cone shape of the liquid improves the resolution of printing and the possibility of improving the resolution of printing of conductive tracks can be realized. EHD inkjet printing not only provides the possibility of using a high concentration of nanoparticle-based ink for printing purposes, but the overall process can have different printing modes such as drop-on-demand, continuous and spray mode inkjet printing. Table 4.1 outlines the viscosity parameters of the ink for various kinds of printing method [150].

Although EHD printing provides benefits, a suitable ink for printing, especially on flexible substrates, is not commonly available due to there being very few suppliers of COTs EHD printer. Most of the conductive inks for printed electronics are either based on gold [151–154], silver [155–159] or copper [79, 160–163] metallic particles. However, silver is low-cost compared to gold and is less susceptible to the environment than copper. Almost all the conductive ink printing through inkjet printing requires post curing or sintering processes to remove the solvent carrier of the conductive nanoparticles to form the conductive tracks. However, it is often seen that conductive tracks tend to develop

cracks during the sintering process, rendering the overall printing futile. This behaviour occurs predominantly when the substrate is flexible and expands with the increase of temperature during the sintering process.

As a general principle, modification of the ink can be effective in preventing the development of cracks during the curing process. With this in mind, we conducted a series of experiments on an in-house developed EHD system with a COTs ink procured from Novacentrix. The details of the EHD system can be found in our early experiments [164]. Using the ink as obtained resulted in cracks in the printed tracks. However, when the ink was modified the cracks were eliminated/reduced. This paper presents the details of the printing experiments, and the ink modification steps and procedure.

4.3 Materials and Methods

In this work, a 101.6 μm commercially available overhead transparency (OHP) sheet from 3M PP2900 was used as the substrate for printing the conductive lines. The substrate was mounted on the copper plate on which small holes of diameter 0.5 mm were drilled. The plate was then fixed by means of screws onto an aluminium machined plate which was connected to the vacuum pump. Once the vacuum pump was in operation it created a vacuum which then holds the substrate firm in-place over the copper plate. To avoid sagging of the substrate under vacuum, a series of 3D printed pillars were inserted between the aluminium suction plate and copper cladded printed circuit board (PCB) plate. Holes on the copper cladded plate were drilled with the help of a ProtoMat S62 PCB milling machine by LPKF Laser & Electronics, USA, at a spacing of 10 mm with the offset distance of 5 mm to the next row on a length of 100 mm by 100 mm. Thus, the overall substrate which can be held firmly on the X-Y stage was around 100 mm x 100 mm. The thickness of the copper cladded PCB plate was 1.2 mm with a copper thickness of 35 μm.

Before fixing the copper plate to the vacuum chamber the copper plate was finely sanded to remove any burrs or unevenness which can occur due to the drilling of the minute holes for the vacuum. The copper plate was then connected to the ground electrode for the electrohydrodynamic ejection of liquid from the nozzle. The bottom of the aluminium suction plate was then mounted on the heating plate, which provided the insitu heating

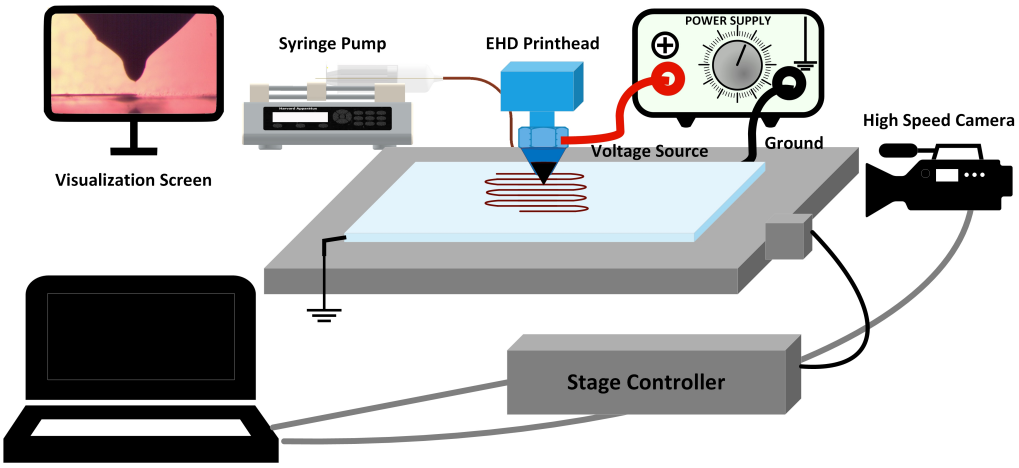

FIGURE 4.1: Layout of the EHD printing system.

of the substrate during the printing process below the glass transition temperature of the PET substrate. A pictorial layout of the EHD system is shown in Figure 4.1.

Conductive inks from Novacentric® USA were used to produce the conductive tracks through EHD printing. Four different types of inks were used based on two different solvents, namely Diethylene glycol (DEG) and Ethylene glycol (EG). Metalon® JS-A102A and Metalon® JS-A211 inks from Novacentric® USA, were based on DEG solvent base with the exception that the later included a fluoropolymer binder. On the other hand Metalon® JS-A191 and Metalon® JS-A291 includes EG solvent with JS-A291 containing a small quantity of polyurethane binder. The role of the binder was to enhance the ability of inks to be printed on bendable flexible substrates at the expense of a little increase of resistivity. It was also noted that the fluoropolymer-based inks provided better inhibition towards oxidation when compared to the polyurethane binder [165–167]. Additional details of the inks can be found in Table 4.2.

All the inks were tested on the OHP PET substrate for their printability on a low cost commercially available substrate. Moreover, these inks were also altered with silver flake based screen printed ink from Novacentric® USA (HPS-021LV) with properties mentioned in Table 4.3. HPS-021LV is a high concentration silver flake (AgF) ink having 75% (wt/wt) of Ag loading with diethylene glycol monobutyl ether (DGME) as the solvent base. The modification process involved addition of isopropyl alcohol (IPA) to enhance the miscibility of the HSP-021LV ink with the piezoelectric inkjet ink. First the AgF-DGME HPS-021LV ink was added in IPA in such a way that the overall ratio of the Ag remained 40% by weight similar to the Ag content of the piezoelectric inkjet

TABLE 4.2: Metalon® piezoelectric inkjet printer physical properties

Parameter	**Metalon® JS-A102A**	**Metalon® JS-A191**	**Metalon® JS-A211**	**Metalon® JS-A291**
Viscosity (cP)	8-12	8-12	8-12	8-12
Ag Content (wt/wt %)	40%	40%	40%	40%
Surface Tension (Dyne/cm)	18-22	27-32	28-32	28-32
Z-avg particle size (nm)	28-40	30-45	30-50	30-50
Specific Gravity	1.6	1.6	1.6	1.6
Solvent	Diethylene glycol(DEG)	Ethylene glycol(EG)	DEG with fluoropolymer binder	EG with Polyurethane binder

TABLE 4.3: Novacentric® HPS-021LV screen printed ink physical properties

Parameter	**HPS-021LV (Water based Ag flake ink)**
Viscosity (cP)	>1000 (Brookfield spindle LV #4, 30 rpm)
Ag Content (wt/wt %)	70-75%
Z-avg particle size (μm)	D50 = 2.0 micron, D90 = 4.0 micron
Specific Gravity	3.1
Solvent	Diethylene glycol monobutyl ether

ink. This brought the overall concentration of Ag particles closer to the AgNP weight ratio of the inkjet printing ink. The AgF-DGME and IPA underwent ultrasonication for 1 hour and subsequent magnetic stirring to avoid agglomeration of the AgNP and to ensure even distribution of AgNP in IPA. Later the HPS-021LV-IPA composite ink was added to the piezoelectric inkjet inks by varying the ratio of HPS-021LV-IPA composite ink from equal volume ratio and increasing the ratio by one fourth (25%) by volume to test and evaluate the printability of the ink on the substrate.

Prior to printing, the PET substrate was cut into 110 mm by 110 mm square sheet suitable for printing platform. Then the substrate was washed with deionized water, dried and cleaned with isopropyl alcohol. After that, it is purged by Nitrogen before the printing process. Conductive ink was delivered to the nozzle with the help of 0.19 mm diameter fluidic connector with a syringe pump. Connection from the syringe pump to the nozzle was done by the COTs hypodermic needle. This was to avoid a volume of printing ink becoming trapped inside the Luer lock hub. All these modifications

resulted in the precise control of the flowrate and instantaneous changes in the shape of the meniscus were observed as the flowrate from the syringe pump was regulated.

During the printing process the temperature of the substrate was maintained above the glass transition temperature of the PET substrate at 80 °C. However, while the temperature was slightly above the glass transition temperature, PET can retain its mechanical properties due to its high crystallization and melting temperature [168, 169]. Further details of the nozzle head design and respective ejection phenomenon can be found in our previous work [164]. The overall process of preparation of the conductive ink, EHD printing and conductive track evaluation via optical and SEM images is depicted by Figure 4.2.

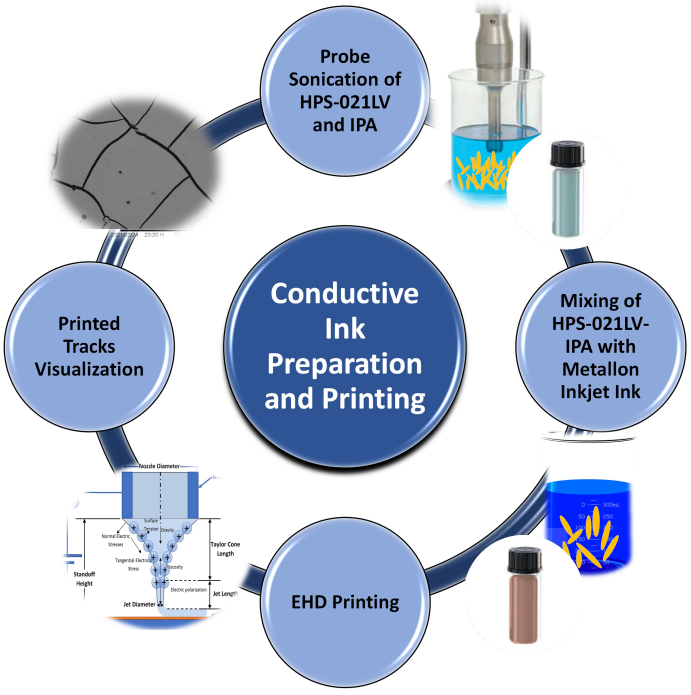

FIGURE 4.2: Process flow of conductive ink preparation and conductive tracks evaluation.

4.4 Result and Discussion

For the conventional inkjet printing method, the conductive particles were subjected to very fine ball milling process to decrease the size of the particles since piezoelectric printhead was prone to clogging. Generally, in inks for piezoelectric inkjet, particle size less than 100 times the diameter of the nozzle is preferable [170–172]. However, recent

developments in the EHD inkjet printing allows larger size of nanoparticles ink to be used for high resolution printing purposes [173].

As the AgNP are mixed with solvent and binders, there is still separation between the NPs during the sintering process. The solvent plays two important roles in the ink formulation. The first is to act as a vehicle to fuse the conductive NP during the sintering process, and the second is to adjust the viscosity and surface tension of the ink so that the ink can be used for a particular inkjet printing process. In our case, EHD printing has the advantage that it can operate over a wider range of viscosities and surface tension [171, 174]. However, during the post printing or insitu ink sintering process, the evaporation of the ink induces stress either through rapid evaporation or due to coefficient of expansion (COE) of substrate, resulting in the ink developing cracks. The amount or width of the cracks can be reduced by changing the sintering temperature profiles or overlapping the tracks with the ink by repeated printing [175–177]. However, the downside of these strategies is that the sintering process take more time to cure the ink and the printed tracks is still prone to cracks with slight bending. Conversely, the repeated printing increases the stiffness of the conductive tracks again limiting the flexibility/bending of the substrate [178, 179].

Evaporation rates of the solvent and binder in the ink also plays an important role during the sintering process and formation of cracks. Often the solvent and binders are selected such that the evaporation rate of the ink is slow and can only be expedited once the overall printing has been finished either through thermal curing or through the application of intense pulse light (IPL) ultraviolet (UV) curing [180–182].

In our investigation, the printed lines with the COTs inkjet inks were prone to cracking after the sintering process. After the printing of the ink, it was cured thermally at 100 °C for two hours to produce the sintered tracks. During the curing process sintering of the silver nanoparticles takes place in two steps. In the first phase the solvent evaporates due to its low evaporation temperature. Therefore, the NP lose their organic shell and nanoparticle interaction or contact starts to form. Once all the organic material is evaporated, the AgNPs fuse together to form the conductive tracks. We noted that each of the printed tracks from the Metalon® inks produced cracks, as shown in Figure 4.3. The overall width of the cracks was less than 5 μm. The reason for the formation of cracks during the EHD printing was due to the focusing of ink at the conejet which

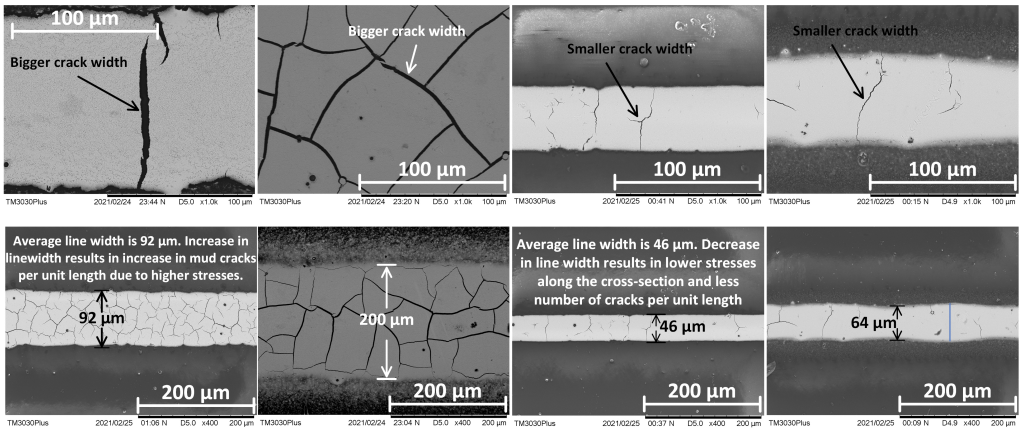

FIGURE 4.3: SEM images of conductive tracks printed with EHD printing depicting formation of cracks at various resolutions.

resulted in more ink deposition at the centre of the ejecting nozzle and ink forming a concave cross-sectional profile. The ink used for the deposition of the conductive tracks on the substrate had been developed for piezoelectric actuation which spreads a similar amount of ink across the cross-section of the deposition. Therefore, during the drying process the sintering is uniform across the cross-section of the deposited ink, which avoids mud crack development. On the other hand, when the same ink is deposited through the EHD printing the ink forms a conejet which results in the improvement of the resolution during the deposition of ink on the substrate. However, the resulting ink volume at the edges of the line is less as compared to the ink volume at the centre of the deposited ink. The differential volume across the cross-sectional area induces the stresses during the drying or thermal curing process. Development of stress during the thermal curing process results in formation of mud cracks.

Figure 4.4 highlights the images of the printed tracks through EHD printing. The optical microscopic image clearly shows that at the centre of the printed line, the printed lines are reflective or have high contrast due to optics focusing on the top layer. The contrasting region clearly shows that the ink is focused on the apex of the conejet in the EHD printing, thus creating a differential volume deposition during the EHD printing process across the crossection of the printed feature. We envisaged that the differential volume expedited the uneven loss of solvent across the cross-section of the printed lines, thus developing stresses in the printed lines. Moreover, the coefficient of expansion of the substrate further aided the formation of cracks in the printed cracks, when the individual size of the metallic nanoparticles in the ink were smaller than the cracks void.

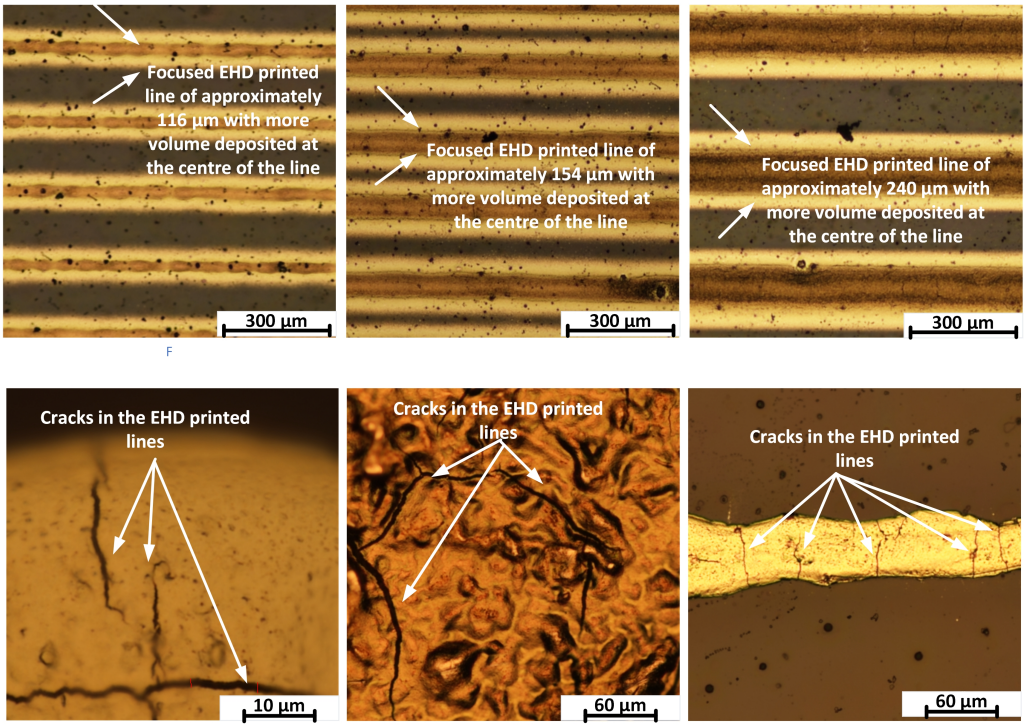

FIGURE 4.4: Optical images of conductive tracks printed with EHD printing depicting high aspect ratio printing and formation of cracks.

Figure 4.5 shows a cross-sectional SEM image of the printed lines. The SEM shows the aspect ratio of the printed line of width of around 60 μm. The cross-section forms the semi-elliptical shape along the x-axis depicting higher volume of ink being deposited at the centre of the line, forging the concept of high aspect printing of the ink through EHD printing.

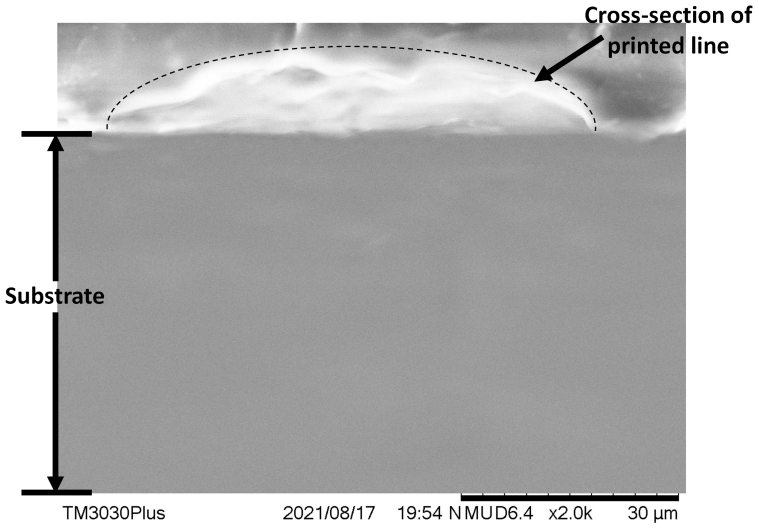

FIGURE 4.5: SEM image of the cross-section of the conductive printed line through EHD printing.

Figure 4.6 shows SEM images of the EHD printed conductive tracks of the composite AgNP and AgF ink. The conductive tracks show no signs of cracks for various EHD line widths. From the AgNP based EHD printed conductive tracks we noticed that the cracks developed predominantly on higher in density whenever the line width is larger. This indicates that for a wider line width the development of stresses is much higher than stresses in smaller printed line widths. However, from the AgNP and AgF IPA composite ink even the tracks which were bigger than 100 μm were free from any cracks. The printed line width ranges from 5 μm to more than 200 μm as shown in Figure 4.6. However, further improvement of the line resolution was not possible through the composite ink due to the presence of larger particles of AgF.

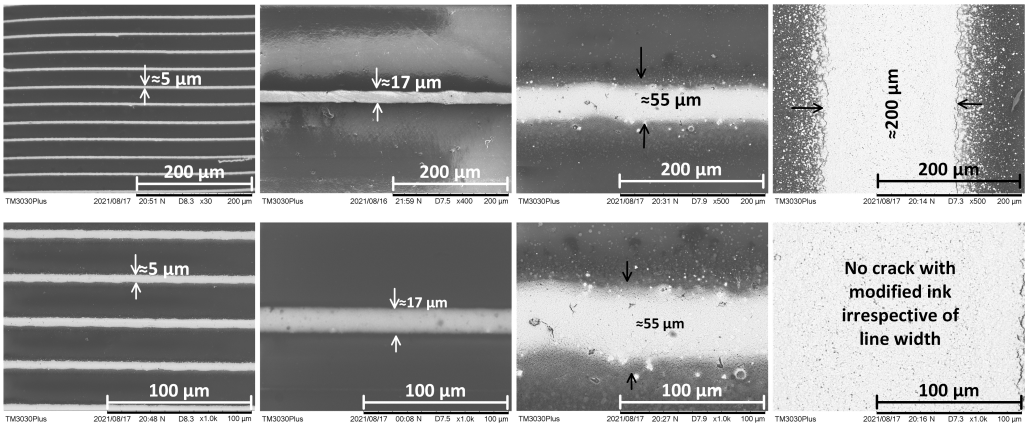

FIGURE 4.6: SEM image of the crack free printing of conductive composite ink through EHD printing.

The piezoelectric inkjet ink was based on AgNP of diameter less than 50 nm. Whereas, the AgF-DGME HPS-021LV screen printing ink had an average particle size of 4 μm. AgF-DGME HPS-021LV IPA solvent was mixed with AgNP piezoelectric ink with an increasing ratio starting from equal ratio by volume. Gradually the ratio of AgF-DGME HPS-021LV IPA was increased by 25% (by volume) in all the piezoelectric ink to prepare other composite formulation for the EHD printing purpose. We used the nomenclature of JS A102A:SNF-IPA for the Metalon® JS A102A and AgF-DGME IPA composition. Breakdown of each composition of the composite ink can be seen in Figure 4.7.

The composite ink was then spin coated at 3000 rpm to form the homogeneous mixture and even coating on the substrate to test the sheet resistance of the prepared ink. The sheet resistance of the spin coated ink on the PET substrate increased with the increased concentration of AgNF. This showed that higher AgF concentration resulted in the lower

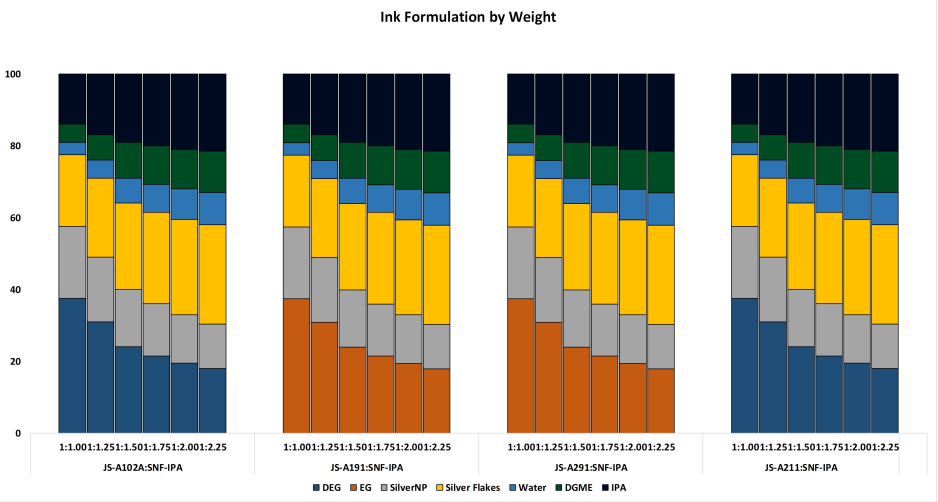

FIGURE 4.7: Ink formulation by weight ratio

conductivity since the average size of Ag particles in the composite ink was increased. On the other hand, bigger particle size of AgF acted as a crosslinking agent between the micro cracks and resulted in the crack free printed lines. JS A102A and JS-191A based composition showed excellent conductivity and no signs of cracking. However, JS-211A and JS-291A ink composition has lower conductivity when compared with the other formulations, nevertheless the cracks in the conductive patterns were not present. It is envisaged that the lower conductivity of the JS-211A and JS-291 ink is due to the inclusion of polyurethane and fluoropolymer binder. The polymer binders provide the ink to retain its conductivity during repetitive bending. Figure 4.8 shows the graph of sheet resistance for each type of the prepared composite ink.

4.5 Conclusion

In this work, a simple method has been presented to mitigate the cracking behaviour of a COTs ink for piezoelectric inkjet printer through investigation of the microstructure of the developed cracks during the EHD printing process. It has been found that the tendency of ink to develop cracks can be avoided by adding the filler AgNFs particles longer than the crack width. The filler AgNFs acts as a nanowire to fill the cracks. We also noted that the increase in the amount of the AgNFs increased the conductivity of the ink. The AgNFs and AgNPs composite ink is compatible with EHD printing. The highest resolution of 6 μm was achieved during the EHD printing of composite ink.

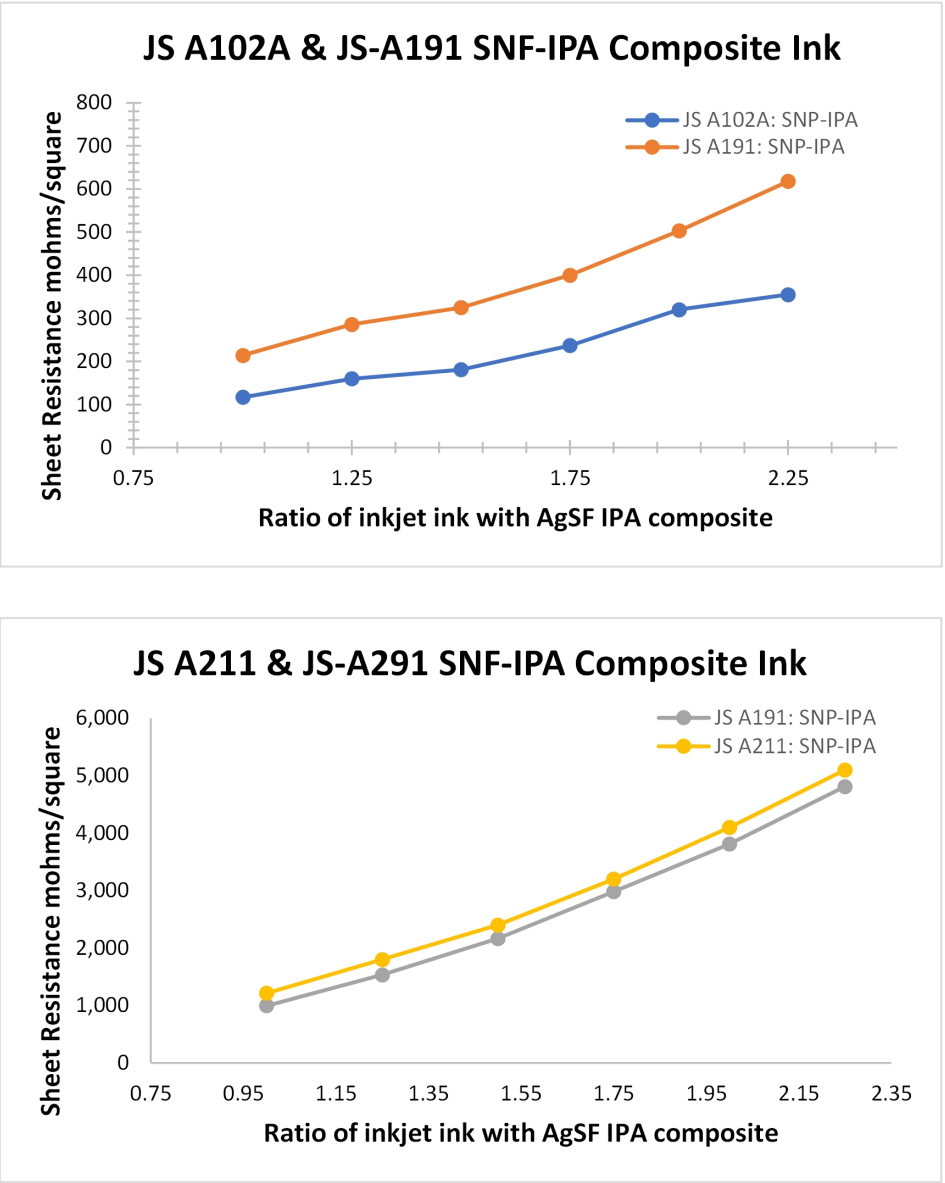

FIGURE 4.8: Sheet resistance of AgNP - AgF IPA ink for various concentration of ink.

The line width was wider for the composite ink as it was composed of 4 μm AgNFs. However, the inclusion of larger AgNFs helped mitigate the development of the cracks in the printed features. Moreover, higher amount of AgNFs further increased the line width of the printed feature but the sheet resistance was decreased with the increase of AgNFs. The average sheet resistance of the prepared ink varied from 100 milli ohm per square to 4 ohm per square (for higher concentration of AgNFs by volume).

Chapter 5

Study of Microchannels Fabricated using Desktop Fused Deposition Modelling Systems

5.1 Abstract

Microfluidic devices are used to transfer small quantities of liquid through micro-scale channels. Conventionally, these devices are fabricated using techniques such as soft-lithography, paper microfluidics, micromachining, injection moulding, etc. The advancement in modern additive manufacturing methods is making three dimensional printing (3DP) a promising platform for the fabrication of microfluidic devices. Particularly, the availability of low-cost desktop 3D printers can produce inexpensive microfluidic devices in fast turnaround times. In this paper, we explore fused deposition modelling (FDM) to print non-transparent and closed internal micro features of in-plane microchannels (i.e. linear, curved and spiral channel profiles) and varying cross-section microchannels in the build direction (i.e. helical microchannel). The study provides a comparison of the minimum possible diameter size, the maximum possible fluid flow-rate without leakage, and absorption through the straight, curved, spiral and helical microchannels along with the printing accuracy of the FDM process for two low-cost desktop printers. Moreover, we highlight the geometry dependent printing issues of microchannels, pressure developed in the microchannels for complex geometry and establish that the profiles in which

flowrate generates 4000 Pa are susceptible to leakages when no pre or post processing in the FDM printed parts is employed.

5.2 Introduction

Microfluidics, the science and technology of manipulating fluids at micro to millilitre scale through internal features, has been applied in various applications such as point-of-care diagnostic tools, therapeutic devices, and air and water quality monitoring methods [183–188]. Currently, popular manufacturing techniques for producing microfluidic devices include soft lithography [189], paper microfluidics [190, 191], micromachining [192], injection moulding [193], hybrid paper based open channel microfluidics [194], etc. Soft-lithography using polydimethylsiloxane (PDMS) micro-moulding is widely used method as PDMS is optically transparent, chemically inert, and gas permeable material with low-surface energy [195]. However, most of these methods are expensive, time-consuming, require multi-step processing in a cleanroom. Additionally, it is quite difficult to change device design [196]. Recently, 3-dimensional printing (3DP) is rapidly gaining attention in the field of microfluidics. The prominent fabrication techniques for microfluidics are fused deposition modelling (FDM), selective laser sintering (SLS), stereolithography (SLA), Xurography and inkjet printing [197–201]. These methods have various advantages like automated fabrication, cost-effectiveness, availability of a wide range of materials, single-step procedure, etc. [195, 202–204]. Moreover, 3DP does not require a photomask, photoresist, or access to a cleanroom. This allows a major reduction in the material cost, creates the possibility of mass manufacturing, and saves significant development time [195].

The literature shows that 3DP methods such as FDM [151, 183, 205–208], SLA [209, 210], and inkjet printing [211] have been used in the field of microfluidics. Symes et. al [184] printed the reagents directly into a 3D reactionware for organic and inorganic synthesis using FDM. Similarly, Anciaux et. al [212] fabricated a micro free-flow electrophoresis device with a consumer-grade 3D printer. The performance of FDM, SLA, and polyjet printers have been compared with the help of microfluidic chip including sealed and open-channel micro-mixers [151, 213–215].

The performance of 3D-printing devices depends upon the choice of process. In microfluidic applications, Stereolithography (SL) printing has been employed widely which works on the principle of curing a photopolymer resin layer-by-layer [216, 217]. However, conventional SL resin is susceptible to toxicity and is not biocompatible [218]. Development of non-toxic and biocompatible SL resin can be expensive and requires rigorous experimentation. In this regard, FDM printing is cost-effective and offers a choice of the biocompatible materials. Moreover, the low cost of FDM printer makes it one of the promising 3D printing technologies for fabricating non-toxic devices, which are essentially required for Lab-on-a-Chip applications. Despite the aforementioned benefits of FDM additive manufacturing, there are applications where other AM techniques can provide better microfluidic devices to study, investigate or harness the physical phenomenon at micro or sub micro level. In this regard Table 5.1 summarizes the methods of fabrication, advantages and limitations of prominent AM and other microfluidic fabrication techniques which can be utilized to fabricate different functional microfluidic devices of interest.

TABLE 5.1: Comparison of prominent additive manufacturing and other microfluidic fabrication techniques

Fabrication Technique for Microfluidics	**Process**	**Typical Microfluidic Resolution (μm)**	**Advantages**	**Disadvantages**
Stereolithography	Point by Point laser scanning of photocurable resin	10–200 [219–221]	High resolution, can produce smoother and large parts with the capability of fabricating internal channels of microfluidics	High capital cost of equipment, photocurable raw material is often expensive and unsuitable for bio applications, printing parameters are intricate, and the equipment requires calibration for consistent print results
FDM	Layer-by-layer deposition of thermoplastic polymer extruded by applying heat and extrusion force to form 3D-printed features and microchannels	400–1000 [187, 222, 223]	Low cost of equipment, printing material is biocompatible and low cost. Can produce highly complex internal microchannels with moderate sub-millimetre resolution	Limited printing resolution and material often not suitable for high temperature applications
Selective Laser Sintering	Point by Point laser induced sintering of ceramic or metal particles to produce 3D parts	100-600 [224]	Strength of parts is good, can produce parts with higher resolution and fabricated parts can be used in high temperature applications	High capital cost of equipment. Due to sintering the surface is rough, cleaning of internal microchannels is difficult
Soft Lithography	Stamping and moulding of elastomeric materials such as PDMS through contact printing, stamping or master mould imprinting [225].	0.05–0.5 [226]	Produces high-resolution microchannels, fabricated devices are biocompatible [221]	Permeable for certain liquids and microchannels can swell due to reaction with certain chemicals. Multistep process, stripping of mould requires precision and expertise. Fabrication of complex 3D microchannel is difficult [227]

Fabrication Technique for Microfluidics	**Process**	**Typical Microfluidic Resolution (μm)**	**Advantages**	**Disadvantages**
Inkjet Printing	Drop-on-demand (DoD) piezo inkjet printing of ink which can be used to form open-channel microfluidic, to form microfluidic path for positive or negative photoresist to use for etching or to form layer by layer adhesive structure for microfluidic applications	42–300 [228]	Low cost, high speed, configurable and multi-material parts can be manufactured [229].	The strength of fabricated devices is low for enclosed channels and fabrication of internal microchannels requires further processing or processes
Xurography	Shearing of material through a sharp knife controlled through a computer-controlled software instructions [199].	15–250 [200, 201]	Low cost of equipment, high speed and large-area fabrication.	Complex 3D microchannel is extremely difficult to produce.

Most of the microfluidic devices involve micro-mixing of reagents. In these applications, the process is primarily dependent upon diffusion of two different flows. The flow rate and channel length are important parameters to achieve effective mixing [213]. Additionally, the design of microchannel, it's size, and the effect of fluid pressure should be considered to explore the possibilities of leakage through the microfluidic devices. Furthermore, FDM printers leave voids while printing the part (Fig. 5.1) as layers are not uniformly bound. Hence, it is also important to characterise the microchannels for their mechanical characteristics.

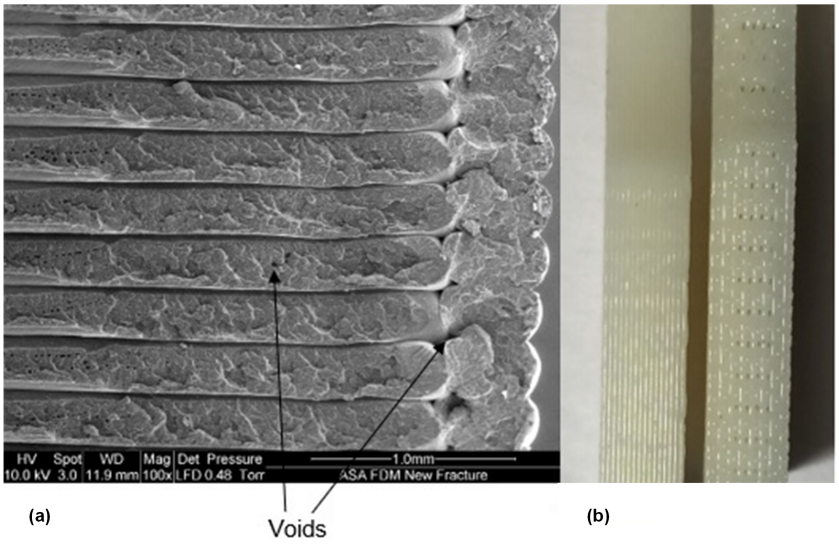

FIGURE 5.1: Voids in the FDM printed parts. a) Scanning electron Microscope (SEM) image showing usual voids inherent to the FDM process. b) Optical image of a dog-bone sample with clearly seen voids.

In this paper, we explore the possibilities of using FDM technology for developing the internal features of the microfluidic devices with non-transparent materials. The internal features consisted of in-plane profiles (i.e. linear, curved and spiral microchannels) as well as microchannels with varying cross-section in the build direction (i.e. helical microchannel).

The comparison of pressure developed was performed based on the minimum possible channel size, fluid flowrate, and leakage in the microchannel body. Furthermore, FDM printed parts have been analysed to observe the absorbance of the fluid due to the presence of voids in the layers. Also, the effect on the microchannels part weight with respect to flowrate after cleaning it with acetone has been included and discussed.

5.3 Materials and Methods

Two FDM printers with 0.4 mm nozzle were used in this study: 1) a Tiertime UP 02 (referred as UP02) and 2) an Original Prusa i3 MK3S (referred as Prusa). The UP02 was controlled through UPStudio software and the Prusa was used with Prusa Slicer and Pronterface softwares. The models for 3D parts were constructed using parametric 3D modelling software Autodesk Inventor Professional 2020. One of the main requirements for the microfluidic application in biomedical applications is their biocompatibility [230–232]. For this purpose, we chose polylactic acid (PLA) printing material, which is biodegradable and does not leave a hazardous footprint in the environment. Moreover, it has low warping deformation and overall printed parts exhibit excellent dimensional accuracy and quality [233, 234]. The spool of PLA filament having a diameter of 1.70 mm was used to deposit the layers of modelled microfluidic channels. Pico Plus Syringe Pump from HARVARD APPARATUS was used for injecting the water at different flow rates. Pressure measurements were performed with the help of a PX3 Series heavy-duty Honeywell pressure transducer having pressure measurement range of 0 to 8600 kPa with total error band (TEB) of ±1% full-scale span (FSS). Sartorius ENTRIS64-1S analytical balance was used for the weight analysis.

TABLE 5.2: Printer specifications and selected parameters.

Specifications	**Tiertime UP 02**	**Prusa i3 MK3S**
Make	Tiertime	Prusa Research
Software	UP Studio	Prusa Slicer and Pronterface
Machine Dimensions	245x350x260 mm	550x400x500 mm
Build Volume	140x140x135 mm	250x210x210 mm
Material Used	PLA (1.7 mm)	PLA (1.7 mm)
Nozzle diameter	0.4 mm	0.4 mm
Support Structure	No Support	No Support
Layer Thickness	100 μm	100 μm
In-Fill	100 %	100 %
Price	799 USD [235]	749 USD [236]

5.3.1 Fabrication of microchannels

Four types of microchannels (linear, curved, spiral along layer and helical, where microchannel is also moving perpendicular to the layer) were designed with different diameter sizes. These microfluidic channels were fabricated using FDM. Different flow rates were applied on the channels for the pressure measurement. The FDM printer was optimised with nozzle temperature at 207°C and platform temperature at 68°C to achieve the best results during the printing process with both the FDM printers. Other process parameters and specifications of the printers are summarized in Table 5.2.

The channel design consisted of an inlet port, the main channel, and the outlet port. The inlet port is connected with the syringe pump which is then connected with the pressure reservoir. The top of the pressure reservoir is connected with the pressure sensor. Outlet port of the pressure sensor reservoir was connected with a luer lock connector which can be easily attached via a conventional hypodermic needle bonded with the inlet port of the fabricated microchannels. Any change in the pressure induced by the change of the flowrate at a specific microchannel diameter was then recorded by the pressure sensor. The output signal of the pressure sensor in voltages was then converted to the pressure through the characteristic curve of the sensor provided by the OEM of the sensor. The inner diameter of the inlet port of the printed microchannel was kept constant at 0.55 mm so that the 25-gauge hypodermic needle can easily be inserted to the inlet port of the microchannel. whereas, the diameter of the main channel was fabricated with various diameter sizes (0.25 mm, 0.3 mm, 0.35 mm, 0.4 mm, 0.45 mm, and 0.5 mm). The connection with the inlet port of the printed microchannel was secured by using the 3M™Scotch Weld™epoxy adhesive DP125 having a tensile strength of 17.23 MPa with the hypodermic needle. The outlet port with a diameter of 0.3 mm was used to connect the silicone tubing. In the linear channel (Fig. 5.2 a and b), length of the main channel was kept at 50 mm and the distance between each of the 4 walls was set at 5mm to avoid immediate leakage possible depending upon the control on the print settings from the slicer software. On the other hand, for the curved channel, the path consisting of 6 half circle turns of 1 mm diameter and 7 straight paths with the total linear length of 50 mm. Spiral channel also designed with the same philosophy of keeping the overall length of the microchannel up to 50 mm while the injection port was matched with the syringe outer diameter.

FIGURE 5.2: (a) CAD models of the linear, curved, spiral and helical microchannels (b) Pictorial view of the connected inlet and outlet ports of the FDM printed linear, curved, spiral and helical microchannel.

5.3.2 Characterisation

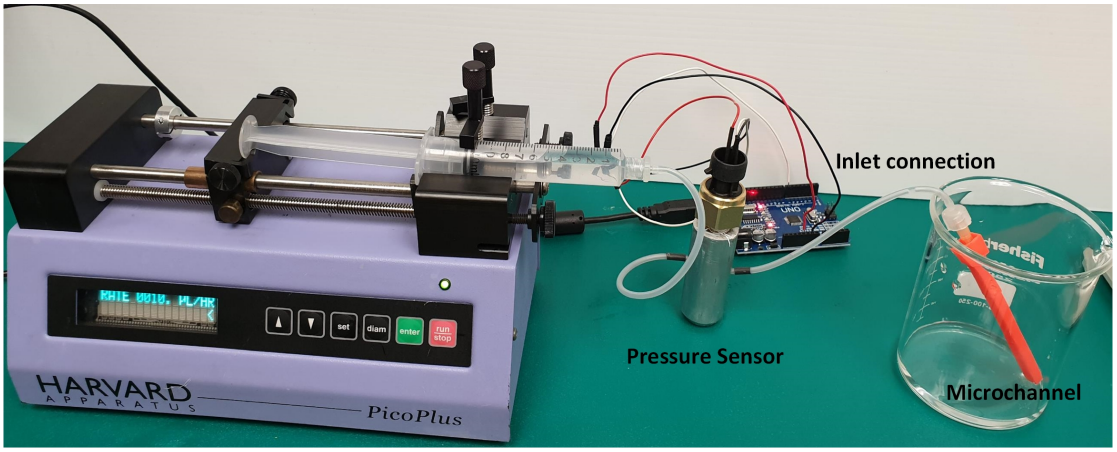

FIGURE 5.3: Pressure measurement experimental setup.

The printed results from the FDM printer shows that the accuracy of the printer not only varies with the type of the printer, but it also varies if the microchannels are along the print layers or perpendicular to the print layers. For instance, when the microchannels are along the printing layers the smallest achievable microchannels with the off-shelf Up printer was around 250 μm whereas when the geometry of the channel changes and microchannels follows the path which is perpendicular to the build layers the size of the microchannels needs to be increased to 900 μm to be able to achieve the flow across the microchannels while keeping the print settings similar to the other geometry. This study provides a practical demonstration of the same through pressure developed across the flow of the minimum possible channel size.

To ascertain the quality of the print, we measured the surface roughness of the printed parts. The measurement of the printed specimen was done by a surface roughness profilometer from STARR instrument model RTD-210. The surface roughness profilometer stylus measurement probe had a low contact force of 4 mN and a tip radius of 5 μm having 90° cone angle of diamond tip. The profiling speed for the test was maintained at 0.5 mm/s resulted in the overall accuracy of 4 nm/$\pm$40 μm in Z-axis and Gaussian filter has been selected to suppress the noise during the measurement of the surface roughness. All the printed FDM parts were printed at an angle of 45° therefore, the tip of the profilometer was held at an angle of 45° for each measurement with respect to the printed surface. The tracing path was auto-levelled with a sampling cut-off length of 0.8 mm and measuring range of 4 mm.

Linear, curved, and spiral microchannels have been characterised in the paper. The characterisation was performed to obtain the minimum possible diameter with each technology. Additionally, the maximum possible flow rate without any leakage through the channels was studied. The experimental set up is explained in Fig. 5.3. Initially, all the printed channels were cleaned with compressed air jets. To ascertain the leakage from the body of the microchannel the consumed water was dyed blue and was injected at different flow rates (varying from 0 to 40 μL/min. in steps of 5) was injected at the input port with the help of the syringe pump. A disposable, 60 mL syringe was actuated on the syringe pump. For each measurement, the syringe pump was operated to dispense enough liquid so that a stable reading at the pressure sensor can be recorded. A pressure sensor was placed in-between the syringe pump and the input port of the channel for corresponding pressure measurement. The pressure was obtained as voltage value which, in turn, was converted into pressure value (Pa) using the datasheet. The change in flow-rate at the input port resulted in a change in pressure at the input port and leakage was observed in the microchannel.

Generally, the voids present in the FDM printed parts are responsible for leakage or water retention. Hence, the effect of acetone cleaning on the microchannel surface was analysed. This was based on the idea that the additives in PLA may react with acetone and melt to fill the gaps and voids inside the microchannel. Acetone was circulated through the FDM printed microchannels for 10 minutes. Furthermore, printing accuracy test for FDM printer was performed by simultaneously printing 8 microchannels of each size and weighing each part separately on the analytical balance.

5.4 Results and Discussion

The average surface roughness of each type of microchannel fabricated with FDM printer has been provided in Fig. 5.4 and the respective parameters of surface roughness profile are mentioned in Table 5.3. The peak height for all the channels was within ± 10 μm. Surface roughness of each print having the same microchannel design is averaged to calculate the resultant surface roughness of the parts. The variation of the surface roughness is due to the change in the profile of each specimen and printing orientation of the specimen or profile feature. Surface roughness values depends on the print setting such as the nozzle diameter, layer thickness, infill properties and layer over-lapping.

TABLE 5.3: Surface roughness profile parameters

Parameter (all values are in μm)	**Straight Channel**	**Curved Channel**	**Spiral Channel**	**Helical Channel**
Roughness Average, R_a	0.598	1.817	2.170	2.907
Average Maximum Height of the Profile, R_z	4.013	11.334	13.343	16.396
Maximum Height of the Profile, R_t	4.888	13.146	16.740	21.784
RMS Roughness, R_q	0.794	2.241	2.713	3.570
Maximum Profile Peak Height, R_p	1.147	6.071	5.906	6.575
Kurtosis, R_{ku}	4.787	2.712	3.049	3.876
Skewness, R_{sk}	1.137	0.150	0.524	0.750

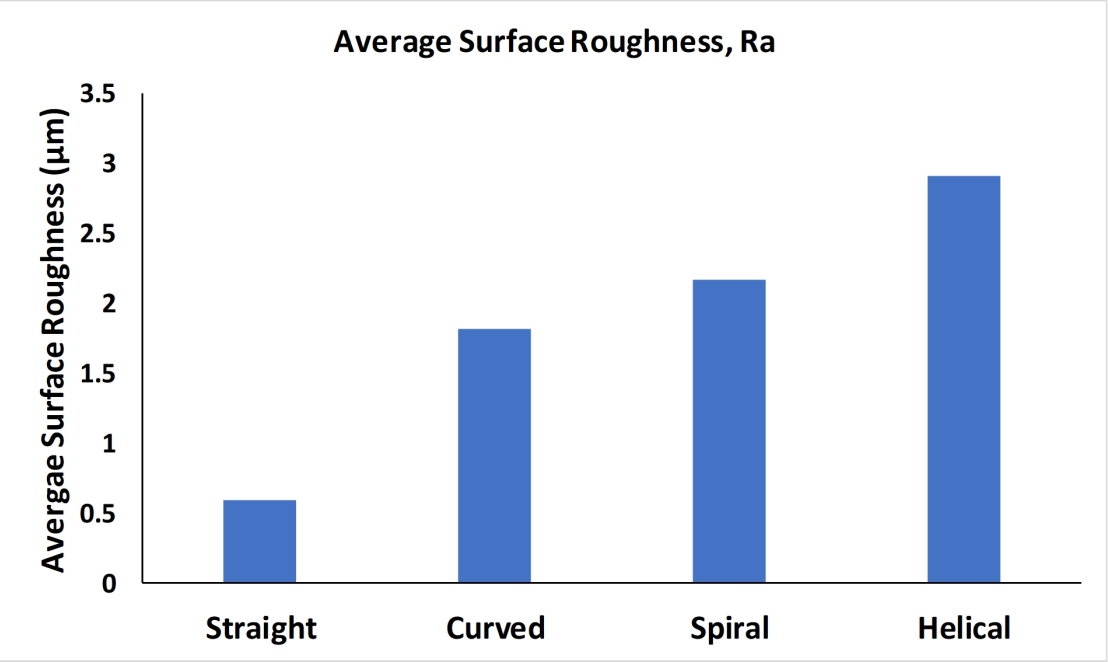

FIGURE 5.4: Average surface roughness (Ra) of straight, curved, spiral and helical microchannels.

The microchannels created using the FDM method having diameters ranging from 0.25 mm to 0.5 mm did not have any blockages. The water was passed through the FDM method based microchannels to study the effect of various flow rates on the leakage. Figure 5.5 shows the leakage across the body of the FDM printed linear microchannel when the pressure developed along the microchannel is excessive at a particular flow rate and instigates the leakage from the layers of the microchannel body.

The accuracy of the printer to replicate the channel was also determined in the paper. This was achieved by printing a total of 8 samples of each diameter (0.25, 0.3, 0.35, 0.4, 0.45, and 0.5 mm) at the same time individually. A default base support structure

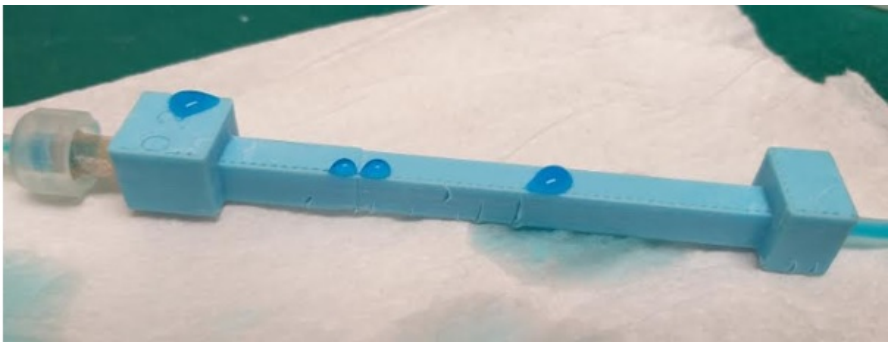

FIGURE 5.5: Leakage in the FDM printed linear microchannel.

was carefully removed using scrapper and filament cutter to ensure to obtain the accurate readings without damaging the part. Each microchannel weight was individually recorded on the analytical scale. This test recorded a total of 144 channels being printed for three different microchannel designs (linear, curved, spiral along layer) and 40 prints for the helical design where microchannel also moves perpendicular to the layers. At the end of printing, we had 8 replicates of each diameter for each design. However, the size of the microchannel for the microchannel geometry which changes perpendicular to the layer has different channel size. Since, the printed results from the FDM printer shows that the accuracy of the printer not only varies with the type of the printer, but it also varies if the microchannels are along the print layers or perpendicular to the print layers. For instance, in case when the microchannels are along the printing layers the smallest achievable microchannels with the off-shelf Up printer was around 250 μm where as the geometry of the channel changes and microchannels follows the path which is perpendicular to the build layers the size of the microchannels needs to be increased to 500 μm to be able to achieve the flow across the microchannels while keeping the print settings similar to the other geometry. This study provides the practical demonstration of the same through pressure developed across the flow of the minimum possible channel size.

Moreover, the accuracy of the print also varies while printing with the Tiertime UP printer and Prusa printer. We have chosen the marlin firmware to generate the G-code which is generally the default selection for the prusa slicer. Whereas, the Tiertime UP printer has the proprietary slicing to generate the layer instructions for the printer. It can be evident from Fig. 5.6 that Tiertime UP printer showed better printing resolution for printing the inlet port of the injection (0.5 mm diameter). The slicing and subsequent printing from the Prusa printer resulted in the smaller inlet port. However, the Prusa slicer allows changes for the setting of prints and is considered to be one of the best open

source slicing software available. From the review of the sliced features, it is evident that the layers show the formation of the inlet ports but the same is not translated in prints by the Prusa i3 MK3S printer. We were unable to test the same slicing on the Tiertime UP printer as the printer does not work with Prusa slicer or any other open source slicing software. It can be inferred from the printing results that the accuracy of the Tiertime UP printer in the category of the low budget 3D printers the accuracy is better when features are printed along the printed layers, however, the slicing software does not allow myriads of parameters which can be adjusted from the open-source Prusa slicer. For our application of microchannels, the accuracy is more important and therefore, the results from the printed microchannels from Tiertime UP printer are more accurate than the Prusa printer.

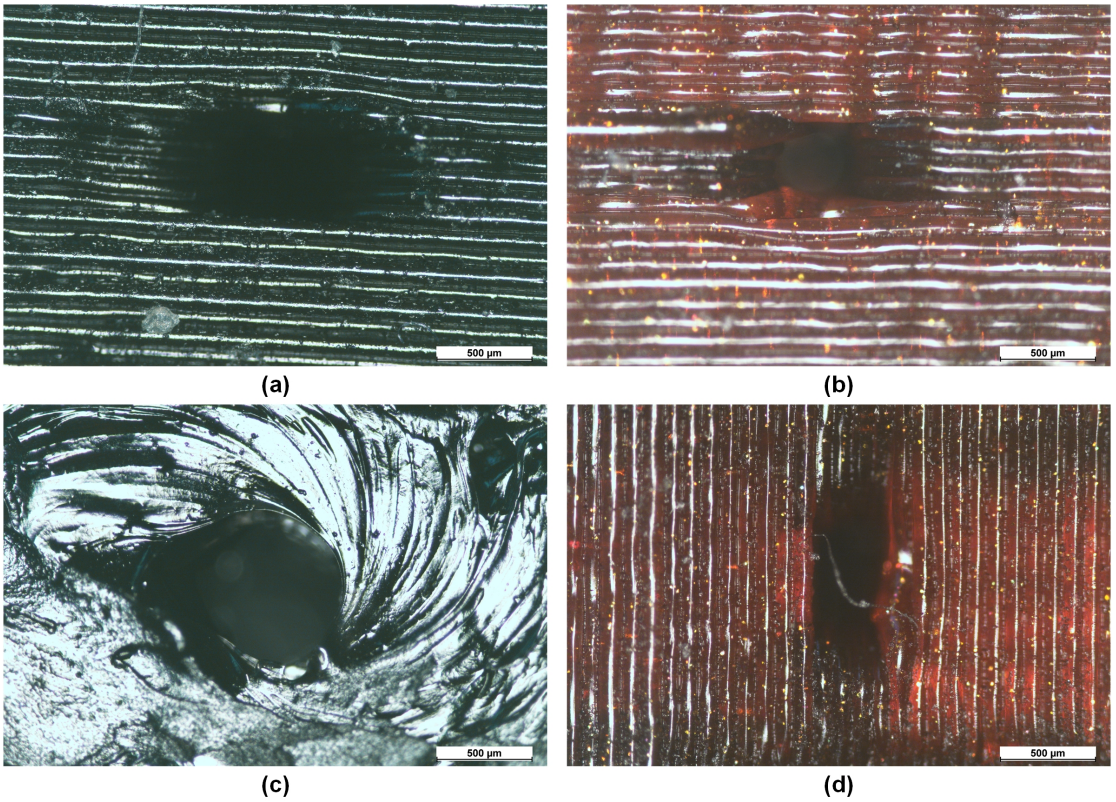

FIGURE 5.6: Comparison between printing with Prusa and UP02: a) Horizontal printing by UP02 b) Horizontal printing by Prusa c) Vertical printing by UP02, and d) Vertical printing by Prusa.

Once the printing of microchannel parts was completed, the base support structures were removed by using mechanical tools (scrapper and filament cutter). Each microchannel weight was individually recorded on Sartorius ENTRIS64-1S before applying adhesives and attachments to connect the fluidic ports. It was ensured that no channel was

damaged while removing the support. This test recorded a total of 48 accurate prints of one type of microchannels. The reason to print 8 microchannels of same diameter, per each type of microchannel, was to evaluate the effect of adsorption or leakage of fluid once the flow rate was increased. As our experiments were composed of evaluating the pressure developed in the microchannels from 5 μl/min to 40 μl/min (with a step of 5μl/min), 8 prints of each type of microchannel were necessary to be fabricated. Figure 5.7 illustrates respective graphs of linear, curved and spiral microchannels with different diameters (0.25 mm, 0.3 mm, 0.35 mm, 0.4 mm, 0.45 mm and 0.5mm). The weight variation of 0.25 mm and 0.30 mm microchannels were removed as the leakage from these microchannels was excessive even at the low flow rates. The actual weights of all the channels were plotted along the average line to represent the deviation in the weights. It is evident from the Fig. 5.7 that variation in weight is negligible among the microchannels. It was also observed that with proper scrapping and removal of support structures the printer could give an excellent precision (with variation of just 0.6%) in both microchannel designs.

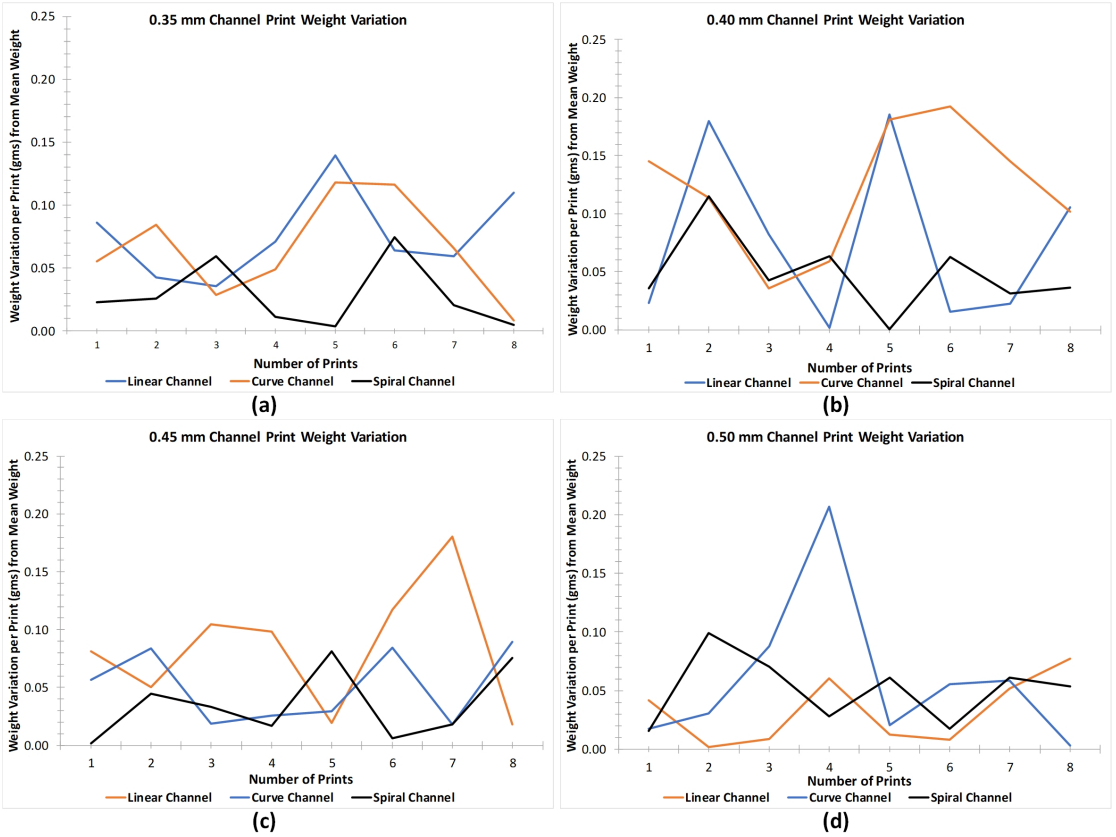

FIGURE 5.7: Weight variation of linear, curved and spiral microchannels with diameter of a) 0.35 mm, b) 0.4 mm, c) 0.45 mm, and d) 0.5 mm for 8 consecutive prints.

The graphs (Fig. 5.8 a, b, and c) explain the relationships between the flow rate and the pressure developed in the microchannel with respect to the diameter of the linear, curved, and spiral microchannel respectively. As depicted in the graphs there is a proportional relationship between the flow rate and the pressure. As the flow rate is increased the pressure developed in the channel also increases however, due to the channel length of each FDM printed microchannel and the channel routing the pressure developed is different for each type of microchannel.

It has been observed that all the microchannels with a diameter of 0.3 mm and less started to leak even at minimum flow rates. There is no leakage observed in linear and curved microchannels with a diameter of 0.4, 0.45 and 0.5 mm up to the flow rate of 40 μL/Min. This shows that the microchannel having a diameter greater than 0.4 mm can be used for various microfluidic drug delivery applications under a controlled flowrate. However, in the linear and curved microchannel with a diameter of 0.35 mm, no leakage has been observed until the developed pressure reached to 4,000 Pa. Above this pressure, the body of the microchannels in both the designs started to leak from the top and bottom side near the inlet port for a diameter of 0.35 mm microchannel. In the case of spiral microchannels, leakage has been observed in 0.35 mm channel diameter, but the inception of the leakage started at a lower flow rate when compared with the linear and curved channel. Moreover, it is observed that more pressure is developed across the channels of the curved and spiral microchannels when compared to linear microchannel at the same flow rate. This is due to the constriction in the microchannel due to the geometrical changes in each of the printed layer as the shape of the microchannel was varying along the printed lines. It is therefore, established that the pressure above 4,000 Pa in the fluidic channel can result in the leakage from the FDM printed parts for straight, curved and spiral microchannels for microchannels sizes less than 0.4 mm. Table 5.4 provides the values of pressure developed against the applied flow rate in the microchannels where the cells highlighted in red indicate the flow rates at which the microchannels started to leak.

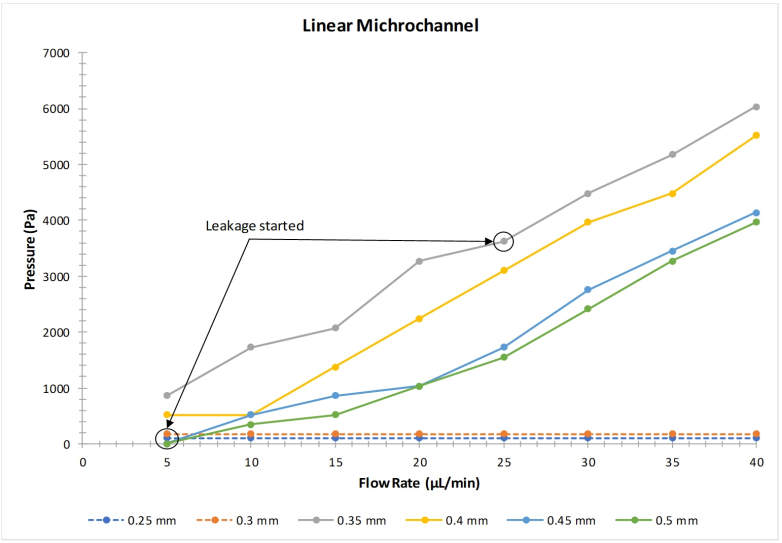

(a)

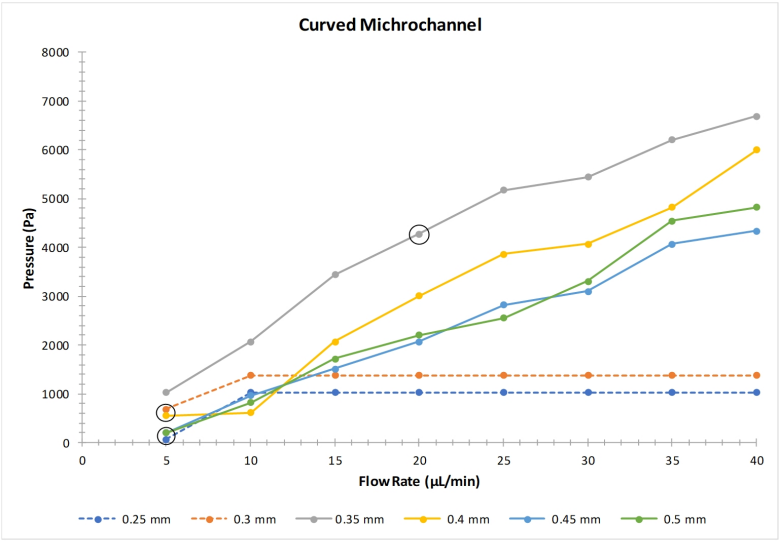

(b)

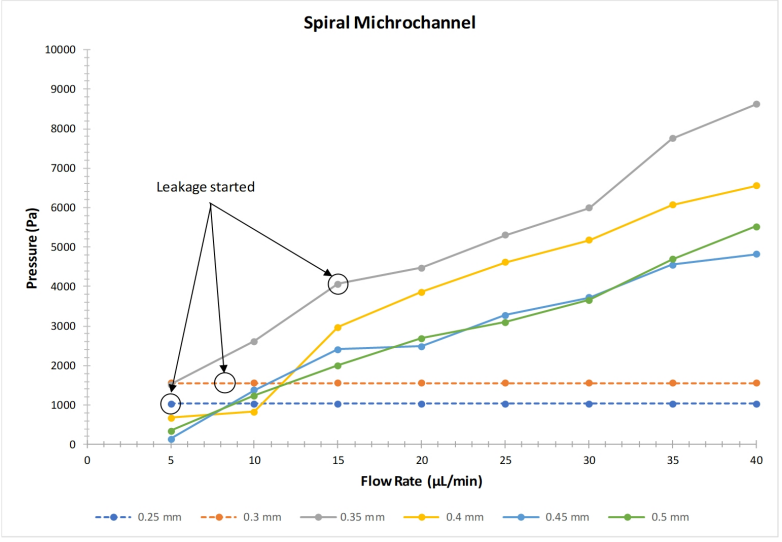

(c)

FIGURE 5.8: Change in flow rate vs developed pressure at the inlet port of a) linear microchannel, b) curved microchannel and c) spiral microchannel.

TABLE 5.4: Pressure developed in microchannels vs. flow rate. The cells highlighted in red indicate the pressure at which the microchannels started to leak.

Microchannel Design	**Flow rate (μl/min)**	**Pressure (Pa) Microchannel Size (mm)**			
		0.35	**0.4**	**0.45**	**0.5**
Linear	5	862	517	0	0
	10	1,724	517	517	345
	15	2,068	1,379	862	517
	20	3,275	2,241	1,034	1,034
	25	**3,620**	3,103	1,724	1,551
	30	**4,482**	3,964	2,758	2,413
	35	**5,171**	**4,482**	3,447	3,275
	40	**6,033**	**5,516**	4,137	3,964
Curve	5	1,034	552	207	207
	10	2,068	621	965	827
	15	3,447	2,068	1,517	1,724
	20	**4,275**	3,006	2,068	2,206
	25	**5,171**	3,861	2,827	2,551
	30	**5,447**	4,068	3,103	3,309
	35	**6,205**	**4,826**	4,068	4,551
	40	**6,688**	**5,998**	4,344	4,826
Spiral	5	1,517	676	138	345
	10	2,620	827	1,379	1,241
	15	**4,068**	2,965	2,413	1,999
	20	**4,482**	3,861	2,482	2,689
	25	**5,309**	4,619	3,275	3,103
	30	**5,998**	**5,171**	3,723	3,654
	35	**7,757**	**6,067**	4,551	4,688
	40	**8,618**	**6,550**	**4,826**	5,516

As discussed earlier the helical microchannel was unable to be printed without the constriction due to the complex profile, therefore the pressure profile of the helical microchannel was not discussed along with the other profiles. We were able to get the flow from the helical profile for microchannel diameter of 500 μm or above. Six profiles with

the increment of 100 μm were printed till 1 mm microchannel for the helical profile. The pressure developed in the helical profile was much greater than the other profiles; though, the size of the microchannel was also greater than the other profiles. It was observed that the helical profile resulted in about an average of 2.45 times the pressure generated by the similar size microchannel for spiral profile when compared for the 500 μm size microchannel. This shows that the mapping of the irregular or complex geometrical shapes cannot be exactly replicated during the printing process by FDM printers (Fig. 5.9).

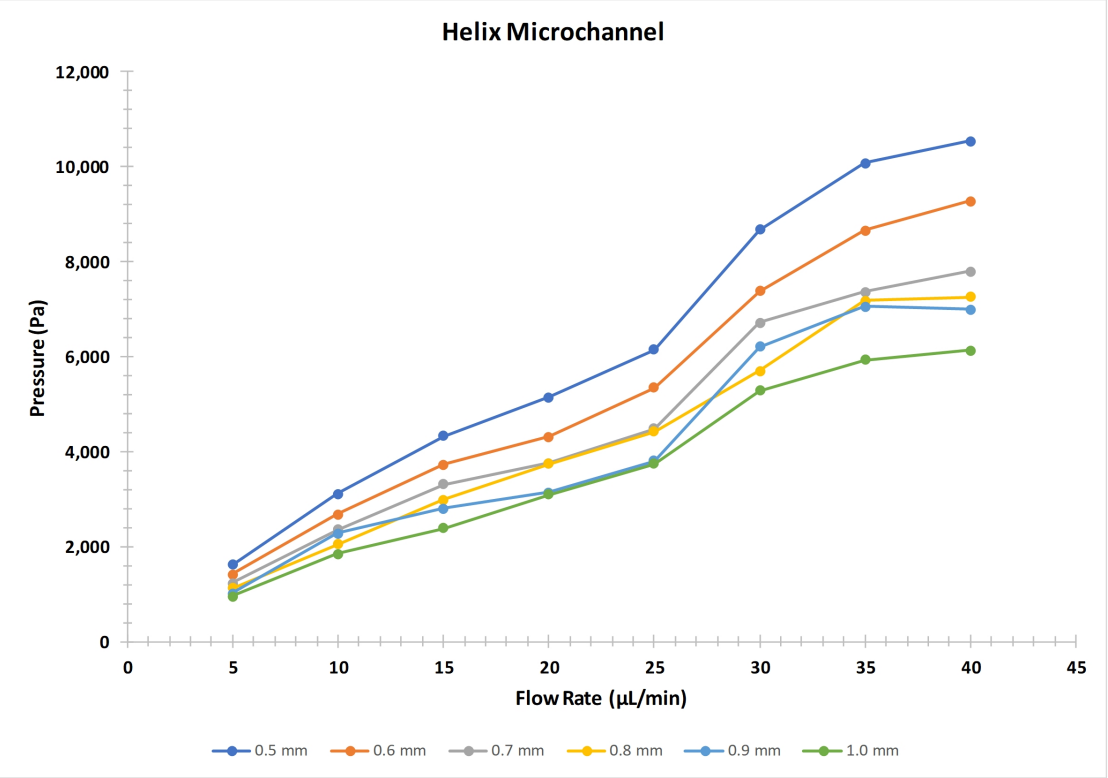

FIGURE 5.9: Helical microchannel pressure profile with respect to flow rate.

The mapping of the geometrical profile can also be confirmed by the optical microscopic images of the two microchannel holes when the orientation of the printed part is changed during the printing process. Fig. 5.6 shows the optical image of the 500 μm size microchannel when oriented horizontally and vertically during the FDM printing process. The optical image of the printed 500 μm size microchannel corroborates that the internal feature cannot be mapped exactly as designed in the CAD software and due to the same the helical profile offers more constriction in the flow of liquid when compared with the other profiles.

Since, the FDM parts contains voids in between the printed layers therefore, it is natural for a microfluidic application that the printed part may result in retention of liquid during and after the application of flow across the channel. For the same purpose water retention analysis in the microchannel was studied by weight analysis. Once the pressure readings are taken by varying the flowrate through the syringe pump, the inlet port of the microchannel was subjected to the application of compressed air so to remove the access water from the microchannel. After removing the excess water, the weight of each microchannel was noted down before and after water flow through the microchannel and the difference (weight variation) between them was calculated. After the experiment, a jet of compressed air was passed through the microchannel to exclude the weight of the stagnant water inside the channel. The weight analysis for each of the design can be observed in the graphs as shown in Fig. 5.10. In each design, the trend shows a linear increase in the weight variation with an increase in the flow rate at all the diameter sizes. Minimum weight variation has been found in the linear microchannel whereas, the maximum variation can be observed in the spiral design. Average weight variation is decreasing with an increase in the diameter size.

Weight analysis of the helical microchannel is done separately as the size of the microchannels were much bigger than the microchannel printed with different profiles in the preceding section. This type of the microchannel changes its profile in the Z-plane during the FDM printing if we consider the movement of the nozzle for a specific layer in XY plane. The result of the weight analysis of the helical microchannel shows that it is more susceptible to retain water when compared to the other profile. This is due to the application of more pressure to generate the flow. Also, there are more inter layer voids which enhances the seepage of water between the voids. Fig. 5.11 shows the water retention in the helical microchannel profile at various flowrates and the variation of weight of the similar size microchannel for consecutive FDM printed parts. The retention of water is proportional to the applied flowrate since the weight of the parts increases with the increase of flowrate. However, above 900 μm microchannel sizes in out-of-plane geometry, the retention follows the similar profile when compared to smaller microchannel sizes of in-plane geometry. This shows that the constriction in the microchannel for complex out-of-plane geometrical profile above 900 μm in diameter is low as the slicing software was able to map the printed layers with good accuracy when the ratio of layer thickness to the microchannel diameter is 1:10 (in our case we used layer thickness of

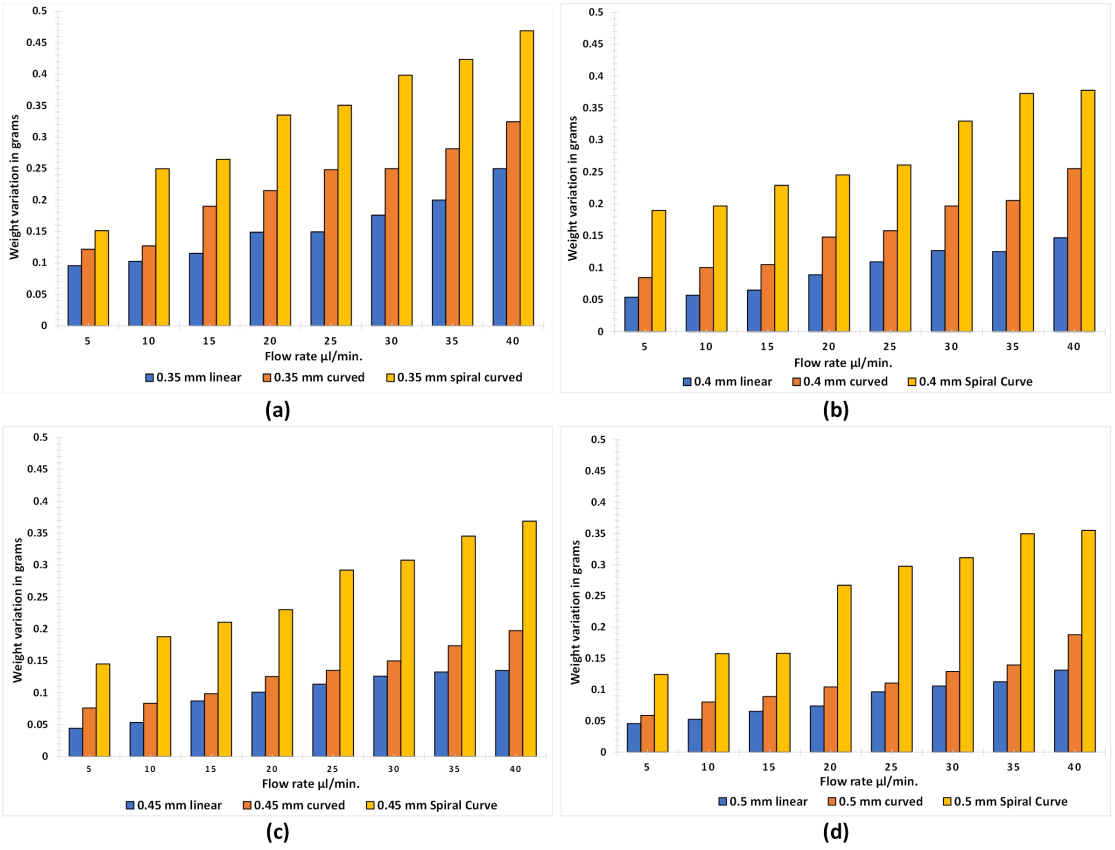

FIGURE 5.10: Weight analysis of linear, curved, and spiral microchannels with diameter size of a) 0.35 mm, b) 0.4 mm, c) 0.45 mm, and d) 0.5 mm.

100 μm for all the microfluidic channel) or greater for complex out-of-plane geometry. This is due to the constant backlash speed of the printing nozzle with respect to the rapid profile changes in the out-of-plane geometry of the microfluidic channel. And such changes cannot be mapped exactly by varying the backlash speed in real-time for the two low-cost FDM printer through their respective slicing software used in this study. Hence, we can establish that the complex out-of-plane geometry not only generates more pressure for similar applied flowrate when compared to in-plane geometry microfluidic channel, but it is also difficult for the slicing software to exactly replicate the 3D modelled microfluidic profile. It is proposed that the further improvement of the microchannel constriction can be reduced by decreasing the layer thickness however, such can lead to drastic increase in the printing time and eventually increases the cost of fabricated part rendering the FDM printing less feasible for fabricating out-of-plane microchannel profiles having diameter less than 500 μm in size.

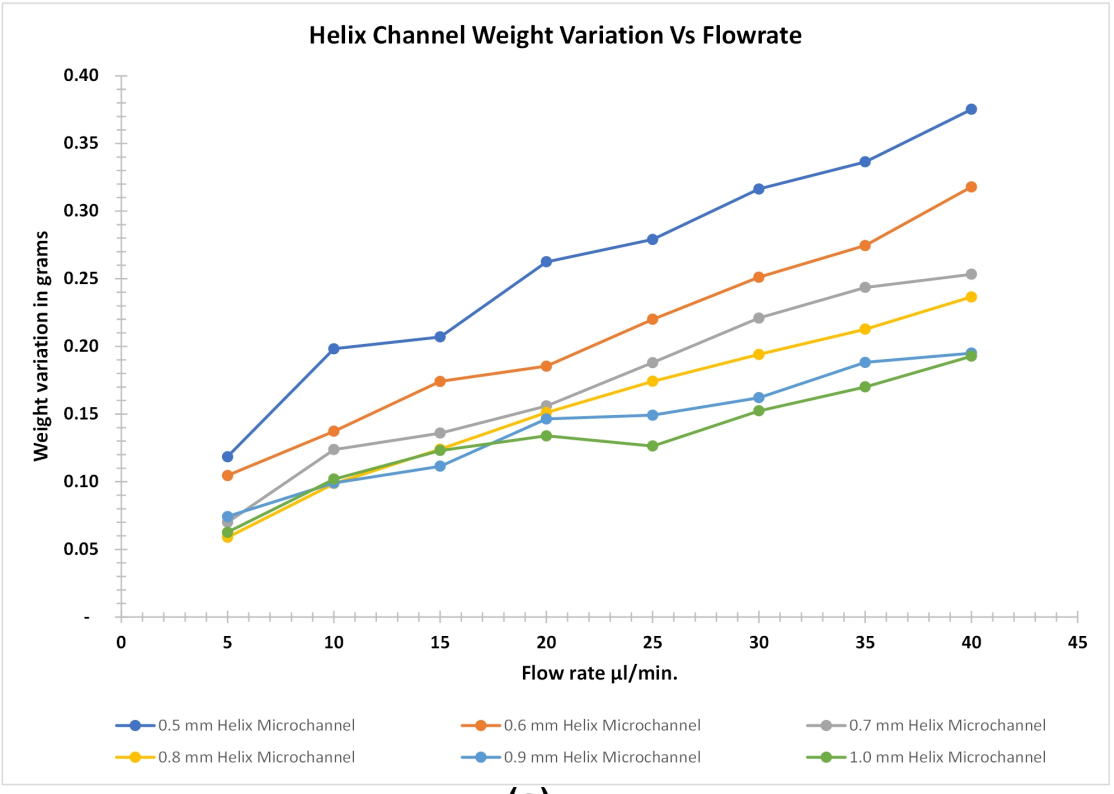

(a)

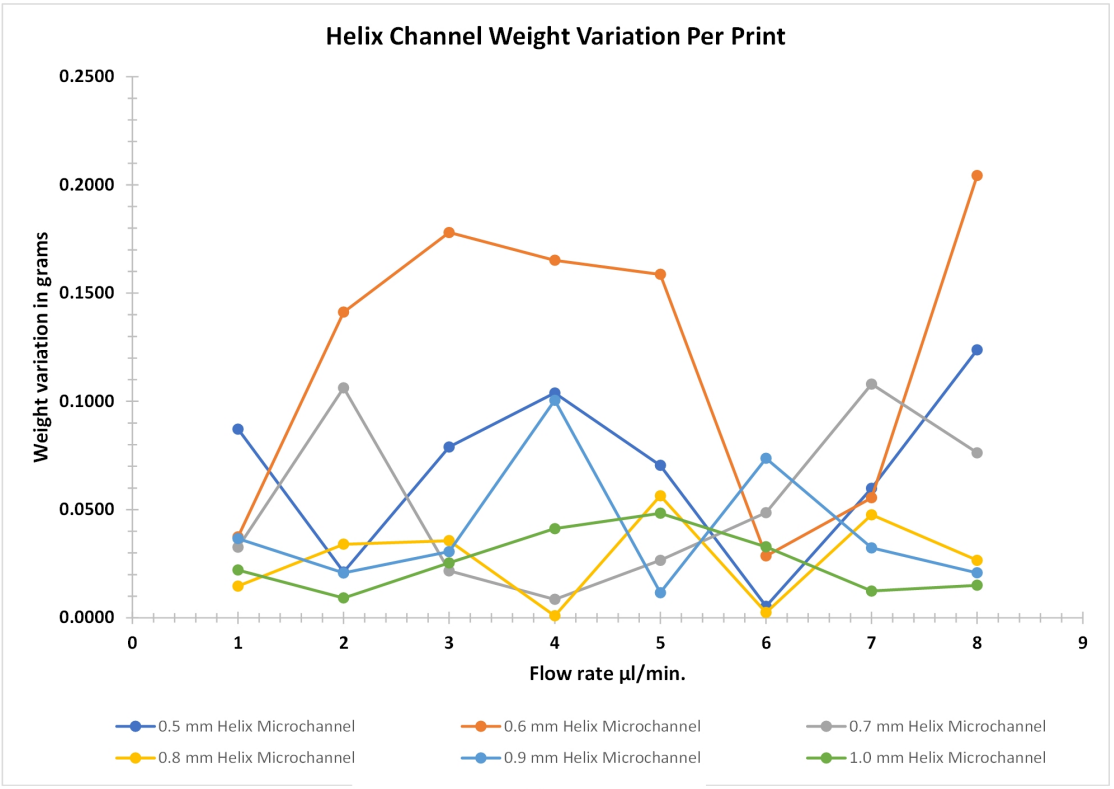

(b)

FIGURE 5.11: Weight analysis of helical microchannel. (a) Water retention with respect to flow rate of diameter size of 500 μm to 1 mm microchannel with an increment of 100 μm (b) Weight variation per printing of FDM parts for helical microchannel from 500 μm to 1 mm microholes.

To observe the effect of acetone cleaning/treatment on the inner surface of the microchannel, pre and post-treatment weight analysis was carried out. Also, the post-treatment leakage through the microchannels was studied. The pre and post-treatment weight of the microchannels were normalised and then plotted as shown in Fig. 5.12. It has been observed that the post-treatment weight of the channels is lesser than the pre-treatment weight. It has also been found that the weight variation is less when the diameter is small and the flow rate is low, and the variation is more when the diameter is large, and the flow rate is high. This means that the cleaning of FDM channel with acetone involves the chemical reaction between additives in PLA and acetone which results in the weight loss of the printed FDM parts suggesting that the PLA filament from Tiertime is not a virgin or pure PLA material. As the flowrate of the acetone is increased the loss in the weight is greater than the printed channel subjected to lower flowrates.

When water was passed through the acetone cleaned/treated microchannels, the leakage was detected from the microchannels which were previously observed to be good carriers of water at every flow rate (0.35, 0.4, 0.45, and 0.5 mm). This means that the chemical reaction between the additives in PLA and acetone was unable to prevent the leakage of water from the body of the microchannel.

5.5 Conclusion

In this paper, we demonstrated the possibility to fabricate the internal features of the microfluidic device using FDM printer by optimizing the printer's parameters. We successfully printed the linear, curved and spiral microchannels with the diameter less than 0.5 mm where the path of the microchannel was along the print layer. The work also demonstrates the limitation of low budget FDM printer fabrication of microchannels where the path of the microchannel follows perpendicular or spline geometry with respect to the print layer. Print resolutions of two different FDM printers were compared and assessed for the suitability of the microchannel printing. One of the selected FDM printer can be used with the widely available open-source slicer and other had the proprietary slicer. The results showed that the low budget FDM printer can print the inline or parallel geometry with better print accuracy and can be used for such type of microchannel channels. However, when the geometry is complex and is not along the

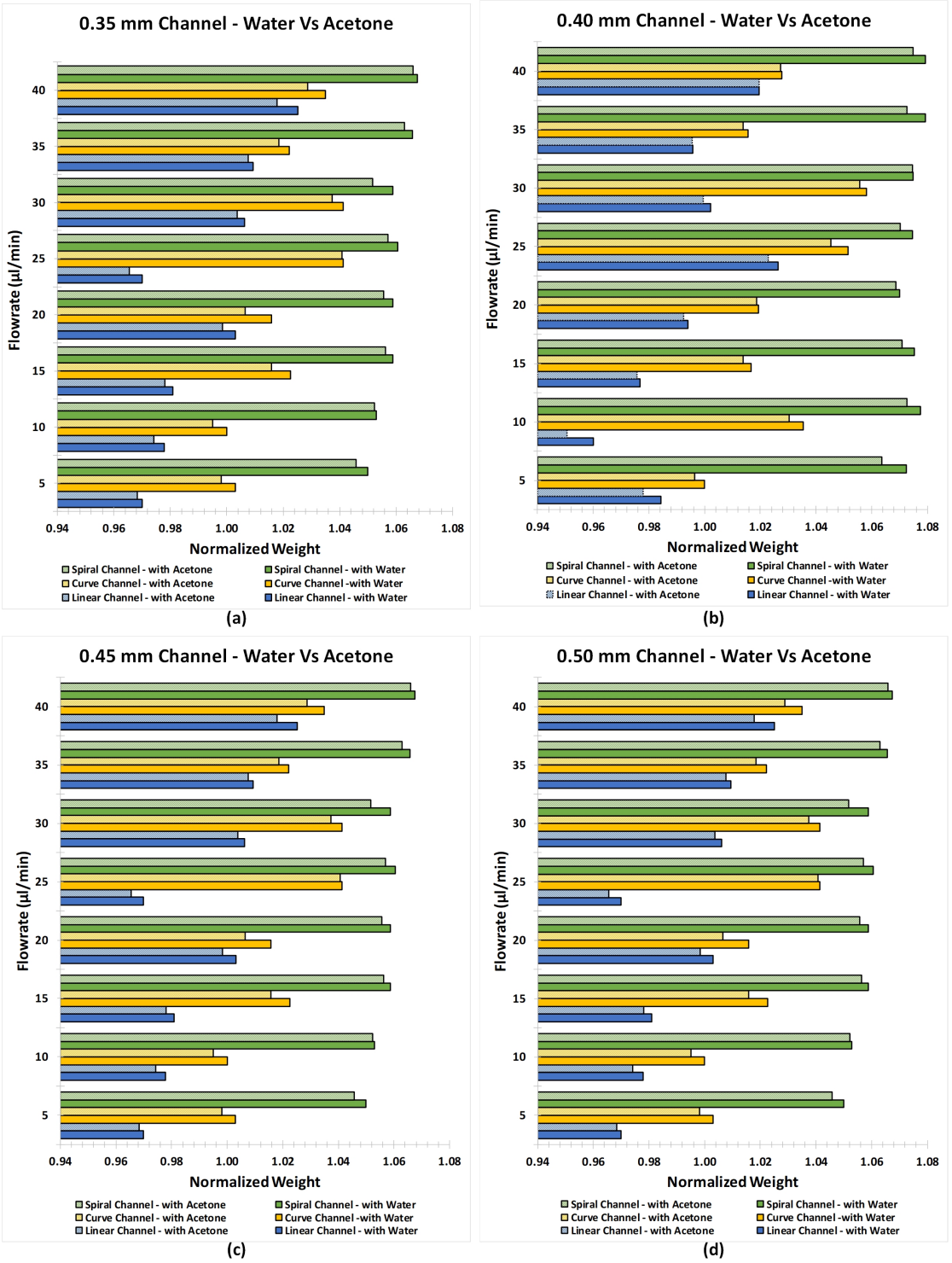

FIGURE 5.12: Post-treatment normalized weight analysis of linear, curved and spiral microchannel with diameter sizes of a) 0.35 mm, b) 0.4 mm, c) 0.45 mm, and d) 0.5 mm.

print layers the size of the microchannels needs to be increased for millifluidic application. Moreover, the experimental results illustrated the correlation of internal feature (microchannel diameter) with the flow rate and also reflects the maximum pressure of the fluid to which microfluidic device can withstand. Also, it has been observed that water retention in both the designs increased with increasing the diameter size. However, it has been found that the more water retention occurred in the spiral microchannels when compared with the linear and curved microchannels. Furthermore, inner surface cleaning/treatment of the microchannel with acetone was also carried out at different flow rates. After the acetone treatment, it was expected that the internal voids in the channels would be sealed, and better results would be observed. However, the results of the porosity test after acetone treatment didn't support this idea. Thin-walled microchannel was assumed to be the reason for failure in this case. Weight variation in the microchannels was discussed after being treated by acetone. The accuracy of the printer was found to be excellent with just 0.6% variation in both designs.

Chapter 6

Conclusion and Future Outlook

6.1 Conclusion

The work presented in this thesis has produced two peer reviewed conference papers and four Journal Articles (two of which have already been published in reputable journals). It is pertinent to mention here that each chapter of the thesis has its respective conclusion section. However, an overall brief summary of the conclusions is presented below:

- Methods other than decreasing the anchoring diameter of printing ink has been explored by fabricating four different EHD printheads. The results showed that the inkjet printhead resolution could be improved by using a primary nozzle to transport the ink/fluid and secondary nozzle for the ejection of the droplet. The aligned aperture coaxial printhead used to transport and dispense the liquid from nozzle has not only improved the resolution but also provided the opportunity for various ink materials—such as metallic, organic, and biomaterials with a wider physical properties (viscosity, surface tension and particle size). All the necessary items for fabricating the proposed printhead are commercially available and this offers a cost-effective way of fabricating the high resolution EHD printhead.

- The nozzle tip distance from the beveled opening of the nozzle also plays a significant role in achieving the improved printed resolution. Shorter distance of nozzle bevel to the tip provides better resolution as seen in the case of spinal needle when compared with the hypodermic aligned aperture EHD printhead.

- The resolution improvement for shorter ink dilation distance is of the order of 3 times in case of spinal needle (2 μm approx.) when compared with hypodermic needle (6 μm approx.) at the similar flowrate, standoff distance and applied voltage during the EHD printing of the same ink.

- Our aligned aperture design based on the spinal needle type D printhead resulted in the smallest resolution of 1.85 μm at the optimal applied voltage and flowrate parameters. The achieved ratio of the proposed printhead nozzle diameter to the printed lines was around 270 times.

- Laser ablation process from a commercial CO_2 laser cutting machine can be used to fabricate microchannels suitable for screen printed transduction electrode. It was observed that for a curved region the XY-stage of laser interpolates successive points on the substrate. During this interpolation the speed of the laser is decreased which results in wider ablated cross-section due to the longer exposure of laser. On average increase of width between the straight and curved profile/geometry is around 30%.

- Various laser ablated transduction schemes for humidity sensing resulted in sensitivities ranging from 0.13 to 2.37 pF/%RH in general. The sensor showed a fast response time of less than 10 seconds for all the fabricated transduction schemes under the ambient testing conditions. The overall process is repeatable, scalable and cost-effective method to fabricate and evaluate the sensing parameters and performance of various transduction geometries.

- During the EHD printing the conductive ink is prone to cracking. The reason of cracking is attributed to the greater volume being dispensed during the conejet formation at the centre of the printed lines. Higher dispensed volume at the centre of printed lines compared to ink volume at the edges creates stresses during the thermal curing of the ink. The developed stresses and coefficient of expansion of the substrate resulted in cracking during the thermal curing of EHD printed features.

- The development of the cracks in EHD printing can be avoided by incorporating the conductive particles similar or bigger than the width of the cracks. The longer particles embedded in the composite ink acts as a filler material between the cracks and retained the conductivity of the printed features.

- Sheet resistance of the ink composite also depends on the concentration of the filler material in the composite ink. Higher concentration of the filler material results in better conductivity.

- To expand the application of sensors a microfluidic device based on the fused deposition modelling seems feasible. However, the FDM printed microfluidic device is prone to leakages due to presence of voids during the printing of extruded material.

- The leakages in the FDM printed microfluidic device depends upon the developed pressure in the microfluidic channel. Straight microchannel profiles along the extruded plane offers less pressure gradient when compared to the curved and non-planar microchannels at the same flowrate.

- Pressure gradient above 4000 Pa in the microchannels are susceptible to leakages when no pre and post processing in the FDM printed parts is employed.

6.2 Future Outlook

The work presented in this thesis provides numerous opportunities in the development of printed sensors such as improvement of printing resolution, role of transduction geometries for sensing applications, susceptibility of crack development in EHD printing and possible integration of sensing device in FDM printed microfluidic device for lab scale deployment in real world environment. It is envisaged that the results from the work presented in this thesis can be extended through following applications in future

- Challenges of EHD printing on non-planar substrate having varying thickness. Since, the standoff distance between the counter electrode is changed for a non-planar substrate profile which can results in varying width of deposited material. A real-time 3D profiling can be used to correlate the changes in the applied voltage to be compensated for varying cross section of non-planar substrate for uniform deposition of ink.

- Applications in the area of flexible electronics and soft robotics can be realized by further exploring the proposed EHD printing technique in our work. Ink compositions and additives which prevents crack development during the posting printing

especially for stretchable and flexible electronics will be highly desirable for future sensing applications.

- Generally silver and gold are expensive material. Conductive inks based on these metals are expensive to synthesize. However, to lower the cost of the ink, cheaper metals such as copper can be used in the conductive ink. Copper is more susceptible to oxidation. Two methods can be used to lower or eliminate the oxidation. First is to coat the copper particles with metallic particles which are less susceptible to oxidation such as nickel, zinc, lead and aluminium can be used and compatible inks can be use for EHD printing.

  Furthermore, an alloy of silver or copper with other metals can be formed which reduces the oxidation of metallic particles in the ink. Since. the rate of oxidation decreased to a greater extent with change in the crystal structure of metals. Change in crystal structure with the addition of other metals to form an alloy seems to be promising approach. Explorations in this area can provide conductive ink and their respective products at a cheaper cost.

Appendix A

List of Publications

A.1 Journal Publications

1. Rehmani, M.A.A., Arif, K.M. High resolution electrohydrodynamic printing of conductive ink with an aligned aperture coaxial printhead. Int J Adv Manuf Technol 115, 2785–2800 (2021).

   doi:https://doi.org/10.1007/s00170-021-07075-6

2. Rehmani, M.A.A.; Jaywant, S.A.; Arif, K.M. Study of Microchannels Fabricated Using Desktop Fused Deposition Modeling Systems. Micromachines 2021, 12, 14.

   https://doi.org/10.3390/mi12010014

3. Rehmani, M.A.A., Mathews, S, Arif, K.M. Silver nanoparticle and diethylene glycol monobutyl ether modified conductive ink for high conductivity electrohydrodynamic printing. MDPI Polymers. Prepared/Submitted.

4. Rehmani, M.A.A., Lal, K, Shaukat, A, Arif, K.M. Laser ablation assisted micropatterned screen printed transduction electrodes for sensing applications. Nature Scientific Reports. Prepared/Submitted.

A.2 Conference Publications

1. M. A. A. Rehmani and K. M. Arif, "Capacitive Transduction Schemes for Environmental Humidity Sensors," 2019 13th International Conference on Sensing Technology (ICST), 2019, pp. 1-5

   doi:10.1109/ICST46873.2019.9047700

2. Jaywant, Swapna A., Rehmani, A., and Nayak, T., and Khalid Mahmood Arif. "Fabrication and Characterization of 3D Printed Microfuidics." Proceedings of Mechatronics and Machine Vision in Practice Conference, M2VIP 2019.

   https://doi.org/10.1007/978-3-030-43703-9_10

3. Muhammad Asif Ali Rehmani, Khalid Arif, Catherine Whitby and Xiaowen Yuan. "Synthesis of Conductive Ink for Printed Sensors." A Poster in The Third National Conference for Innovation in Manufacturing, Design and Entrepreneurship, MaD 2019.

4. Muhammad Asif Ali Rehmani, and Khalid Arif. "Laser Micromachined Templating for Fabrication of Printed Sensors." A Poster in Second International Symposium on Advanced Materials, Manufacturing Processes and Devices (MMPD) 2019.

5. Muhammad Asif Ali Rehmani, Khalid Arif and Xiaowen Yuan. "Effecr of Electrode Geometrical Structure on Signal Transduction in Indoor Air Quality Sensors." A Poster in NZ Product Accelerator 2018.

The International Journal of Advanced Manufacturing Technology (2021) 115:2785–2800
https://doi.org/10.1007/s00170-021-07075-6

ORIGINAL ARTICLE

High resolution electrohydrodynamic printing of conductive ink with an aligned aperture coaxial printhead

Muhammad Asif Ali Rehmani[1] · Khalid Mahmood Arif[1]

Received: 23 July 2020 / Accepted: 12 April 2021 / Published online: 29 May 2021

Abstract
Electrohydrodynamic (EHD) printing is a promising inkjet technique to generate smaller droplet sizes due to the formation of a Taylor cone. However, the process is intricate and involves the fabrication of a printhead having a smaller nozzle diameter. Notable examples are present in the literature regarding printing through EHD but the underlying phenomenon which is responsible for generating the smaller droplet is obscure. In this work, we present a methodology which highlights the importance of nozzle shape which can govern smaller droplets even with a large head diameter. The work achieves a resolution of less than 2 μm by fabricating the inkjet head using simple techniques and off-the-shelf inexpensive needles of nozzle diameter ranging from 500 μm to 250 μm. The study of various nozzle profiles resulted in a printed resolution which is 50 times smaller than the nozzle diameter. Moreover, the study also highlights the importance of the wetting area profile of the nozzle and explains the role of printhead design which facilitates fine resolution printing of conductive tracks which until now seemed to be obscure.

Keywords Electrohydrodynamic printing · Printhead design · Conductive ink · Flexible electronics · Inkjet printing systems

1 Introduction

High resolution conductive printing without the need of a cleanroom and conventional photolithography process which requires fabrication of mask and subsequent etching is highly desirable. Microscale printing with on-the-fly customization for small batch fabrication of printed electronics and flexible sensors development has received tremendous attention [1–4].

Primarily, the key printing technologies can be divided into contact and contact-less printing [5, 6]. In contact printing the impression of roll generates the features on the substrate. Depending on the process whether the impression engraves or penetrates the ink on the substrate the process can be differentiated by physical phenomenon responsible for generating tracks or features in the substrate. Screen, offset, flexography, gravure and pad printing are examples of contact printing, whereas aerosol, thermal, piezoelectric, electrohydrodynamic and acoustic inkjet printing are the prominent contactless inkjet printing methods. Contact printing technology is widely used in the paper industry and print media. The advantage of these printing methods is their high throughput with accuracies up to 50 μm, with gravure printing reaching higher resolution and high aspect ratios [7]. Almost all the contact printing methods utilize the roll-to-roll technology to transfer the base pattern on the substrate. But registration control, in the case of tight tolerances, can be a challenge. High velocity and pressure on the substrate in contact printing cause the flexible substrate to stretch, resulting in the design of complex registration algorithms [8–11] for aligning the next feature printing on the substrate. The cost of product fabricated through contact printing is cheaper per unit than the contact-less printing method due to high throughput for large production batches [12–15]. However, for small production batches, the cost per unit is much higher than contact-less printing [16, 17] and incorporating design changes requires changes in the impression features of roller which is often expensive and complex. Moreover, the overall printing process produces ink wastage at various stages of printing. Inkjet printing has a certain advantage in a printed electronic application. Not only is it a contact-less printing method but it also has a fabrication process which allows the pattern printing to be in a discrete or continuous manner depending

✉ Khalid Mahmood Arif
k.arif@massey.ac.nz

[1] Department of Mechanical and Electrical Engineering, SF & AT, Massey University, Auckland 0632, New Zealand

FIGURE A.1: A paper published in The International Journal of Advanced Manufacturing Technology, Springer, 2021

micromachines

MDPI

Article

Study of Microchannels Fabricated Using Desktop Fused Deposition Modeling Systems

Muhammad Asif Ali Rehmani, Swapna A. Jaywant and Khalid Mahmood Arif *

Department of Mechanical and Electrical Engineering, SF&AT, Massey University, Auckland 0632, New Zealand; m.a.a.rehmani@massey.ac.nz (M.A.A.R.); s.jaywant@massey.ac.nz (S.A.J.)
* Correspondence: K.Arif@massey.ac.nz; Tel.: +64-9-414-0800

Abstract: Microfluidic devices are used to transfer small quantities of liquid through micro-scale channels. Conventionally, these devices are fabricated using techniques such as soft-lithography, paper microfluidics, micromachining, injection moulding, etc. The advancement in modern additive manufacturing methods is making three dimensional printing (3DP) a promising platform for the fabrication of microfluidic devices. Particularly, the availability of low-cost desktop 3D printers can produce inexpensive microfluidic devices in fast turnaround times. In this paper, we explore fused deposition modelling (FDM) to print non-transparent and closed internal micro features of in-plane microchannels (i.e., linear, curved and spiral channel profiles) and varying cross-section microchannels in the build direction (i.e., helical microchannel). The study provides a comparison of the minimum possible diameter size, the maximum possible fluid flow-rate without leakage, and absorption through the straight, curved, spiral and helical microchannels along with the printing accuracy of the FDM process for two low-cost desktop printers. Moreover, we highlight the geometry dependent printing issues of microchannels, pressure developed in the microchannels for complex geometry and establish that the profiles in which flowrate generates 4000 Pa are susceptible to leakages when no pre or post processing in the FDM printed parts is employed.

Keywords: additive manufacturing; microfluidics; microchannel; curved microchannel; fused deposition modelling; 3d printing

check for updates

Citation: Rehmani, M.A.A.; Jaywant, S.A.; Arif, K.M. Study of Microchannels Fabricated Using Desktop Fused Deposition Modeling Systems. *Micromachines* **2021**, *12*, 14. http://dx.doi.org/10.3390/mi12010014

Received: 22 October 2020
Accepted: 16 December 2020
Published: 25 December 2020

1. Introduction

Microfluidics, the science and technology of manipulating fluids at micro to millilitre scale through internal features, has been applied in various applications such as point-of-care diagnostic tools, therapeutic devices, and air and water quality monitoring methods [1–6]. Currently, popular manufacturing techniques for producing microfluidic devices include soft lithography [7], paper microfluidics [8,9], micromachining [10], injection moulding [11], hydrid paper based open channel microfluidics [12], etc. Soft-lithography using polydimethylsiloxane (PDMS) micro-moulding is widely used method as PDMS is optically transparent, chemically inert, and gas permeable material with low-surface energy [13]. However, most of these methods are expensive, time-consuming, require multi-step processing in a cleanroom. Additionally, it is quite difficult to change device design [14]. Recently, 3-dimensional printing (3DP) is rapidly gaining attention in the field of microfluidics. The prominent fabrication techniques for microfluidics are fused deposition modelling (FDM), selective laser sintering (SLS), stereolithography (SLA), Xurography and inkjet printing [15–19]. These methods have various advantages like automated fabrication, cost-effectiveness, availability of a wide range of materials, single-step procedure, etc. [13,20–22]. Moreover, 3DP does not require a photomask, photoresist, or access to a cleanroom. This allows a major reduction in the material cost, creates the possibility of mass manufacturing, and saves significant development time [13].

The literature shows that 3DP methods such as FDM [1,23–27], SLA [28,29], and inkjet printing [30] have been used in the field of microfluidics. Symes et al. [2] printed the

FIGURE A.2: A paper published in Micromachines, MDPI 2021

2019 Thirteenth International Conference on Sensing Technology (ICST)

Capacitive Transduction Schemes for Environmental Humidity Sensors

1st Muhammad Asif Ali Rehmani
Department of Mechanical and Electrical Engineering
Massey University
Auckland, New Zealand
m.a.a.rehmani@massey.ac.nz

2nd Dr. Khalid Mahmood Arif
Department of Mechanical and Electrical Engineering
Massey University
Auckland, New Zealand
K.Arif@massey.ac.nz

***Abstract*—In this work various capacitive transduction schemes have been evaluated by performing numerical solution using COMSOL Multiphysics. Seven different schemes were evaluated by keeping the printed sensor finger widths up to 200μm and the same interspacing between these electrodes. The geometrical structure of transduction electrodes of the sensor directly relates to the sensitivity of the sensor and its performance. Our findings suggest that customized triangular arrow electrode configuration provides high transduction signals and is suitable for many gas sensing applications and environmental sensors.**

***Index Terms*—Capacitive Sensor; Environmental Sensor; Interdigitated Electrodes; Transduction Scheme; Electrochemical Sensor**

I. Introduction

Printed capacitive structures to sense the electrochemical behaviour of the analyte are widely used for environmental sensors. The advantage of capacitive sensors is that they consume low energy, are less susceptible to radiation, have good sensitivity and provide fast response [1]–[6]. The most common capacitive designs are parallel plate (PP) electrodes separated by a dielectric layer [7], [8]. Thin film interdigitated electrodes (IDEs) are one of the most widely used schemes due to simplicity of design and ease of analytical and numerical modelling [9]–[12].

The basic component of an electrochemical sensor are the sensing layer, transduction electrodes and the substrate. The sensing layer attracts the analyte by undergoing chemiadsorption which generates the electric signal sensed by the readout circuit. The rate of adsorption dictates the response of the sensor where desorption cycle is attributed to the recovery of the sensing layer. The sensing layer can be a single layer, bilayer or composite layer. Whereas the substrate for flexible printed sensors (and electronics) can be polyethylene terephthalate, polyamide, polyethylene naphthalate, polycarbonate, and polystyrene polymer-based substrate. A typical sensor layout is presented in Fig. 1.

Whereas, transduction electrodes can be of different shape or geometry such as indigitated or meander electrodes which provide enhanced signal for capacitive and resistive sensing schemes [13] as shown in Fig. 2. Capacitive sensing has been commonly used for humidity sensors with reference capacitors so to mitigate the drift due to thermal interference. However, these devices are complex due to the inclusion of additional components [14], [15]. Other methods such as heating of substrate are also used to shorten or augment the recovery of such sensors [16]. Nevertheless, with proper selection of sensing layers, electrode geometry and suitable substrate a sensitive and highly responsive environmental sensor can be fabricated which operates at room temperature with low or minimal sensor drift and without needing additional components [17], [18].

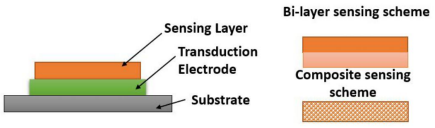

Fig. 1. Typical sensing mechanism

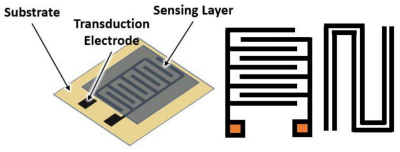

Fig. 2. Geometric shapes of transduction electrodes

Environmental humidity sensors are also synthesized by producing the transduction electrodes on the polyamide substrate without the need of sensing layer. Polyamide substrate is susceptible to change its dielectric propoerties at varying humidity levels. Moreover, polyamide has high glass transition temperature of above 250°C which makes it one of the suitable substrate for inkjet printing applications. Physical properties of various flexible substrate are mentioned in TABLE I [19].

978-1-7281-4807-6/19/$31.00 ©2019 IEEE

FIGURE A.3: A paper published in ICST-2019 Conference proceedings

Fabrication and Characterization of 3D Printed Microfluidics

Swapna A. Jaywant, Muhammad Asif Ali Rehmani, Tanmay Nayak, and Khalid Mehmood

1 Introduction

Microfluidics is an integral part of lab-on-chip (LOC) and a micro total analysis system (μTAS) and sometimes also referred by these names. The field of microfluidics has proven high potential in many applications ranging from environmental assays to clinical analyses. This includes various point-of-care diagnostic tools, therapeutic devices, and water quality monitoring techniques and so on [5, 6, 8, 10, 12, 14, 15]. Several techniques are available today for manufacturing of microfluidic channels such as injection moulding, softlithography and paper microfluidics [1]. Among many methods, softlithography technique using polydimethylsiloxane (PDMS) micro-moulding is a highly popular method [2, 7]. Microfluidics fabrication using PDMS can be easily prototyped with simple procedures [4]. However, this multi-step process requires special equipment, and in many cases access to a cleanroom. Furthermore, it generally manufactures the final product at the second step (casting). The process is manual and cannot be fully automated [2].

Due to advancements in the modern additive manufacturing methods, 3DP has been shown as a promising platform for the fabrication of microfluidic devices. 3D printers convert a computer-aided design (CAD) into a physical 3D object by depositing the desired material in a layer by layer fashion [11]. The main advantages of 3DP are automated fabrication process, cost-effectiveness, higher printing resolution, etc. Additionally, these machines make the process simpler and lower the size of the required infrastructure and can be used as desktop printers [3].

S. A. Jaywant (✉) · M. A. A. Rehmani · T. Nayak · K. Mehmood
Department of Mechanical and Electrical Engineering, SF&AT, Massey University, Auckland 0632, New Zealand
e-mail: S.Jaywant@massey.ac.nz

K. Mehmood
e-mail: k.Arif@massey.ac.nz

J. Billingsley and P. Brett (eds.), *Mechatronics and Machine Vision in Practice 4*,
https://doi.org/10.1007/978-3-030-43703-9_10

FIGURE A.4: A paper published in M2VIP-2019 Conference proceedings

Manufacturing and Design New Zealand
20th - 21st May 2019, Auckland

MASSEY UNIVERSITY
TE KUNENGA KI PŪREHUROA

Synthesis of Conductive Ink for Printed Sensors

Muhammad Asif Ali Rehmani, Khalid Arif, Catherine Whitby, Xiaowen Yuan

School of Food and Advanced Technology (SF&AT), Massey University, Auckland

Synthesis of conductive ink through facile processing of lead-tin paste for screen printing applications.

Motivation

- Inks for printed electronics are expensive and requires high temperature for curing.
- After sintering the resolution of the printed features can be improved by coalescing of conductive particles providing better transduction mechanism.

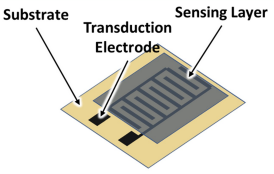

Key findings

- Tin-Lead precursor particle with suitable solvent can be used for printed electrodes
- A facile approach of laser cutting and screen printing provides a resolutions of 130µm-200µm for electrodes.
- Ink improves the resolution of around 10% of printed features.

Objective

- To synthesize highly viscous ink suitable for screen printing
- Ink sintering temperature to be compatible with substrate
- To fabricate cost effective sensing electrode in multi-scale using laser cutting & screen printing.

Synthesis & Results

Laser cutting of PET substrate for bonding on polyimide film

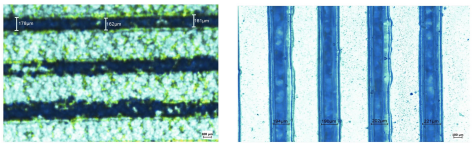

Planar screen printing of tin-lead conductive paste

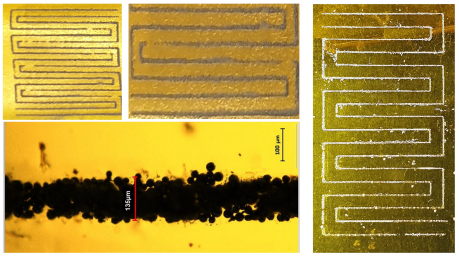

Methodology

- Tin-Lead solder paste 4.8 gm
- Ethyl Alcohol solvent 3.5 gm
- 4-Stage ultrasonic sonication for 5 mins each at 50%, 60%, 70% and 80% power for homogenised ink

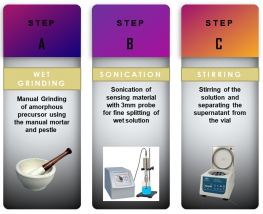

- Separation of solder flux by multiple stage of centrifugation to remove supernatant for 20 mins at 8000 rpm
- Magnetic Stirring of paste for uniform colloidal for 2 hours.

Printed Lines Parameters

Measure	Value
Sintering Temperature	180 ℃
Conductivity	60% of bulk
Particle Size	200 nm
Conductive Particle percentage	70%
Average printed feature	132.5µm

Template Feature Resolution

Measure	Value (µm)
Average	161.7
Minimum	106.3
Maximum	220.0
Standard deviation	32.1

Sensor & Smart Systems Lab, Department of Mechanical and Electrical Engineering, 229 Dairy Flat Highway (Off Kell Drive), Massey University, Auckland 0632, Telephone: +64(09) 414 0800 ext. 43580; Email: k.arif@massey.ac.nz

FIGURE A.5: A poster presented at Manufacturing and Design (MaD) Conference 2019

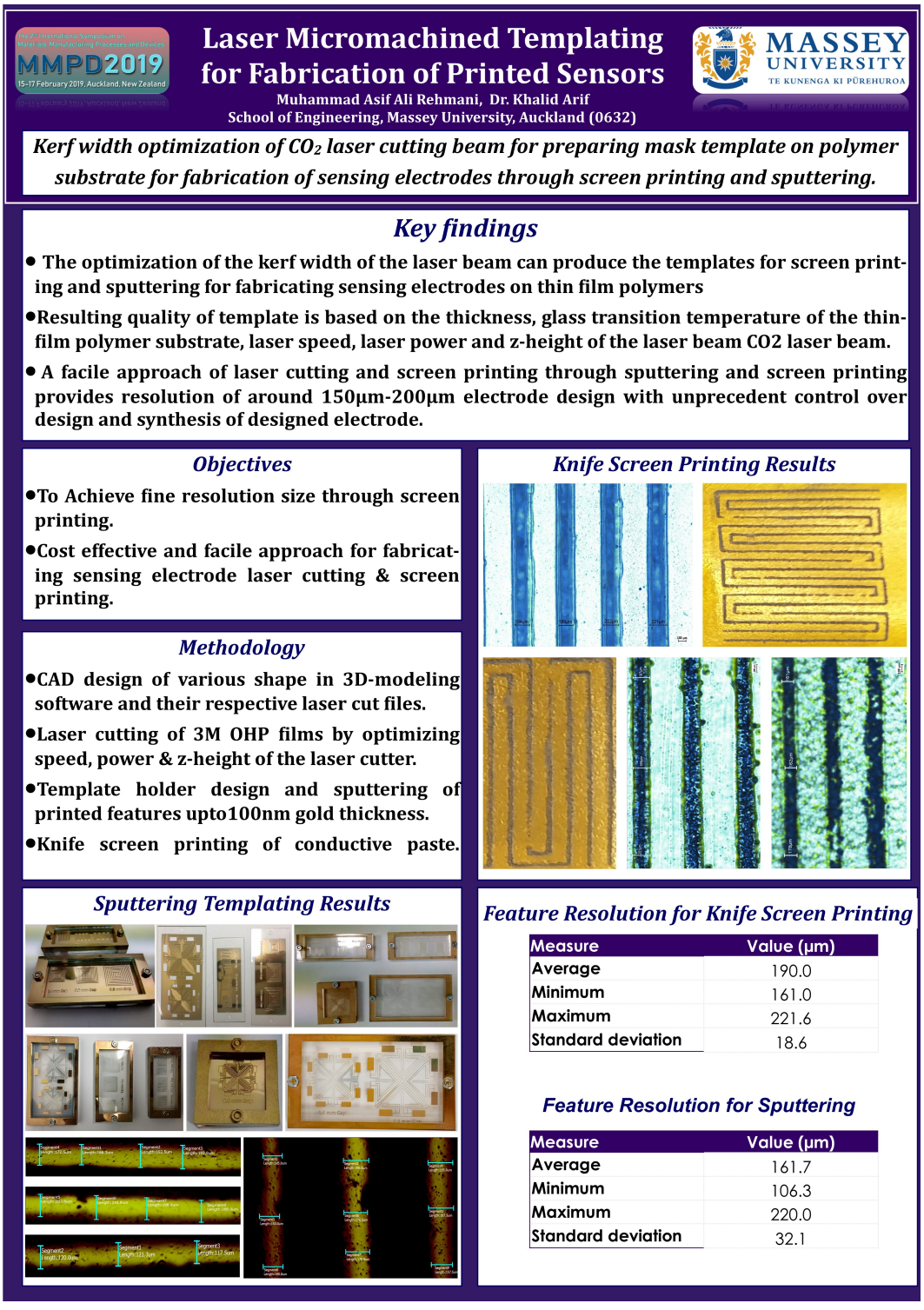

FIGURE A.6: A poster presented at the 2nd International Symposium on Advanced Materials, Manufacturing Processes and Devices (MMPD) 2019

NZ Product Accelerator

Effect of Electrode Geometrical Structure on Signal Transduction in Indoor Air Quality Sensors

MASSEY UNIVERSITY
TE KUNENGA KI PŪREHUROA

Muhammad Asif Ali Rehmani, Khalid Arif, Xiaowen Yuan
School of Engineering and Advanced Technology (SEAT), Massey University, Auckland

Enhancement of transduction sensitivity of thin film flexible sensor through geometrical design & manufacturing using facile screen printing technique

Key findings

- Geometry and shape of electrode can result in highly sensitive transduction scheme for thin film sensors for indoor air quality.
- Serpentine and converging electrode configurations result in high electric displacement field and can be utilized for highly sensitive sensor designs in applications such as air quality monitoring.
- A facile approach of laser cutting and screen printing through sputtering provides a resolutions of 150µm-200µm for electrodes and allows control over the synthesis of the electrode.
- Laser cutter parameters such as power, speed and z-height can be optimized to produce thin templates for screen printing of electrodes.

Objectives

- To achieve fine resolution size via screen printing
- To optimize geometry of the electrode for high sensitivity, compact size and large contact area.
- To fabricate cost effective sensing electrode in multi-scale using laser cutting & screen printing.

Methodology

- CAD design of various shapes using Autodesk Inventor®.
- Numerical simulations of the electrode design.
- Laser cutting of 3M OHP films by optimizing speed, power & z-height of the laser cutter.
- Template holder design and sputtering of printed features upto100nm of gold thickness.
- Measurement of line thickness of the electrodes.

Designs & Numerical Simulation

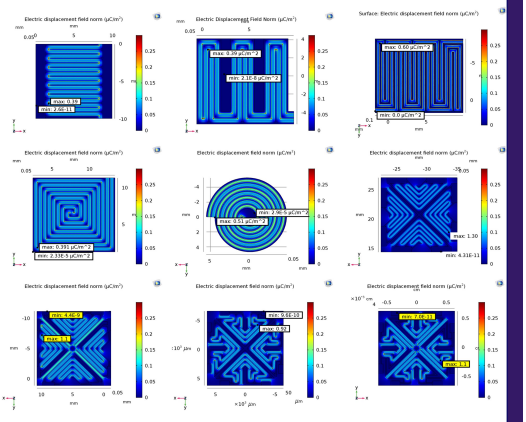

Synthesis & Results

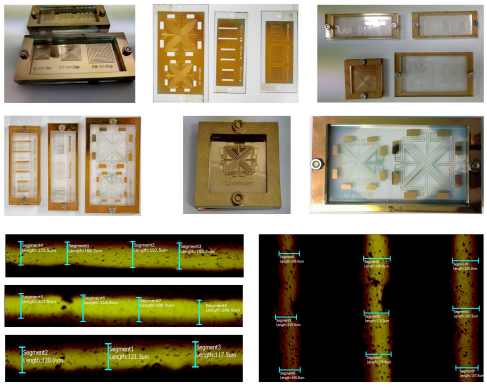

Numerical Results

Geometrical Shape	x (mm)	Y (mm)	Electric Displacement Field (µC/m²)
Meander	0.6	2.9	0.39
Serpentine	-1.1	-7.7	0.60
Spiral	3.0	1.8	0.39
Interdigitated Electrodes	1.7	-8.0	0.39
Swiss Spiral	4.4	0.1	0.51
Triangular Spiral	-3.4	1.8	1.30
Arrow Spiral	-2.1	-4.3	0.92

Feature Resolution

Measure	Value (µm)
Average	161.7
Minimum	106.3
Maximum	220.0
Standard deviation	32.1

Sensor & Robotics Lab, School of Engineering and Advanced Technology, 229, Dairy Flat Highway (Off Kell Drive), Massey University, Auckland 0632
Telephone: +64(09) 414 0800 ext. 43580; Email: k.arif@massey.ac.nz

FIGURE A.7: A poster presented at NZ Product Accelerator 2018

Appendix B

Datasheets

NOVACENTRIX®

Metalon® Conductive Inks for Printed Electronics

www.novacentrix.com

Metalon® JS-A101A and JS-A102A

Nanosilver Ink – Aqueous dispersions for Inkjet Printing

JS-A101A and JS-A102A are electrically conductive inks designed to produce circuits on non-porous, temperature-sensitive substrates including polycarbonate and PET. The inks can be thermally cured or PulseForge® processed. The JS-A series inks are specially formulated for compatibility and stability with various printheads including those manufactured by Dimatix, Xaar and HP. Printing waveforms are available by request.

Performance Properties

	PulseForge 1200		Thermal[3]		
	JS-A101A	JS-A102A	JS-A101A	JS-A102A	Units
Sheet resistance[1]	25	25	< 100	< 100	milli-ohm/square
Volume resistivity[2]	7.8E-06	7.8E-06	< 3.1E-05	< 3.1E-05	ohm-cm
Pencil hardness	>4H	>4H	>4H	>4H	--

Printed on Melinex ST505 with Dimatix DMP-2831 at 20 micron drop spacing.

The inks also display excellent crosshatch adhesion and water resistance after full curing.

[1]Typical values.

[2] Value calculated based on estimate of 50% porosity in cured print.

[3]Thermal cure: 140C 10 minutes

Physical Properties

General Description ..... Water-based Ag ink
Flash Point .....Non-flammable

	JS-A101	JS-A102	Units
Ag content	40	40	wt%
Viscosity	5-7	8-12	cP
Surface tension	19-30	19-30	dyne/cm
z-avg particle size[4]	30-50	30-50	nm
Specific gravity	1.6	1.6	–

[4]Malvern dynamic light scattering

Shipping and Packaging

Standard sample order is 50 mL or multiples of 50 mL. Bulk packaging is also available.

www.novacentrix.com
Contact us today to learn more.
info@novacentrix.com

FIGURE B.1: Datasheet of conductive ink used in chapter 2 and chapter 4

NOVACENTRIX®

Metalon® Conductive Inks for Printed Electronics

www.novacentrix.com

Metalon® HPS-021LV

Silver Screen Ink – Aqueous dispersion

HPS-021LV is an electrically conductive silver flake ink designed to produce conductive traces on low-temperature to high-temperature substrates such as paper, PET, glass, polyimide, and silicon. **HPS-021LV** ink is specially formulated for screen printing.

THERMAL PROCESSING						
Substrate	**Cure Temperature (°C)**	**Cure Time (minutes)**	**Sheet Resistance (mΩ/sq)[1]**	**Weight Resistivity (Ω-g/m²)**	**Volume Resistivity[2] (μΩ-cm)**	**Sheet Resistivity[3] (mΩ/sq/mil)**
Melinex ST505	80	60	35	1.77	33.8	14
	100	60	22	1.07	20.4	9
	125	30	14	0.71	13.5	6
	150	30	11	0.54	10.4	4
Polyimide	200	5	10	0.51	9.7	4
	250	5	6	0.29	5.6	2
	300	5	4	0.23	4.3	2
	375	5	4	0.22	4.3	2
PULSEFORGE PROCESSING						
Melinex ST505	PulseForge[4]	NA	11	0.57	10.85	4
Polyimide	PulseForge[4]	NA	11	0.53	10.12	4

[1] At 0.05 kg/m2 dry ink coverage (150cm²/g wet ink), [2]At 50% porosity, [3] Based on 10 micron print with 50% porosity, [4] Pre-dry sample at 150C for 5 minutes

Physical Properties	**General Description**.....Water-based Ag flake ink **Viscosity (typical values)** .....26,000cP at 0.1sec^{-1}, 800cP at 100 sec^{-1} **Specific Gravity**.....3.1 **Flash Point** .....Non-flammable **Particle Size**.....D50 2.0 micron D90 4.0 micron **Ag Content** .....75 wt%
Shipping and Packaging	Standard sample order is 100g or multiples of 100g. Inquire directly for packaging of larger quantities.

Metalon inks can be directly purchased at store.novacentrix.com
Contact us today to learn more.
info@novacentrix.com

FIGURE B.2: Datasheet of screen printing ink used in chapter 3 and chapter 4

SIGMA-ALDRICH® sigma-aldrich.com

3050 Spruce Street, Saint Louis, MO 63103, USA
Website: www.sigmaaldrich.com
Email USA: techserv@sial.com
Outside USA: eurtechserv@sial.com

Product Specification

Product Name:
Sigmacell Cellulose - Type 20, 20 µm

Product Number:	**S3504**
CAS Number:	9004-34-6
MDL:	MFCD00081512

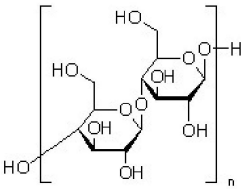

TEST	Specification
Appearance (Color)	White to Off-White
Appearance (Form)	Powder
Suitability	Suitable
Suitable for use as a thin layer chromotography reagent	
Loss on Drying	1 - 5 %

Specification: PRD.0.ZQ5.10000038047

FIGURE B.3: Datasheet of cellulose sensing element used in chapter 3

SIGMA-ALDRICH®

sigma-aldrich.com

3050 Spruce Street, Saint Louis, MO 63103, USA
Website: www.sigmaaldrich.com
Email USA: techserv@sial.com
Outside USA: eurtechserv@sial.com

Product Specification

Product Name:
Poly(3,4-ethylenedioxythiophene)-poly(styrenesulfonate) - high-conductivity grade

Product Number: **900181**

TEST	Specification
Appearance (Color)	Dark Blue to Very Dark Blue
Appearance (Form)	Liquid or Suspension
pH	2.0 - 3.5
Surface Resistance (ohm/sq)	< 200
(coating: 40u wet - drying: 6 min 130°C)	
Viscosity	< 70
mPa.s	
at 20°C	
Transmission	≥ 80 %
Visual Light	
Trademark	Confirmed
Orgacon is a trademark of Agfa-Gevaert N.V.	
Recommended Retest Period	----------
1 Year	

Specification: PRD.2.ZQ5.10000076780

FIGURE B.4: Datasheet of PEDOT:PSS sensing element used in chapter 3

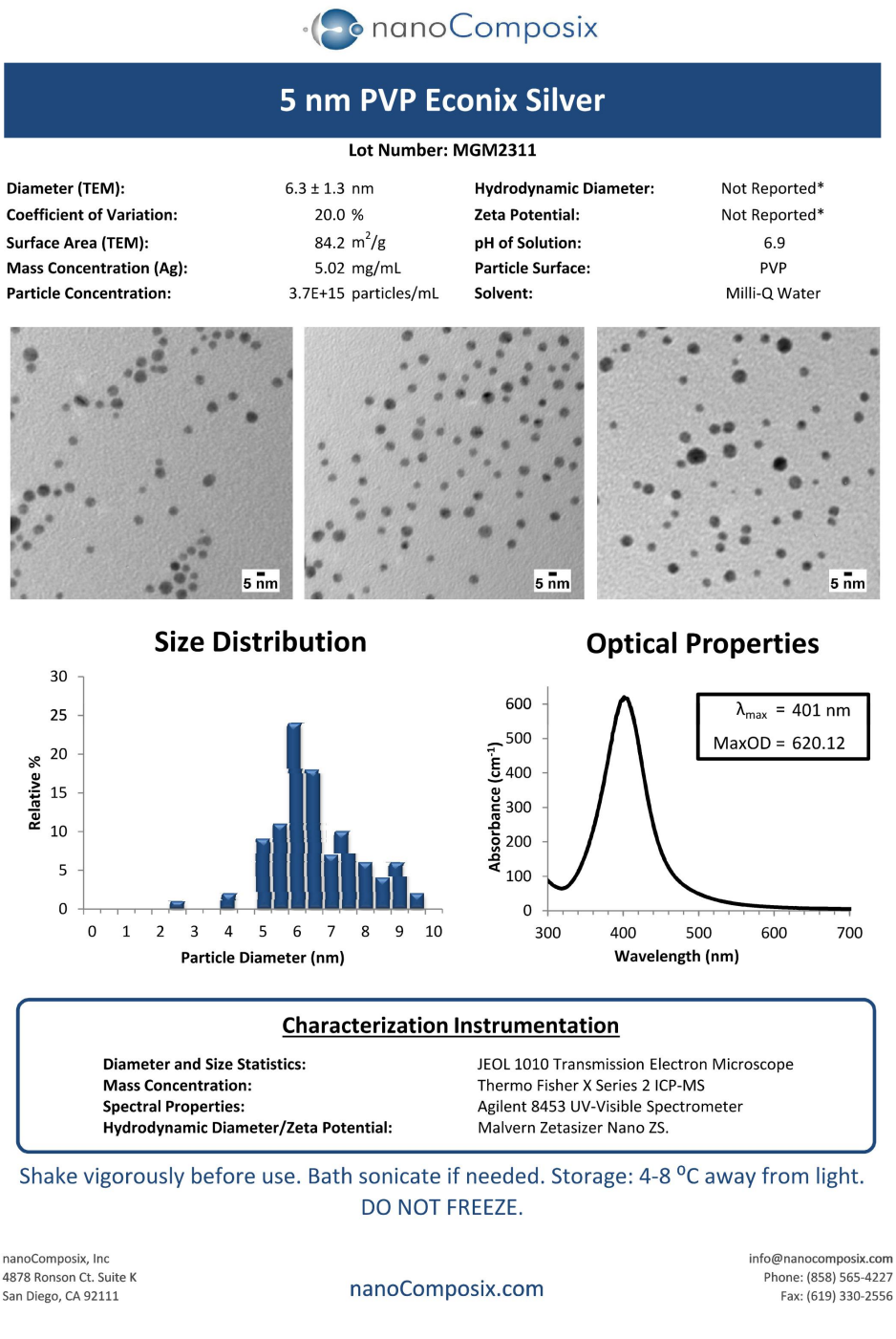

FIGURE B.5: Datasheet of PVP SNP steric stabilizer used in chapter 3

NOVACENTRIX®

Metalon® Conductive Inks for Printed Electronics

www.novacentrix.com

Metalon® JS-A291

Nanosilver Ink – Aqueous dispersion for Inkjet Printing

JS-A291 is an electrically conductive ink designed to produce circuits on non-porous, temperature-sensitive substrates including polycarbonate, PET, polyimide, and glass. The ink contains a polyurethane which provides excellent adhesion and water-resistance on most substrates. The JS-A series of inks are specially formulated for compatibility and stability with various printheads including those manufactured by Dimatix and Xaar. Printing waveforms are available by request.

Performance Properties

Cure temperature (°C)	Cure time (minutes)	Volume Resistivity (Ω-cm)[1]	Crosshatch Adhesion	Substrate
100	60	5.3 x 10E-4	5B	Melinex ST505
120	30	2.4 x 10E-4	5B	Melinex ST505
140	10	8.6 x 10E-5	5B	Melinex ST505
175	10	3.7 x 10E-5	5B	Polyimide
200	5	2.1 x 10E-5	5B	Polyimide
250	5	9.9 x 10E-6	5B	Polyimide

[1]Value calculated based on estimate of 25% porosity of cured print.

Physical Properties

General Description ..... Water-based Ag ink
Flash Point .....Non-flammable

	Value	Units
Ag content	40	wt%
Viscosity	8-12	cP
Surface tension	28-32	dyne/cm
z-avg particle size[3]	30-50	nm
Specific gravity	1.6	–

[3] Malvern dynamic light scattering

Shipping and Packaging

Standard sample order is 50 mL or multiples of 50 mL. Bulk packaging is also available.

www.novacentrix.com
Contact us today to learn more.
info@novacentrix.com

FIGURE B.6: Datasheet of conductive ink used in Chapter 4

NOVACENTRIX®

Metalon® Conductive Inks for Printed Electronics

www.novacentrix.com

Metalon® JS-A211

Nanosilver Ink – Aqueous dispersion for Inkjet Printing

JS-A211 is an electrically conductive ink designed to produce circuits on non-porous, temperature-sensitive substrates including polycarbonate, PET, polyimide, and glass. The ink contains a fluoropolymer which provides excellent adhesion and water-resistance on most substrates. The JS-A series of inks are specially formulated for compatibility and stability with various printheads including those manufactured by Dimatix and Xaar. Printing waveforms are available by request.

Performance Properties

Cure temperature (°C)	Cure time (minutes)	Volume Resistivity (Ω-cm)[1]	Crosshatch Adhesion	Substrate
100	60	7.3 x 10E-4	5B	PET
120	60	2.4 x 10E-4	5B	PET
140	30	8.6 x 10E-5	5B	PET
175	10	2.1 x 10E-5	5B	Polyimide
200	5	1.3 x 10E-5	5B	Polyimide
250	5	7.7 x 10E-6	5B	Polyimide

[1]Value calculated based on estimate of 25% porosity of cured print.

Physical Properties

General Description ..... Water-based Ag ink
Flash Point .....Non-flammable

	Value	Units
Ag content	40	wt%
Viscosity	8-12	cP
Surface tension	28-32	dyne/cm
z-avg particle size[3]	30-50	nm
Specific gravity	1.6	–

[3] Malvern dynamic light scattering

Shipping and Packaging

Standard sample order is 50 mL or multiples of 50 mL. Bulk packaging is also available.

www.novacentrix.com
Contact us today to learn more.
info@novacentrix.com

FIGURE B.7: Datasheet of conductive ink used in Chapter 4

Appendix C

DRC16 Forms

DRC 16

MASSEY UNIVERSITY
TE KUNENGA KI PŪREHUROA
UNIVERSITY OF NEW ZEALAND

GRADUATE RESEARCH SCHOOL

STATEMENT OF CONTRIBUTION
DOCTORATE WITH PUBLICATIONS/MANUSCRIPTS

We, the candidate and the candidate's Primary Supervisor, certify that all co-authors have consented to their work being included in the thesis and they have accepted the candidate's contribution as indicated below in the *Statement of Originality*.

Name of candidate:	Muhammad Asif Ali Rehmani
Name/title of Primary Supervisor:	Dr. Khalid Arif
In which chapter is the manuscript /published work:	Chapter 2

Please select one of the following three options:

(●) The manuscript/published work is published or in press

- Please provide the full reference of the Research Output:

M. A. A. Rehmani and K. M. Arif, "High resolution electrohydrodynamic printing of conductive ink with an aligned aperture coaxial printhead," The International Journal of Advanced Manufacturing Technology, vol. 115, no. 9, pp. 2785-2800, 2021/08/01 2021, doi: 10.1007/s00170-021-07075-6.

( ) The manuscript is currently under review for publication – please indicate:

- The name of the journal:
- The percentage of the manuscript/published work that was contributed by the candidate:
- Describe the contribution that the candidate has made to the manuscript/published work:

( ) It is intended that the manuscript will be published, but it has not yet been submitted to a journal

Candidate's Signature:	Muhammad Asif Ali Rehmani — Digitally signed by Muhammad Asif Ali Rehmani Date: 2021.10.30 13:28:14 +13'00'
Date:	30-Oct-2021
Primary Supervisor's Signature:	Khalid Arif, Senior Lecturer — Digitally signed by Khalid Arif, Senior Lecturer Date: 2021.10.30 14:23:24 +13'00'
Date:	30-Oct-2021

This form should appear at the end of each thesis chapter/section/appendix submitted as a manuscript/ publication or collected as an appendix at the end of the thesis.

DRC 16

MASSEY UNIVERSITY
TE KUNENGA KI PŪREHUROA
UNIVERSITY OF NEW ZEALAND

GRADUATE RESEARCH SCHOOL

STATEMENT OF CONTRIBUTION
DOCTORATE WITH PUBLICATIONS/MANUSCRIPTS

We, the candidate and the candidate's Primary Supervisor, certify that all co-authors have consented to their work being included in the thesis and they have accepted the candidate's contribution as indicated below in the *Statement of Originality*.

Name of candidate:	Muhammad Asif Ali Rehmani
Name/title of Primary Supervisor:	Dr. Khalid Arif
In which chapter is the manuscript /published work:	Chapter 3

Please select one of the following three options:

○ The manuscript/published work is published or in press

- Please provide the full reference of the Research Output:

○ The manuscript is currently under review for publication – please indicate:

- The name of the journal:
- The percentage of the manuscript/published work that was contributed by the candidate:
- Describe the contribution that the candidate has made to the manuscript/published work:

◉ It is intended that the manuscript will be published, but it has not yet been submitted to a journal

Candidate's Signature:	Muhammad Asif Ali Rehmani — Digitally signed by Muhammad Asif Ali Rehmani Date: 2021.10.30 13:48:45 +13'00'
Date:	30-Oct-2021
Primary Supervisor's Signature:	Khalid Arif, Senior Lecturer — Digitally signed by Khalid Arif, Senior Lecturer Date: 2021.10.30 14:23:41 +13'00'
Date:	30-Oct-2021

This form should appear at the end of each thesis chapter/section/appendix submitted as a manuscript/ publication or collected as an appendix at the end of the thesis.

DRC 16

MASSEY UNIVERSITY
TE KUNENGA KI PŪREHUROA
UNIVERSITY OF NEW ZEALAND

GRADUATE RESEARCH SCHOOL

STATEMENT OF CONTRIBUTION
DOCTORATE WITH PUBLICATIONS/MANUSCRIPTS

We, the candidate and the candidate's Primary Supervisor, certify that all co-authors have consented to their work being included in the thesis and they have accepted the candidate's contribution as indicated below in the *Statement of Originality*.

Name of candidate:	Muhammad Asif Ali Rehmani
Name/title of Primary Supervisor:	Dr. Khalid Arif
In which chapter is the manuscript /published work:	Chapter 3

Please select one of the following three options:

(●) The manuscript/published work is published or in press

- Please provide the full reference of the Research Output:

M. A. A. Rehmani and K. M. Arif, "Capacitive Transduction Schemes for Environmental Humidity Sensors," in 2019 13th International Conference on Sensing Technology (ICST), 2019: IEEE, pp. 1-5, doi:10.1109/ICST46873.2019.9047700.

( ) The manuscript is currently under review for publication – please indicate:

- The name of the journal:
- The percentage of the manuscript/published work that was contributed by the candidate:
- Describe the contribution that the candidate has made to the manuscript/published work:

( ) It is intended that the manuscript will be published, but it has not yet been submitted to a journal

Candidate's Signature:	Muhammad Asif Ali Rehmani — Digitally signed by Muhammad Asif Ali Rehmani Date: 2021.10.30 14:03:21 +13'00'
Date:	30-Oct-2021
Primary Supervisor's Signature:	Khalid Arif, Senior Lecturer — Digitally signed by Khalid Arif, Senior Lecturer Date: 2021.10.30 14:24:06 +13'00'
Date:	30-Oct-2021

This form should appear at the end of each thesis chapter/section/appendix submitted as a manuscript/ publication or collected as an appendix at the end of the thesis.

DRC 16

MASSEY UNIVERSITY
TE KUNENGA KI PŪREHUROA
UNIVERSITY OF NEW ZEALAND

GRADUATE RESEARCH SCHOOL

STATEMENT OF CONTRIBUTION
DOCTORATE WITH PUBLICATIONS/MANUSCRIPTS

We, the candidate and the candidate's Primary Supervisor, certify that all co-authors have consented to their work being included in the thesis and they have accepted the candidate's contribution as indicated below in the *Statement of Originality*.

Name of candidate:	Muhammad Asif Ali Rehmani
Name/title of Primary Supervisor:	Dr. Khalid Arif
In which chapter is the manuscript /published work:	Chapter 4

Please select one of the following three options:

○ The manuscript/published work is published or in press

- Please provide the full reference of the Research Output:

○ The manuscript is currently under review for publication – please indicate:

- The name of the journal:
- The percentage of the manuscript/published work that was contributed by the candidate:
- Describe the contribution that the candidate has made to the manuscript/published work:

◉ It is intended that the manuscript will be published, but it has not yet been submitted to a journal

Candidate's Signature:	Muhammad Asif Ali Rehmani — Digitally signed by Muhammad Asif Ali Rehmani Date: 2021.10.30 13:50:29 +13'00'
Date:	30-Oct-2021
Primary Supervisor's Signature:	Khalid Arif, Senior Lecturer — Digitally signed by Khalid Arif, Senior Lecturer Date: 2021.10.30 14:23:06 +13'00'
Date:	30-Oct-2021

This form should appear at the end of each thesis chapter/section/appendix submitted as a manuscript/ publication or collected as an appendix at the end of the thesis.

DRC 16

MASSEY UNIVERSITY
TE KUNENGA KI PŪREHUROA
UNIVERSITY OF NEW ZEALAND

GRADUATE RESEARCH SCHOOL

STATEMENT OF CONTRIBUTION
DOCTORATE WITH PUBLICATIONS/MANUSCRIPTS

We, the candidate and the candidate's Primary Supervisor, certify that all co-authors have consented to their work being included in the thesis and they have accepted the candidate's contribution as indicated below in the *Statement of Originality*.

Name of candidate:	Muhammad Asif Ali Rehmani
Name/title of Primary Supervisor:	Dr. Khalid Arif
In which chapter is the manuscript /published work:	Chapter 5

Please select one of the following three options:

(●) The manuscript/published work is published or in press

- Please provide the full reference of the Research Output:

M. A. A. Rehmani, S. A. Jaywant, and K. M. Arif, "Study of Microchannels Fabricated Using Desktop Fused Deposition Modeling Systems," Micromachines, vol. 12, no. 1, p. 14, 2021, doi:10.3390/mi12010014.

( ) The manuscript is currently under review for publication – please indicate:

- The name of the journal:

- The percentage of the manuscript/published work that was contributed by the candidate:

- Describe the contribution that the candidate has made to the manuscript/published work:

( ) It is intended that the manuscript will be published, but it has not yet been submitted to a journal

Candidate's Signature:	Muhammad Asif Ali Rehmani — Digitally signed by Muhammad Asif Ali Rehmani Date: 2021.10.30 13:38:17 +13'00'
Date:	30-Oct-2021
Primary Supervisor's Signature:	Khalid Arif, Senior Lecturer — Digitally signed by Khalid Arif, Senior Lecturer Date: 2021.10.30 14:22:00 +13'00'
Date:	30-Oct-2021

This form should appear at the end of each thesis chapter/section/appendix submitted as a manuscript/ publication or collected as an appendix at the end of the thesis.

DRC 16

MASSEY UNIVERSITY
TE KUNENGA KI PŪREHUROA
UNIVERSITY OF NEW ZEALAND

GRADUATE RESEARCH SCHOOL

STATEMENT OF CONTRIBUTION
DOCTORATE WITH PUBLICATIONS/MANUSCRIPTS

We, the candidate and the candidate's Primary Supervisor, certify that all co-authors have consented to their work being included in the thesis and they have accepted the candidate's contribution as indicated below in the *Statement of Originality*.

Name of candidate:	Muhammad Asif Ali Rehmani
Name/title of Primary Supervisor:	Dr. Khalid Arif
In which chapter is the manuscript /published work:	Chapter 5

Please select one of the following three options:

(●) The manuscript/published work is published or in press

- Please provide the full reference of the Research Output:

S. A. Jaywant, M. A. A. Rehmani, T. Nayak, and K. Mehmood, "Fabrication and Characterization of 3D Printed Microfluidics," in Mechatronics and Machine Vision in Practice 4: Springer, 2021, pp. 119-124. doi:10.1007/978-3-030-43703-9_10

( ) The manuscript is currently under review for publication – please indicate:

- The name of the journal:
- The percentage of the manuscript/published work that was contributed by the candidate:
- Describe the contribution that the candidate has made to the manuscript/published work:

( ) It is intended that the manuscript will be published, but it has not yet been submitted to a journal

Candidate's Signature:	Muhammad Asif Ali Rehmani — Digitally signed by Muhammad Asif Ali Rehmani Date: 2021.10.30 14:06:27 +13'00'
Date:	30-Oct-2021
Primary Supervisor's Signature:	Khalid Arif, Senior Lecturer — Digitally signed by Khalid Arif, Senior Lecturer Date: 2021.10.30 14:22:27 +13'00'
Date:	30-Oct-2021

This form should appear at the end of each thesis chapter/section/appendix submitted as a manuscript/ publication or collected as an appendix at the end of the thesis.

References

[1] I Myers and RL Maynard. Polluted air—outdoors and indoors. *Occupational medicine*, 55(6):432–438, 2005.

[2] World Health Organization et al. *WHO guidelines for indoor air quality: selected pollutants*. World Health Organization. Regional Office for Europe, 2010.

[3] World Health Organization et al. Ambient air pollution: A global assessment of exposure and burden of disease. 2016.

[4] EPA Buildings. Buildings and their impact on the environment: A statistical summary. *Washington, DC: US Environmental Protection Agency*, 2009.

[5] Herman Wijshoff. The dynamics of the piezo inkjet printhead operation. *Physics reports*, 491(4-5):77–177, 2010.

[6] Marc Aliqué, Claudia Delgado Simão, Gonzalo Murillo, and Ana Moya. Fully-printed piezoelectric devices for flexible electronics applications. *Advanced Materials Technologies*, 6(3):2001020, 2021.

[7] Nobutoshi Komuro, Shunsuke Takaki, Koji Suzuki, and Daniel Citterio. Inkjet printed (bio) chemical sensing devices. *Analytical and bioanalytical chemistry*, 405 (17):5785–5805, 2013.

[8] Pratikkumar Vikramark Raje and Naresh Chandra Murmu. A review on electrohydrodynamic-inkjet printing technology. *Int J Emerg Technol Adv Eng*, 4(5):174–183, 2014.

[9] Hue P Le. Progress and trends in ink-jet printing technology. *Journal of Imaging Science and Technology*, 42(1):49–62, 1998.

[10] Yuji Ishida, Keigo Sogabe, Shintaro Kai, and Tanemasa Asano. Droplet ejection behavior in electrostatic inkjet driving. *Japanese Journal of Applied Physics*, 47 (6S):5281, 2008.

[11] Daniel C Hughes and Steven E Ernster. Screen printed feature size capabilities. In *SPIE proceedings series*, pages 58–62, 2003.

[12] Jongsu Lee, Soosung Park, Kee-Hyun Shin, and Hoeryong Jung. Smearing defects: a root cause of register measurement error in roll-to-roll additive manufacturing system. *The International Journal of Advanced Manufacturing Technology*, 98(9): 3155–3165, 2018.

[13] Cheol Kim, Sung Woong Jeon, and Chung Hwan Kim. Measurement of position accuracy of engraving in plate roller and its effect on register accuracy in roll-to-roll multi-layer printing. *Measurement Science and Technology*, 28(12):125002, 2017.

[14] Cheol Kim, Sung Woong Jeon, and Chung Hwan Kim. Reduction of linearly varying term of register errors using a dancer system in roll-to-roll printing equipment for printed electronics. *International Journal of Precision Engineering and Manufacturing*, 20(9):1485–1493, 2019.

[15] Eonseok Lee, Young-Man Choi, Seung-Hyun Lee, Sin Kwon, Taik-Min Lee, and Dongwoo Kang. Enhancement of printing overlay accuracy by reducing the effects of mark deformations. *Microelectronic Engineering*, 180:8–14, 2017.

[16] Mark AM Leenen, Volker Arning, Heiko Thiem, Jürgen Steiger, and Ralf Anselmann. Printable electronics: Flexibility for the future. *physica status solidi (a)*, 206(4):588–597, 2009.

[17] Robert Abbel, Yulia Galagan, and Pim Groen. Roll-to-roll fabrication of solution processed electronics. *Advanced Engineering Materials*, 20(8):1701190, 2018.

[18] Byung-Yong Wang, Eung-Seok Lee, Dae-Soon Lim, Hyun Wook Kang, and Young-Jei Oh. Roll-to-roll slot die production of 300 mm large area silver nanowire mesh films for flexible transparent electrodes. *RSC advances*, 7(13):7540–7546, 2017.

[19] Yasser Khan, Arno Thielens, Sifat Muin, Jonathan Ting, Carol Baumbauer, and Ana C Arias. A new frontier of printed electronics: flexible hybrid electronics. *Advanced Materials*, 32(15):1905279, 2020.

[20] Wei Wu. Inorganic nanomaterials for printed electronics: a review. *Nanoscale*, 9 (22):7342–7372, 2017.

[21] HW Tan, T Tran, and CK Chua. A review of printed passive electronic components through fully additive manufacturing methods. *Virtual and Physical Prototyping*, 11(4):271–288, 2016.

[22] Daniele Foresti, Katharina T Kroll, Robert Amissah, Francesco Sillani, Kimberly A Homan, Dimos Poulikakos, and Jennifer A Lewis. Acoustophoretic printing. *Science advances*, 4(8):eaat1659, 2018.

[23] William Gilbert. *De magnete, magneticisque corporibus, et de magno magnete tellure: physiologia noua, plurimis & argumentis, & experimentis demonstrata.* excudebat Short, 1967.

[24] Geoffrey Ingram Taylor. Disintegration of water drops in an electric field. *Proceedings of the Royal Society of London. Series A. Mathematical and Physical Sciences*, 280(1382):383–397, 1964.

[25] Fei Zheng, Brian Derby, and Jason Wong. Fabrication of microvascular constructs using high resolution electrohydrodynamic inkjet printing. *Biofabrication*, 13(3): 035006, 2021.

[26] Ju-Hwan Choi, Ju-Hun Ahn, and Chang-Yull Lee. Flexible structural color films based on electro-hydrodynamic inkjet printing. *Coatings*, 11(3):277, 2021.

[27] A Jaworek, AT Sobczyk, and A Krupa. Electrospray application to powder production and surface coating. *Journal of Aerosol Science*, 125:57–92, 2018.

[28] Md Khalilur Rahman, Thanh Huy Phung, Soobin Oh, Se Hyun Kim, Tse Nga Ng, and Kye-Si Kwon. High-efficiency electrospray deposition method for nonconductive substrates: Applications of superhydrophobic coatings. *ACS applied materials & interfaces*, 13(15):18227–18236, 2021.

[29] Eng San Thian, Xiang Li, Jie Huang, Mohan J Edirisinghe, William Bonfield, and Serena M Best. Electrospray deposition of nanohydroxyapatite coatings: A strategy to mimic bone apatite mineral. *Thin Solid Films*, 519(7):2328–2331, 2011.

[30] Lin Lei, Dylan A Kovacevich, Michael P Nitzsche, Jihyun Ryu, Kutaiba Al-Marzoki, Gabriela Rodriguez, Lisa C Klein, Andrei Jitianu, and Jonathan P Singer. Obtaining thickness-limited electrospray deposition for 3d coating. *ACS applied materials & interfaces*, 10(13):11175–11188, 2018.

[31] Antonio Ramos. Electrohydrodynamic pumping in microsystems. *Electrokinetics and electrohydrodynamics in microsystems*, pages 127–175, 2011.

[32] Wonkyoung Kim, Jae Chun Ryu, Yong Kweon Suh, and Kwan Hyoung Kang. Pumping of dielectric liquids using non-uniform-field induced electrohydrodynamic flow. *Applied Physics Letters*, 99(22):224102, 2011.

[33] R Bakhshi, MJ Edirisinghe, A Darbyshire, Zeeshan Ahmad, and AM Seifalian. Electrohydrodynamic jetting behaviour of polyhedral oligomeric silsesquioxane nanocomposite. *Journal of biomaterials applications*, 23(4):293–309, 2009.

[34] María José Fabra, Amparo López-Rubio, and Jose M Lagaron. Use of the electrohydrodynamic process to develop active/bioactive bilayer films for food packaging applications. *Food Hydrocolloids*, 55:11–18, 2016.

[35] Suriyan Laohalertdecha, Paisarn Naphon, and Somchai Wongwises. A review of electrohydrodynamic enhancement of heat transfer. *Renewable and Sustainable Energy Reviews*, 11(5):858–876, 2007.

[36] Olivier Rouaud, Michel Havet, et al. Assessment of the electrohydrodynamic drying process. *Food and Bioprocess Technology*, 2(3):240–247, 2009.

[37] Leilei Zhang, Jiwei Huang, Ting Si, and Ronald X Xu. Coaxial electrospray of microparticles and nanoparticles for biomedical applications. *Expert review of medical devices*, 9(6):595–612, 2012.

[38] Marjan Enayati, Ming-Wei Chang, Felix Bragman, Mohan Edirisinghe, and Eleanor Stride. Electrohydrodynamic preparation of particles, capsules and bubbles for biomedical engineering applications. *Colloids and Surfaces A: Physicochemical and Engineering Aspects*, 382(1-3):154–164, 2011.

[39] Yang Wu. Electrohydrodynamic jet 3d printing in biomedical applications. *Acta Biomaterialia*, 2021.

[40] Hongtao Liang, Jiankang He, Jinke Chang, Bing Zhang, and Dichen Li. Coaxial nozzle-assisted electrohydrodynamic printing for microscale 3d cell-laden constructs. *International journal of bioprinting*, 4(1), 2018.

[41] Thanh Huy Phung, Luu Ngoc Nguyen, and Kye-Si Kwon. A vector printing method for high-speed electrohydrodynamic (ehd) jet printing based on encoder position sensors. *Applied Sciences*, 8(3):351, 2018.

[42] J. Heinzl and C.H. Hertz. Ink-jet printing. volume 65 of *Advances in Electronics and Electron Physics*, pages 91–171. Academic Press, 1985. doi: https://doi.org/10.1016/S0065-2539(08)60877-X. URL https://www.sciencedirect.com/science/article/pii/S006525390860877X.

[43] Thi Thu Thuy Can, Tuan Canh Nguyen, and Woon-Seop Choi. Patterning of high-viscosity silver paste by an electrohydrodynamic-jet printer for use in tft applications. *Scientific reports*, 9(1):1–8, 2019.

[44] Xinlin Li, Eun Mi Jung, Ki Seung Kim, Jeong Hyun Oh, Tae Kyu An, Seung Woo Lee, and Se Hyun Kim. Printed water-based ito nanoparticle via electrohydrodynamic (ehd) jet printing and its application of zno transistors. *Electronic Materials Letters*, 15(5):595–604, 2019.

[45] D Gao and JG Zhou. Designs and applications of electrohydrodynamic three-dimensional printing (vol 5, pg 172, 2019). *INTERNATIONAL JOURNAL OF BIOPRINTING*, 6(4):130–130, 2020.

[46] Changhai Ru, Jun Luo, Shaorong Xie, and Yu Sun. A review of non-contact micro- and nano-printing technologies. *Journal of Micromechanics and Microengineering*, 24(5):053001, 2014.

[47] Kazuhiro Murata, Junichi Matsumoto, Akira Tezuka, Yorishige Matsuba, and Hiroshi Yokoyama. Super-fine ink-jet printing: toward the minimal manufacturing system. *Microsystem technologies*, 12(1):2–7, 2005.

[48] A Jaworek and A Krupa. Classification of the modes of ehd spraying. *Journal of aerosol science*, 30(7):873–893, 1999.

[49] Thanh Huy Phung, Soobin Oh, and Kye-Si Kwon. High-resolution patterning using two modes of electrohydrodynamic jet: drop on demand and near-field electrospinning. *Journal of visualized experiments: JoVE*, (137), 2018.

[50] Zhentao Wang, Lei Xia, and Shuiqing Zhan. Experimental study on electrohydrodynamics (ehd) spraying of ethanol with double-capillary. *Applied Thermal Engineering*, 120:474–483, 2017.

[51] Tongju Wang, Jian Lin, Xingye Guo, Yongping Lei, and Hanguang Fu. A new method for producing uniform droplets by continuous-ink-jet technology. *Review of Scientific Instruments*, 89(8):085008, 2018.

[52] Milim Yu, Kyung Hyun Ahn, and Seung Jong Lee. Design optimization of ink in electrohydrodynamic jet printing: Effect of viscoelasticity on the formation of taylor cone jet. *Materials & Design*, 89:109–115, 2016.

[53] Seongpil An, Min Wook Lee, Na Young Kim, Changmin Lee, Salem S Al-Deyab, Scott C James, and Sam S Yoon. Effect of viscosity, electrical conductivity, and surface tension on direct-current-pulsed drop-on-demand electrohydrodynamic printing frequency. *Applied Physics Letters*, 105(21):214102, 2014.

[54] Yonghee Jang, Indra Hartarto Tambunan, Hyowon Tak, Vu Dat Nguyen, TaeSam Kang, and Doyoung Byun. Non-contact printing of high aspect ratio ag electrodes for polycrystalline silicone solar cell with electrohydrodynamic jet printing. *Applied Physics Letters*, 102(12):123901, 2013.

[55] Kazuyo Shigeta, Ying He, Erick Sutanto, Somi Kang, An-Phong Le, Ralph G Nuzzo, Andrew G Alleyne, Placid M Ferreira, Yi Lu, and John A Rogers. Functional protein microarrays by electrohydrodynamic jet printing. *Analytical chemistry*, 84(22):10012–10018, 2012.

[56] Prina Mehta, Rita Haj-Ahmad, Manoochehr Rasekh, Muhammad S Arshad, Ashleigh Smith, Susanna M van der Merwe, Xiang Li, Ming-Wei Chang, and Zeeshan Ahmad. Pharmaceutical and biomaterial engineering via electrohydrodynamic atomization technologies. *Drug Discovery Today*, 22(1):157–165, 2017.

[57] Zeeshan Ahmad, HB Zhang, U Farook, M Edirisinghe, E Stride, and P Colombo. Generation of multilayered structures for biomedical applications using a novel tri-needle coaxial device and electrohydrodynamic flow. *Journal of the Royal Society Interface*, 5(27):1255–1261, 2008.

[58] Michael J Poellmann, Kira L Barton, Sandipan Mishra, and Amy J Wagoner Johnson. Patterned hydrogel substrates for cell culture with electrohydrodynamic jet printing. *Macromolecular bioscience*, 11(9):1164–1168, 2011.

[59] JR Melcher and GI Taylor. Electrohydrodynamics: a review of the role of interfacial shear stresses. *Annual review of fluid mechanics*, 1(1):111–146, 1969.

[60] DA Saville. Electrohydrodynamics: the taylor-melcher leaky dielectric model. *Annual review of fluid mechanics*, 29(1):27–64, 1997.

[61] Dong Ho Choi and Ian R Smith. Electrohydrodynamic ink jet printer and printing method, November 17 1998. US Patent 5,838,349.

[62] Jang-Ung Park, Matt Hardy, Seong Jun Kang, Kira Barton, Kurt Adair, Deep kishore Mukhopadhyay, Chang Young Lee, Michael S Strano, Andrew G Alleyne, John G Georgiadis, et al. High-resolution electrohydrodynamic jet printing. *Nature materials*, 6(10):782–789, 2007.

[63] Sandipan Mishra, Kira Barton, and Andrew Alleyne. Control of high-resolution electrohydrodynamic jet printing. In *Proceedings of the 2010 American Control Conference*, pages 6537–6542. IEEE, 2010.

[64] Kira Barton, Sandipan Mishra, Andrew Alleyne, Placid Ferreira, and John Rogers. Control of high-resolution electrohydrodynamic jet printing. *Control Engineering Practice*, 19(11):1266–1273, 2011.

[65] Kira Barton, Sandipan Mishra, K Alex Shorter, Andrew Alleyne, Placid Ferreira, and John Rogers. A desktop electrohydrodynamic jet printing system. *Mechatronics*, 20(5):611–616, 2010.

[66] Young Jin Yang, Hyung Chan Kim, Memoon Sajid, Soo wan Kim, Shahid Aziz, Young Soo Choi, and Kyung Hyun Choi. Drop-on-demand electrohydrodynamic printing of high resolution conductive micro patterns for mems repairing. *International Journal of Precision Engineering and Manufacturing*, 19(6):811–819, 2018.

[67] Tae Heon Hwang, Yong Jae Kim, Haseung Chung, and WonHyoung Ryu. Motionless electrohydrodynamic (ehd) printing of biodegradable polymer micro patterns. *Microelectronic Engineering*, 161:43–51, 2016.

[68] Fariza Dian Prasetyo, Hadi Teguh Yudistira, Vu Dat Nguyen, and Doyoung Byun. Ag dot morphologies printed using electrohydrodynamic (ehd) jet printing based on a drop-on-demand (dod) operation. *Journal of Micromechanics and Microengineering*, 23(9):095028, 2013.

[69] Hong Kyoon Choi, Jang-Ung Park, O Ok Park, Placid M Ferreira, John G Georgiadis, and John A Rogers. Scaling laws for jet pulsations associated with high-resolution electrohydrodynamic printing. *Applied Physics Letters*, 92(12):123109, 2008.

[70] Wuhao Zou, Haibo Yu, Peilin Zhou, and Lianqing Liu. Tip-assisted electrohydrodynamic jet printing for high-resolution microdroplet deposition. *Materials & Design*, 166:107609, 2019.

[71] Yeongjun Kim, Shin Jang, and Je Hoon Oh. High-resolution electrohydrodynamic printing of silver nanoparticle ink via commercial hypodermic needles. *Applied Physics Letters*, 106(1):014103, 2015.

[72] Jung Woo Sohn, Chulhee Han, Chun-Yong Park, and Seung-Bok Choi. An electrohydrodynamic jet printing system with metal nanoparticle-based ink: experimental evaluation. *IEEE Transactions on Components, Packaging and Manufacturing Technology*, 9(2):343–352, 2019.

[73] Xinlin Li, Heonkuk Park, Myeong Hoon Lee, Byungil Hwang, Se Hyun Kim, and Sooman Lim. High resolution patterning of ag nanowire flexible transparent electrode via electrohydrodynamic jet printing of acrylic polymer-silicate nanoparticle composite overcoating layer. *Organic Electronics*, 62:400–406, 2018.

[74] Amirreza Panahi, Ahmad Reza Pishevar, and Mohammad Reza Tavakoli. Experimental investigation of electrohydrodynamic modes in electrospraying of viscoelastic polymeric solutions. *Physics of Fluids*, 32(1):012116, 2020.

[75] Matthew S Alexander, Mark D Paine, and John PW Stark. Pulsation modes and the effect of applied voltage on current and flow rate in nanoelectrospray. *Analytical chemistry*, 78(8):2658–2664, 2006.

[76] Saeideh Kholghi Eshkalak, Amutha Chinnappan, WADM Jayathilaka, Marziyeh Khatibzadeh, Elaheh Kowsari, and Seeram Ramakrishna. A review on inkjet printing of cnt composites for smart applications. *Applied Materials Today*, 9: 372–386, 2017.

[77] Ruo-Zhou Li, Anming Hu, Tong Zhang, and Ken D Oakes. Direct writing on paper of foldable capacitive touch pads with silver nanowire inks. *ACS applied materials & interfaces*, 6(23):21721–21729, 2014.

[78] Hantang Qin, Chuang Wei, Jingyan Dong, and Yuan-Shin Lee. Direct printing and electrical characterization of conductive micro-silver tracks by alternating current-pulse modulated electrohydrodynamic jet printing. *Journal of Manufacturing Science and Engineering*, 139(2), 2017.

[79] Hantang Qin, Jingyan Dong, and Yuan-Shin Lee. Ac-pulse modulated electrohydrodynamic jet printing and electroless copper deposition for conductive microscale patterning on flexible insulating substrates. *Robotics and Computer-Integrated Manufacturing*, 43:179–187, 2017.

[80] Huayang Li, Yongqing Duan, Jiangjiang Jin, Jing Huang, Wenzhi Zhang, Tianfu Guo, Hsiang Lun Hsu, and YongAn Huang. 32.2: Multifunctional electrohydrodynamic printing and its industrial applications in flat panel display manufacturing. In *SID Symposium Digest of Technical Papers*, volume 49, pages 351–354. Wiley Online Library, 2018.

[81] Thanh Huy Phung, Seora Kim, and Kye-Si Kwon. A high speed electrohydrodynamic (ehd) jet printing method for line printing. *Journal of Micromechanics and Microengineering*, 27(9):095003, 2017.

[82] Jiaxin Jiang, Gaofeng Zheng, Xiang Wang, Jianyi Zheng, Juan Liu, Yifang Liu, Wenwang Li, and Shumin Guo. Printing of highly conductive solution by alternating current electrohydrodynamic direct-write. In *Journal of Physics: Conference Series*, volume 986, page 012027. IOP Publishing, 2018.

[83] Samuel Haedong Kim, Heuiseok Kang, Kyungtae Kang, Sang Ho Lee, Kwan Hyun Cho, and Jun Young Hwang. Effect of meniscus damping ratio on drop-on-demand electrohydrodynamic jetting. *Applied Sciences*, 8(2):164, 2018.

[84] Joonghyuk Kim, Hyuncheol Oh, and Sang Soo Kim. Electrohydrodynamic drop-on-demand patterning in pulsed cone-jet mode at various frequencies. *Journal of Aerosol Science*, 39(9):819–825, 2008.

[85] Hao Wu, Jun Yu, Rui Cao, Yinghua Yang, and Zhenan Tang. Electrohydrodynamic inkjet printing of pd loaded sno2 nanofibers on a cmos micro hotplate for low power h2 detection. *AIP Advances*, 8(5):055307, 2018.

[86] Xiang Wang, Lei Xu, GaoFeng Zheng, Wei Cheng, and DaoHeng Sun. Pulsed electrohydrodynamic printing of conductive silver patterns on demand. *Science china technological sciences*, 55(6):1603–1607, 2012.

[87] Qi Lei, Jiankang He, Bing Zhang, Jinke Chang, and Dichen Li. Microscale electrohydrodynamic printing of conductive silver features based on in situ reactive inks. *Journal of Materials Chemistry C*, 6(2):213–218, 2018.

[88] Lei Xu, Xiang Wang, Tingping Lei, Daoheng Sun, and Liwei Lin. Electrohydrodynamic deposition of polymeric droplets under low-frequency pulsation. *Langmuir*, 27(10):6541–6548, 2011.

[89] MW Lee, DK Kang, NY Kim, Ho Young Kim, SC James, and SS Yoon. A study of ejection modes for pulsed-dc electrohydrodynamic inkjet printing. *Journal of Aerosol Science*, 46:1–6, 2012.

[90] Weng Hong Lim, Yuen Kiat Yap, Wu Yi Chong, and Harith Ahmad. All-optical graphene oxide humidity sensors. *Sensors*, 14(12):24329–24337, 2014.

[91] Mahdiar Ghadiry, Mehrdad Gholami, Lai Choon Kong, Chong Wu Yi, Harith Ahmad, and Yatima Alias. Nano-anatase tio2 for high performance optical humidity sensing on chip. *Sensors*, 16(1):39, 2016.

[92] Miyeon Jang, Chungsik Yoon, Jihoon Park, and Ohhun Kwon. Evaluation of hazardous chemicals with material safety data sheet and by-products of a photoresist used in the semiconductor-manufacturing industry. *Safety and health at work*, 10 (1):114–121, 2019. ISSN 2093-7911.

[93] Angela Yu-Chen Lin, Sri Chandana Panchangam, and Chao-Chun Lo. The impact of semiconductor, electronics and optoelectronic industries on downstream perfluorinated chemical contamination in taiwanese rivers. *Environmental Pollution*, 157(4):1365–1372, 2009. ISSN 0269-7491.

[94] Yaoming Wang, Zenghui Zhang, Chenxiao Jiang, and Tongwen Xu. Electrodialysis process for the recycling and concentrating of tetramethylammonium hydroxide (tmah) from photoresist developer wastewater. *Industrial & Engineering Chemistry Research*, 52(51):18356–18361, 2013. ISSN 0888-5885.

[95] Sílvia Manuela Ferreira Cruz, Luís A Rocha, and Júlio C Viana. Printing technologies on flexible substrates for printed electronics. In *Flexible electronics*. IntechOpen, 2018.

[96] Rd K Khirotdin, Nurhafizzah Hassan, Hi H Siang, and Muhamad H Zawahid. Printing and curing of conductive ink track on curvature substrate using fluid dispensing system and oven. *Engineering Letters*, 25(3), 2017. ISSN 1816-093X.

[97] Erika Hrehorova, Marian Rebros, Alexandra Pekarovicova, Bradley Bazuin, Amrith Ranganathan, Sean Garner, Gary Merz, John Tosch, and Robert Boudreau. Gravure printing of conductive inks on glass substrates for applications in printed electronics. *Journal of Display Technology*, 7(6):318–324, 2011.

[98] Claudio S Ravasio, Stephen D Hoath, Graham D Martin, Peter Boltryk, and Marko Dorrestijn. Meniscus motion inside a dod inkjet print-head nozzle. In *NIP & Digital Fabrication Conference*, volume 2016, pages 348–352. Society for Imaging Science and Technology, 2016.

[99] Shlomo Magdassi. *The chemistry of inkjet inks*. World scientific, 2009. ISBN 9814470929.

[100] Tatsumi Ishihara and Shogo Matsubara. Capacitive type gas sensors. *Journal of electroceramics*, 2(4):215–228, 1998. ISSN 1385-3449.

[101] Hanns-Erik Endres, Ralf Hartinger, Markus Schwaiger, Gerhard Gmelch, and Mathias Roth. A capacitive co2 sensor system with suppression of the humidity interference. *Sensors and Actuators B: Chemical*, 57(1-3):83–87, 1999. ISSN 0925-4005.

[102] SC Lee and Maureen Chang. Indoor air quality investigations at five classrooms. *Indoor air*, 9(2):134–138, 1999. ISSN 0905-6947.

[103] B Ivanov, O Zhelondz, L Borodulkin, and H Ruser. Distributed smart sensor system for indoor climate monitoring. In *KONNEX Scientific Conf., Mnchen*, pages 10–11, 2002.

[104] Florian Bender, Kerstin Länge, Achim Voigt, and Michael Rapp. Improvement of surface acoustic wave gas and biosensor response characteristics using a capacitive coupling technique. *Analytical chemistry*, 76(13):3837–3840, 2004.

[105] Jung-Yoon Kim, Chao-Hsien Chu, and Sang-Moon Shin. Issaq: An integrated sensing systems for real-time indoor air quality monitoring. *IEEE Sensors Journal*, 14(12):4230–4244, 2014. ISSN 1530-437X.

[106] Yi Liu, Tianhong Cui, and Kody Varahramyan. All-polymer capacitor fabricated with inkjet printing technique. *Solid-State Electronics*, 47(9):1543–1548, 2003. ISSN 0038-1101.

[107] Angélique Tetelin, Claude Pellet, Céline Laville, and Gilles N'Kaoua. Fast response humidity sensors for a medical microsystem. *Sensors and Actuators B: Chemical*, 91(1-3):211–218, 2003. ISSN 0925-4005.

[108] OK Varghese, PD Kichambre, D Gong, KG Ong, EC Dickey, and CA Grimes. Gas sensing characteristics of multi-wall carbon nanotubes. *Sensors and Actuators B: Chemical*, 81(1):32–41, 2001. ISSN 0925-4005.

[109] Peter Van Gerwen, Wim Laureyn, Wim Laureys, Guido Huyberechts, Maaike Op De Beeck, Kris Baert, Jan Suls, Willy Sansen, P Jacobs, and Lou Hermans. Nanoscaled interdigitated electrode arrays for biochemical sensors. *Sensors and Actuators B: Chemical*, 49(1-2):73–80, 1998. ISSN 0925-4005.

[110] M Kitsara, D Goustouridis, S Chatzandroulis, M Chatzichristidi, I Raptis, Th Ganetsos, R Igreja, and CJ Dias. Single chip interdigitated electrode capacitive chemical sensor arrays. *Sensors and Actuators B: Chemical*, 127(1):186–192, 2007. ISSN 0925-4005.

[111] H-E Endres and S Drost. Optimization of the geometry of gas-sensitive interdigital capacitors. *Sensors and Actuators B: Chemical*, 4(1-2):95–98, 1991. ISSN 0925-4005.

[112] Xiaohui Hu and Wuqiang Yang. Planar capacitive sensors–designs and applications. *Sensor Review*, 30(1):24–39, 2010. ISSN 0260-2288.

[113] A Oprea, J Courbat, N Bârsan, D Briand, NF De Rooij, and U Weimar. Temperature, humidity and gas sensors integrated on plastic foil for low power applications. *Sensors and Actuators B: Chemical*, 140(1):227–232, 2009. ISSN 0925-4005.

[114] J Courbat, YB Kim, D Briand, and NF De Rooij. Inkjet printing on paper for the realization of humidity and temperature sensors. In *2011 16th International Solid-State Sensors, Actuators and Microsystems Conference*, pages 1356–1359. IEEE, 2011. ISBN 1457701561.

[115] A Vásquez Quintero, F Molina-Lopez, G Mattana, D Briand, and NF De Rooij. Self-standing printed humidity sensor with thermo-calibration and integrated heater. In *2013 Transducers & Eurosensors XXVII: The 17th International Conference on Solid-State Sensors, Actuators and Microsystems (TRANSDUCERS & EUROSENSORS XXVII)*, pages 838–841. IEEE, 2013. ISBN 1467359831.

[116] Almudena Rivadeneyra, José Fernández-Salmeron, Manuel Agudo, Juan A López-Villanueva, Luis Fermín Capitan-Vallvey, and Alberto J Palma. Design and characterization of a low thermal drift capacitive humidity sensor by inkjet-printing. *Sensors and Actuators B: Chemical*, 195:123–131, 2014. ISSN 0925-4005.

[117] F Molina-Lopez, D Briand, and NF De Rooij. All additive inkjet printed humidity sensors on plastic substrate. *Sensors and Actuators B: Chemical*, 166:212–222, 2012. ISSN 0925-4005.

[118] Catrin Sohrabi, Ginimol Mathew, Thomas Franchi, Ahmed Kerwan, Michelle Griffin, Jennick Soleil C Del Mundo, Syed Ahsan Ali, Maliha Agha, and Riaz Agha. Impact of the coronavirus (covid-19) pandemic on scientific research and implications for clinical academic training–a review. *International Journal of Surgery*, 2021. ISSN 1743-9191.

[119] G Jeffrey Snyder, James R Lim, Chen-Kuo Huang, and Jean-Pierre Fleurial. Thermoelectric microdevice fabricated by a mems-like electrochemical process. *Nature materials*, 2(8):528–531, 2003. ISSN 1476-4660.

[120] L Li, Filipe Vilela, J Forgie, Peter J Skabara, and D Uttamchandani. Miniature humidity micro-sensor based on organic conductive polymer–poly (3, 4-ethylenedioxythiophene). *Micro & Nano Letters*, 4(2):84–87, 2009. ISSN 1750-0443.

[121] L Juhász and J Mizsei. Humidity sensor structures with thin film porous alumina for on-chip integration. *Thin Solid Films*, 517(22):6198–6201, 2009. ISSN 0040-6090.

[122] Kazuhiro Murata. Super-fine ink-jet printing for nanotechnology. In *Proceedings International Conference on MEMS, NANO and Smart Systems*, pages 346–349. IEEE, 2003. ISBN 0769519474.

[123] Ana Moya, Gemma Gabriel, Rosa Villa, and F Javier del Campo. Inkjet-printed electrochemical sensors. *Current Opinion in Electrochemistry*, 2017. ISSN 2451-9103.

[124] Henrik Andersson, Anatoliy Manuilskiy, Tomas Unander, Cecilia Lidenmark, Sven Forsberg, and Hans-Erik Nilsson. Inkjet printed silver nanoparticle humidity sensor with memory effect on paper. *IEEE Sensors Journal*, 12(6):1901–1905, 2011. ISSN 1530-437X.

[125] Mallika Bariya, Ziba Shahpar, Hyejin Park, Junfeng Sun, Younsu Jung, Wei Gao, Hnin Yin Yin Nyein, Tiffany Sun Liaw, Li-Chia Tai, Quynh P Ngo, et al. Roll-to-roll gravure printed electrochemical sensors for wearable and medical devices. *ACS nano*, 12(7):6978–6987, 2018.

[126] Hakyung Jeong, Youngwook Noh, and Dongjin Lee. Highly stable and sensitive resistive flexible humidity sensors by means of roll-to-roll printed electrodes and flower-like tio2 nanostructures. *Ceramics International*, 45(1):985–992, 2019. ISSN 0272-8842.

[127] ASG Reddy, BB Narakathu, MZ Atashbar, M Rebros, E Rebrosova, and MK Joyce. Gravure printed electrochemical biosensor. *Procedia Engineering*, 25: 956–959, 2011. ISSN 1877-7058.

[128] Shaukat Khan, Mazhar Ul-Islam, Muhammad Wajid Ullah, Yeji Kim, and Joong Kon Park. Synthesis and characterization of a novel bacterial cellulose–poly (3, 4-ethylenedioxythiophene)–poly (styrene sulfonate) composite for use in biomedical applications. *Cellulose*, 22(4):2141–2148, 2015.

[129] Seunghyeon Lee, Yeongbeom Hong, and Bong Sup Shim. biodegradable pedot: Pss/clay composites for multifunctional green-electronic materials. *Advanced Sustainable Systems*, page 2100056, 2021.

[130] R Pradeep Kumar and Annie Abraham. Pvp-coated naringenin nanoparticles for biomedical applications–in vivo toxicological evaluations. *Chemico-biological interactions*, 257:110–118, 2016.

[131] Adnan Haider and Inn-Kyu Kang. Preparation of silver nanoparticles and their industrial and biomedical applications: a comprehensive review. *Advances in materials science and engineering*, 2015, 2015.

[132] David Roe, Balu Karandikar, Nathan Bonn-Savage, Bruce Gibbins, and Jean-Baptiste Roullet. Antimicrobial surface functionalization of plastic catheters by silver nanoparticles. *Journal of antimicrobial chemotherapy*, 61(4):869–876, 2008.

[133] Amit Gupta, Kazuaki Matsui, Jeng-Fan Lo, and Simon Silver. Molecular basis for resistance to silver cations in salmonella. *Nature medicine*, 5(2):183–188, 1999.

[134] Jose Ruben Morones, Jose Luis Elechiguerra, Alejandra Camacho, Katherine Holt, Juan B Kouri, Jose Tapia Ramírez, and Miguel Jose Yacaman. The bactericidal effect of silver nanoparticles. *Nanotechnology*, 16(10):2346, 2005.

[135] MK Inglesby and SH Zeronian. Direct dyes as molecular sensors to characterize cellulose substrates. *Cellulose*, 9(1):19–29, 2002.

[136] Jin-Woo Han, Beomseok Kim, Jing Li, and M Meyyappan. Carbon nanotube based humidity sensor on cellulose paper. *The Journal of Physical Chemistry C*, 116(41):22094–22097, 2012.

[137] Zhouping Yin, Yongan Huang, Yongqing Duan, and Haitao Zhang. *Electrohydrodynamic direct-writing for flexible electronic manufacturing*. Springer, 2018.

[138] GP Alcantara and CGM Andrade. A short review of gas sensors based on interdigital electrode. In *2015 12th IEEE International Conference on Electronic*

Measurement & Instruments (ICEMI), volume 3, pages 1616–1621. IEEE, 2015. ISBN 1479970719.

[139] Ryan D Boehm, Shaun D Gittard, Jacqueline MH Byrne, Anand Doraiswamy, Jonathan J Wilker, Timothy M Dunaway, Rene Crombez, Weidian Shen, Yuan-Shin Lee, and Roger J Narayan. Piezoelectric inkjet printing of medical adhesives and sealants. *Jom*, 62(7):56–60, 2010. ISSN 1543-1851.

[140] Ryan D Boehm, Philip R Miller, Justin Daniels, Shane Stafslien, and Roger J Narayan. Inkjet printing for pharmaceutical applications. *Materials Today*, 17(5): 247–252, 2014. ISSN 1369-7021.

[141] Anand Doraiswamy, Timothy M Dunaway, Jonathan J Wilker, and Roger J Narayan. Inkjet printing of bioadhesives. *Journal of Biomedical Materials Research Part B: Applied Biomaterials: An Official Journal of The Society for Biomaterials, The Japanese Society for Biomaterials, and The Australian Society for Biomaterials and the Korean Society for Biomaterials*, 89(1):28–35, 2009. ISSN 1552-4973.

[142] Jae Dong Kim, Ji Suk Choi, Beob Soo Kim, Young Chan Choi, and Yong Woo Cho. Piezoelectric inkjet printing of polymers: Stem cell patterning on polymer substrates. *Polymer*, 51(10):2147–2154, 2010. ISSN 0032-3861.

[143] Yuanhua Li, Omar Dahhan, Carlos DM Filipe, John D Brennan, and Robert H Pelton. Optimizing piezoelectric inkjet printing of silica sols for biosensor production. *Journal of Sol-Gel Science and Technology*, 87(3):657–664, 2018. ISSN 1573-4846.

[144] Makoto Nakamura, Akiko Kobayashi, Fumio Takagi, Akihiko Watanabe, Yuko Hiruma, Katsuhiro Ohuchi, Yasuhiko Iwasaki, Mikio Horie, Ikuo Morita, and Setsuo Takatani. Biocompatible inkjet printing technique for designed seeding of individual living cells. *Tissue engineering*, 11(11-12):1658–1666, 2005. ISSN 1076-3279.

[145] Tao Xu, Joyce Jin, Cassie Gregory, James J Hickman, and Thomas Boland. Inkjet printing of viable mammalian cells. *Biomaterials*, 26(1):93–99, 2005. ISSN 0142-9612.

[146] Marc Aliqué, Claudia Delgado Simão, Gonzalo Murillo, and Ana Moya. Fully-printed piezoelectric devices for flexible electronics applications. *Advanced Materials Technologies*, 6(3):2001020, 2021. ISSN 2365-709X.

[147] Junfeng Mei, Michael R Lovell, and Marlin H Mickle. Formulation and processing of novel conductive solution inks in continuous inkjet printing of 3-d electric circuits. *IEEE transactions on electronics packaging manufacturing*, 28(3):265–273, 2005. ISSN 1521-334X.

[148] Ashok Sridhar, Thomas Blaudeck, and Reinhard R Baumann. Inkjet printing as a key enabling technology for printed electronics. *Material Matters*, 6(1):12–15, 2011.

[149] ZhouPing Yin, YongAn Huang, NingBin Bu, XiaoMei Wang, and YouLun Xiong. Inkjet printing for flexible electronics: Materials, processes and equipments. *Chinese Science Bulletin*, 55(30):3383–3407, 2010. ISSN 1861-9541.

[150] Helmut Kipphan. *Handbook of print media: technologies and production methods*. Springer Science Business Media, 2001. ISBN 3540673261.

[151] Lucas P Bressan, Jessica Robles-Najar, Cristina B Adamo, Reverson F Quero, Brenda MC Costa, Dosil P de Jesus, and Jose AF da Silva. 3d-printed microfluidic device for the synthesis of silver and gold nanoparticles. *Microchemical Journal*, 146:1083–1089, 2019. ISSN 0026-265X.

[152] Seung Hwan Ko, Jaewon Chung, Heng Pan, Costas P Grigoropoulos, and Dimos Poulikakos. Fabrication of multilayer passive and active electric components on polymer using inkjet printing and low temperature laser processing. *Sensors and Actuators A: Physical*, 134(1):161–168, 2007. ISSN 0924-4247.

[153] Ana Moya, Enrico Sowade, Francisco J del Campo, Kalyan Y Mitra, Eloi Ramon, Rosa Villa, Reinhard R Baumann, and Gemma Gabriel. All-inkjet-printed dissolved oxygen sensors on flexible plastic substrates. *Organic Electronics*, 39: 168–176, 2016. ISSN 1566-1199.

[154] Mathilde Rieu, Malick Camara, Guy Tournier, Jean-Paul Viricelle, Christophe Pijolat, Nico F de Rooij, and Danick Briand. Fully inkjet printed sno2 gas sensor on plastic substrate. *Sensors and Actuators B: Chemical*, 236:1091–1097, 2016. ISSN 0925-4005.

[155] Susanita Carvajal, Samantha N Fera, Abby L Jones, Thaisa A Baldo, Islam M Mosa, James F Rusling, and Colleen E Krause. Disposable inkjet-printed electrochemical platform for detection of clinically relevant her-2 breast cancer biomarker. *Biosensors and Bioelectronics*, 2018. ISSN 0956-5663.

[156] TM Eggenhuisen, Y Galagan, AFKV Biezemans, TMWL Slaats, WP Voorthuijzen, S Kommeren, S Shanmugam, JP Teunissen, A Hadipour, and WJH Verhees. High efficiency, fully inkjet printed organic solar cells with freedom of design. *Journal of Materials Chemistry A*, 3(14):7255–7262, 2015.

[157] Peter Mack Grubb, Harish Subbaraman, Saungeun Park, Deji Akinwande, and Ray T Chen. Inkjet printing of high performance transistors with micron order chemically set gaps. *Scientific reports*, 7(1):1202, 2017. ISSN 2045-2322.

[158] Jin-A Jeong, Jihoon Kim, and Han-Ki Kim. Ag grid/ito hybrid transparent electrodes prepared by inkjet printing. *Solar Energy Materials and Solar Cells*, 95(7): 1974–1978, 2011. ISSN 0927-0248.

[159] Enrico Sowade, Eloi Ramon, Kalyan Yoti Mitra, Carme Martínez-Domingo, Marta Pedró, Jofre Pallarès, Fausta Loffredo, Fulvia Villani, Henrique L Gomes, and Lluís Terés. All-inkjet-printed thin-film transistors: manufacturing process reliability by root cause analysis. *Scientific reports*, 6:33490, 2016. ISSN 2045-2322.

[160] Seonhee Jang, Youngkwan Seo, Joonrak Choi, Taehoon Kim, Jeongmin Cho, Sungeun Kim, and Donghoon Kim. Sintering of inkjet printed copper nanoparticles for flexible electronics. *Scripta Materialia*, 62(5):258–261, 2010.

[161] Shujie Liu, Yujie Li, Songling Xing, Lei Liu, Guisheng Zou, and Peng Zhang. Structure inheritance in nanoparticle ink direct-writing processes and crack-free nano-copper interconnects printed by a single-run approach. *Materials*, 12(9):1559, 2019.

[162] Shohei Norita, Daisuke Kumaki, Yu Kobayashi, Tsubasa Sato, Kenjiro Fukuda, and Shizuo Tokito. Inkjet-printed copper electrodes using photonic sintering and their application to organic thin-film transistors. *Organic Electronics*, 25:131–134, 2015.

[163] Bong Kyun Park, Dongjo Kim, Sunho Jeong, Jooho Moon, and Jang Sub Kim. Direct writing of copper conductive patterns by ink-jet printing. *Thin solid films*, 515(19):7706–7711, 2007.

[164] Muhammad Asif Ali Rehmani and Khalid Mahmood Arif. High resolution electrohydrodynamic printing of conductive ink with an aligned aperture coaxial printhead. *The International Journal of Advanced Manufacturing Technology*, pages 1–16, 2021. ISSN 1433-3015.

[165] Robert Ward, James Anderson, Rick McVenes, and Ken Stokes. In vivo biostability of polyether polyurethanes with fluoropolymer and polyethylene oxide surface modifying endgroups; resistance to metal ion oxidation. *Journal of Biomedical Materials Research Part A: An Official Journal of The Society for Biomaterials, The Japanese Society for Biomaterials, and The Australian Society for Biomaterials and the Korean Society for Biomaterials*, 80(1):34–44, 2007.

[166] Bob Ward, James Anderson, Rick McVenes, and Ken Stokes. In vivo biostability of polyether polyurethanes with fluoropolymer surface modifying endgroups: resistance to biologic oxidation and stress cracking. *Journal of Biomedical Materials Research Part A*, 79(4):827–835, 2006.

[167] Haiyan Wang, Yanzhi Wang, Dongxu Liu, Zonghui Sun, and Huicong Wang. Effects of additives on weather-resistance properties of polyurethane films exposed to ultraviolet radiation and ozone atmosphere. *Journal of Nanomaterials*, 2014, 2014.

[168] BG Girija, RRN Sailaja, and Giridhar Madras. Thermal degradation and mechanical properties of pet blends. *Polymer Degradation and stability*, 90(1):147–153, 2005.

[169] N Torres, JJ Robin, and B Boutevin. Study of thermal and mechanical properties of virgin and recycled poly (ethylene terephthalate) before and after injection molding. *European Polymer Journal*, 36(10):2075–2080, 2000.

[170] S Magdassi. The chemistry of silver ink. *World Scientific Publishing. Singapore:[sn]*, 2010.

[171] A Kosmala, R Wright, Qi Zhang, and P Kirby. Synthesis of silver nano particles and fabrication of aqueous ag inks for inkjet printing. *Materials Chemistry and Physics*, 129(3):1075–1080, 2011.

[172] Sonia Sharma, Sumukh S Pande, and P Swaminathan. Top-down synthesis of zinc oxide based inks for inkjet printing. *RSC advances*, 7(63):39411–39419, 2017.

[173] DK Kang, MW Lee, Ho Young Kim, SC James, and SS Yoon. Electrohydrodynamic pulsed-inkjet characteristics of various inks containing aluminum particles. *Journal of Aerosol Science*, 42(10):621–630, 2011.

[174] Mei Fang, Tianli Li, Sangjian Zhang, K Venkat Rao, and Lyubov Belova. Design and tailoring of inks for inkjet patterning of metal oxides. *Royal Society open science*, 7(4):200242, 2020.

[175] Rajendra K Bordia and Anand Jagota. Crack growth and damage in constrained sintering films. *Journal of the American Ceramic Society*, 76(10):2475–2485, 1993.

[176] Hugo Mercier, Franck Levassort, Hana Uršič, and Danjela Kuscer. Microstructure evolution and electromechanical properties of (k, na) nbo3-based thick films. *Journal of the American Ceramic Society*, 103(12):6677–6689, 2020.

[177] GEORGE W SCHERER and Terry Garino. Viscous sintering on a rigid substrate. *Journal of the American Ceramic Society*, 68(4):216–220, 1985.

[178] Dong Jun Lee, Je Hoon Oh, and Han Seung Bae. Crack formation and substrate effects on electrical resistivity of inkjet-printed ag lines. *Materials Letters*, 64(9): 1069–1072, 2010.

[179] Mahesh S Tirumkudulu and William B Russel. Cracking in drying latex films. *Langmuir*, 21(11):4938–4948, 2005.

[180]

[181] ACM Yang and HR Brown. Solvent induced crack-like defects in adhered polyimide films. *MRS Online Proceedings Library (OPL)*, 72, 1986.

[182] Neil Dalal, Yuan Gu, Daniel R Hines, Abhijit Dasgupta, and Siddhartha Das. Cracks in the 3d-printed conductive traces of silver nanoparticle ink. *Journal of Micromechanics and Microengineering*, 29(9):097001, 2019.

[183] Philip J Kitson, Mali H Rosnes, Victor Sans, Vincenza Dragone, and Leroy Cronin. Configurable 3d-printed millifluidic and microfluidic 'lab on a chip'reactionware devices. *Lab on a Chip*, 12(18):3267–3271, 2012.

[184] Mark D Symes, Philip J Kitson, Jun Yan, Craig J Richmond, Geoffrey JT Cooper, Richard W Bowman, Turlif Vilbrandt, and Leroy Cronin. Integrated 3d-printed reactionware for chemical synthesis and analysis. *Nature chemistry*, 4(5):349–354, 2012.

[185] Matthew K Gelber and Rohit Bhargava. Monolithic multilayer microfluidics via sacrificial molding of 3d-printed isomalt. *Lab on a Chip*, 15(7):1736–1741, 2015.

[186] Paul J Hung, Philip J Lee, Poorya Sabounchi, Robert Lin, and Luke P Lee. Continuous perfusion microfluidic cell culture array for high-throughput cell-based assays. *Biotechnology and bioengineering*, 89(1):1–8, 2005.

[187] Sidra Waheed, Joan M Cabot, Niall P Macdonald, Trevor Lewis, Rosanne M Guijt, Brett Paull, and Michael C Breadmore. 3d printed microfluidic devices: enablers and barriers. *Lab on a Chip*, 16(11):1993–2013, 2016.

[188] FAN Yi-Qiang, WANG Hong-Liang, GAO Ke-Xin, LIU Jing-Ji, CHAI Dong-Ping, and Ya-Jun ZHANG. Applications of modular microfluidics technology. *Chinese Journal of Analytical Chemistry*, 46(12):1863–1871, 2018.

[189] Stefania Torino, Brunella Corrado, Mario Iodice, and Giuseppe Coppola. Pdms-based microfluidic devices for cell culture. *Inventions*, 3(3):65, 2018.

[190] E Brandon Strong, Carsten Knutsen, Jay T Wells, Aditya R Jangid, Megan L Mitchell, Nathaniel W Martinez, and Andres W Martinez. Wax-printed fluidic time delays for automating multi-step assays in paper-based microfluidic devices (micropads). *Inventions*, 4(1):20, 2019.

[191] Lung-Ming Fu, Chin-Chung Tseng, Wei-Jhong Ju, and Ruey-Jen Yang. Rapid paper-based system for human serum creatinine detection. *Inventions*, 3(2):34, 2018.

[192] Babak Ziaie, Antonio Baldi, Ming Lei, Yuandong Gu, and Ronald A Siegel. Hard and soft micromachining for biomems: review of techniques and examples of applications in microfluidics and drug delivery. *Advanced drug delivery reviews*, 56 (2):145–172, 2004. ISSN 0169-409X.

[193] Usama M Attia, Silvia Marson, and Jeffrey R Alcock. Micro-injection moulding of polymer microfluidic devices. *Microfluidics and nanofluidics*, 7(1):1, 2009. ISSN 1613-4982.

[194] Yong He, Qing Gao, Wen-Bin Wu, Jing Nie, and Jian-Zhong Fu. 3d printed paper-based microfluidic analytical devices. *Micromachines*, 7(7):108, 2016.

[195] Gabriel Gaal, Melissa Mendes, Tiago P de Almeida, Maria HO Piazzetta, Ângelo L Gobbi, Antonio Riul Jr, and Varlei Rodrigues. Simplified fabrication of integrated microfluidic devices using fused deposition modeling 3d printing. *Sensors and Actuators B: Chemical*, 242:35–40, 2017.

[196] Anna V Nielsen, Michael J Beauchamp, Gregory P Nordin, and Adam T Woolley. 3d printed microfluidics. *Annual Review of Analytical Chemistry*, 13:3862–3881, 2019.

[197] Jessica L Moore, Austin McCuiston, Isaac Mittendorf, Rudy Ottway, and R Daniel Johnson. Behavior of capillary valves in centrifugal microfluidic devices prepared by three-dimensional printing. *Microfluidics and Nanofluidics*, 10(4):877–888, 2011.

[198] Anthony K Au, Wilson Huynh, Lisa F Horowitz, and Albert Folch. 3d-printed microfluidics. *Angewandte Chemie International Edition*, 55(12):3862–3881, 2016.

[199] Bruce K Gale, Alexander R Jafek, Christopher J Lambert, Brady L Goenner, Hossein Moghimifam, Ugochukwu C Nze, and Suraj Kumar Kamarapu. A review of current methods in microfluidic device fabrication and future commercialization prospects. *Inventions*, 3(3):60, 2018.

[200] Amélie Neuville, Louis Renaud, Thi Thuy Luu, Mona Wetrhus Minde, Espen Jettestuen, Jan Ludvig Vinningland, Aksel Hiorth, and Dag Kristian Dysthe. Xurography for microfluidics on a reactive solid. *Lab on a Chip*, 17(2):293–303, 2017.

[201] Nicholas C Speller, Giorgio Gianini Morbioli, Michael E Cato, Thomas P Cantrell, Erin M Leydon, Britney E Schmidt, and Amanda M Stockton. Cutting edge microfluidics: Xurography and a microwave. *Sensors and Actuators B: Chemical*, 291:250–256, 2019.

[202] Wenlai Tang, Hao Liu, Liya Zhu, Jianping Shi, Zongan Li, Nan Xiang, and Jiquan Yang. Fabrication of different microchannels by adjusting the extrusion parameters for sacrificial molds. *Micromachines*, 10(8):544, 2019.

[203] Nirveek Bhattacharjee, Arturo Urrios, Shawn Kang, and Albert Folch. The upcoming 3d-printing revolution in microfluidics. *Lab on a Chip*, 16(10):1720–1742, 2016.

[204] Ryan D Sochol, Eric Sweet, Casey C Glick, Sung-Yueh Wu, Chen Yang, Michael Restaino, and Liwei Lin. 3d printed microfluidics and microelectronics. *Microelectronic Engineering*, 189:52–68, 2018.

[205] Feng Li, Petr Smejkal, Niall P Macdonald, Rosanne M Guijt, and Michael C Breadmore. One-step fabrication of a microfluidic device with an integrated membrane and embedded reagents by multimaterial 3d printing. *Analytical chemistry*, 89(8): 4701–4707, 2017.

[206] Feng Li, Niall P Macdonald, Rosanne M Guijt, and Michael C Breadmore. Using printing orientation for tuning fluidic behavior in microfluidic chips made by fused deposition modeling 3d printing. *Analytical chemistry*, 89(23):12805–12811, 2017.

[207] Gert IJ Salentijn, Pieter E Oomen, Maciej Grajewski, and Elisabeth Verpoorte. Fused deposition modeling 3d printing for (bio) analytical device fabrication: procedures, materials, and applications. *Analytical chemistry*, 89(13):7053–7061, 2017.

[208] Frederik Kotz, Markus Mader, Nils Dellen, Patrick Risch, Andrea Kick, Dorothea Helmer, and Bastian E. Rapp. Fused deposition modeling of microfluidic chips in polymethylmethacrylate. *Micromachines*, 11(9), 2020. ISSN 2072-666X. doi: 10.3390/mi11090873. URL https://www.mdpi.com/2072-666X/11/9/873.

[209] Joan M Cabot, Elisabet Fuguet, Marti Roses, Petr Smejkal, and Michael C Breadmore. Novel instrument for automated p k a determination by internal standard capillary electrophoresis. *Analytical chemistry*, 87(12):6165–6172, 2015.

[210] Aliaa I Shallan, Petr Smejkal, Monika Corban, Rosanne M Guijt, and Michael C Breadmore. Cost-effective three-dimensional printing of visibly transparent microchips within minutes. *Analytical chemistry*, 86(6):3124–3130, 2014.

[211] Xiaojun Chen, Hong Chen, Dezhi Wu, Qinnan Chen, Zhou Zhou, Rongrong Zhang, Xingyue Peng, Yu-Chuan Su, and Daoheng Sun. 3d printed microfluidic chip for multiple anticancer drug combinations. *Sensors and Actuators B: Chemical*, 276: 507–516, 2018.

[212] Sarah K Anciaux, Matthew Geiger, and Michael T Bowser. 3d printed micro free-flow electrophoresis device. *Analytical chemistry*, 88(15):7675–7682, 2016.

[213] Mojtaba Zeraatkar, Daniel Filippini, and Gianluca Percoco. On the impact of the fabrication method on the performance of 3d printed mixers. *Micromachines*, 10 (5):298, 2019.

[214] Niall P Macdonald, Joan M Cabot, Petr Smejkal, Rosanne M Guijt, Brett Paull, and Michael C Breadmore. Comparing microfluidic performance of three-dimensional (3d) printing platforms. *Analytical chemistry*, 89(7):3858–3866, 2017.

[215] Jia Min Lee, Meng Zhang, and Wai Yee Yeong. Characterization and evaluation of 3d printed microfluidic chip for cell processing. *Microfluidics and Nanofluidics*, 20(1):5, 2016.

[216] Mohamed GA Mohamed, Hitendra Kumar, Zongjie Wang, Nicholas Martin, Barry Mills, and Keekyoung Kim. Rapid and inexpensive fabrication of multi-depth microfluidic device using high-resolution lcd stereolithographic 3d printing. *Journal of Manufacturing and Materials Processing*, 3(1):26, 2019.

[217] Jia Ming Zhang, Qinglei Ji, and Huiling Duan. Three-dimensional printed devices in droplet microfluidics. *Micromachines*, 10(11):754, 2019.

[218] Feng Zhu, Timo Friedrich, Dayanthi Nugegoda, Jan Kaslin, and Donald Wlodkowic. Assessment of the biocompatibility of three-dimensional-printed polymers using multispecies toxicity tests. *Biomicrofluidics*, 9(6):061103, 2015. ISSN 1932-1058.

[219] Xin Wang, Man Jiang, Zuowan Zhou, Jihua Gou, and David Hui. 3d printing of polymer matrix composites: A review and prospective. *Composites Part B: Engineering*, 110:442–458, 2017. ISSN 1359-8368.

[220] J Israel Martínez-López, Héctor Andrés Betancourt Cervantes, Luis Donaldo Cuevas Iturbe, Elisa Vázquez, Edisson A Naula, Alejandro Martínez López, Héctor R Siller, Christian Mendoza-Buenrostro, and Ciro A Rodríguez. Characterization of soft tooling photopolymers and processes for micromixing devices with variable cross-section. *Micromachines*, 11(11):970, 2020.

[221] Kiran Raj M and Suman Chakraborty. Pdms microfluidics: A mini review. *Journal of Applied Polymer Science*, 137(27):48958, 2020. ISSN 0021-8995.

[222] Daniela Pranzo, Piero Larizza, Daniel Filippini, and Gianluca Percoco. Extrusion-based 3d printing of microfluidic devices for chemical and biomedical applications: A topical review. *Micromachines*, 9(8):374, 2018.

[223] Chengpeng Chen, Benjamin T Mehl, Akash S Munshi, Alexandra D Townsend, Dana M Spence, and R Scott Martin. 3d-printed microfluidic devices: fabrication, advantages and limitations—a mini review. *Analytical Methods*, 8(31):6005–6012, 2016.

[224] Nan Zhang, Jinghang Liu, Honggang Zhang, Nigel J Kent, Dermot Diamond, and Michael D Gilchrist. 3d printing of metallic microstructured mould using selective laser melting for injection moulding of plastic microfluidic devices. *Micromachines*, 10(9):595, 2019.

[225] John A Rogers and Ralph G Nuzzo. Recent progress in soft lithography. *Materials today*, 8(2):50–56, 2005. ISSN 1369-7021.

[226] Pilnam Kim, Keon Woo Kwon, Min Cheol Park, Sung Hoon Lee, Sun Min Kim, and Kahp Yang Suh. Soft lithography for microfluidics: a review. 2:1–11, 2008. ISSN 1976-0280.

[227] Rajendrani Mukhopadhyay. When pdms isn't the best. *Analytical Chemistry*, 79 (9):3248–3253, 2007.

[228] Yong He, Yan Wu, Jian-Zhong Fu, and Wen-Bin Wu. Fabrication of paper-based microfluidic analysis devices: a review. *Rsc Advances*, 5(95):78109–78127, 2015.

[229] Fabian Rengier, Amit Mehndiratta, Hendrik Von Tengg-Kobligk, Christian M Zechmann, Roland Unterhinninghofen, H-U Kauczor, and Frederik L Giesel. 3d printing based on imaging data: review of medical applications. *International journal of computer assisted radiology and surgery*, 5(4):335–341, 2010. ISSN 1861-6410.

[230] Yanen Wang, Mingju Lei, Qinghua Wei, Yanmei Wang, Juan Zhang, Ying Guo, and Jabran Saroia. 3d printing biocompatible l-arg/gnps/pla nanocomposites with enhanced mechanical property and thermal stability. *Journal of Materials Science*, 55(12):5064–5078, 2020. ISSN 1573-4803.

[231] Agathe Grémare, Vera Guduric, Reine Bareille, Valérie Heroguez, Simon Latour, Nicolas L'heureux, Jean-Christophe Fricain, Sylvain Catros, and Damien Le Nihouannen. Characterization of printed pla scaffolds for bone tissue engineering. *Journal of Biomedical Materials Research Part A*, 106(4):887–894, 2018. ISSN 1549-3296.

[232] Matthias C Wurm, Tobias Möst, Bastian Bergauer, Dominik Rietzel, Friedrich Wilhelm Neukam, Sandra C Cifuentes, and Cornelius von Wilmowsky. In-vitro evaluation of polylactic acid (pla) manufactured by fused deposition modeling. *Journal of biological engineering*, 11(1):1–9, 2017. ISSN 1754-1611.

[233] Eujin Pei, Garrett W Melenka, Jonathon S Schofield, Michael R Dawson, and Jason P Carey. Evaluation of dimensional accuracy and material properties of the makerbot 3d desktop printer. *Rapid Prototyping Journal*, 21:618–627, 2015. ISSN 1355-2546.

[234] Oğuzhan Emre Akbaş, Onur Hıra, Sahar Zhiani Hervan, Shahrad Samankan, and Atakan Altınkaynak. Dimensional accuracy of fdm-printed polymer parts. *Rapid Prototyping Journal*, 26:288–298, 2019. ISSN 1355-2546.

[235] Tiertime. *Price of Tiertime UP 02 Printer*, 2020. Available online: https://shop.tiertime.com/product/tiertime-up-plus-2-3d-printer/ (accessed November 16, 2020).

[236] Prusa. *Price of Prusa i3 MK3S Printer*, 2020. Available online: https://shop.prusa3d.com/en/3d-printers/180-original-prusa-i3-mk3s-kit.html (accessed November 16, 2020).